Energy & Environmental Science

Cite this: *Energy Environ. Sci.*, 2012, **5**, 8475

www.rsc.org/ees

REVIEW

Nanostructured ceria-based materials: synthesis, properties, and applications

Chunwen Sun,*[ab] Hong Li[ab] and Liquan Chen[ab]

Received 22nd May 2012, Accepted 28th June 2012
DOI: 10.1039/c2ee22310d

The controllable synthesis of nanostructured CeO_2-based materials is an imperative issue for environment- and energy-related applications. In this review, we present the recent technological and theoretical advances related to the CeO_2-based nanomaterials, with a focus on the synthesis from one dimensional to mesoporous ceria as well as the properties from defect chemistry to nano-size effects. Seven extensively studied aspects regarding the applications of nanostructured ceria-based materials are selectively surveyed as well. New experimental approaches have been demonstrated with an atomic scale resolution characterization. Density functional theory (DFT) calculations can provide insight into the rational design of highly reactive catalysts and understanding of the interactions between the noble metal and ceria support. Achieving desired morphologies with designed crystal facets and oxygen vacancy clusters in ceria *via* controlled synthesis process is quite important for highly active catalysts. Finally, remarks on the challenges and perspectives on this exciting field are proposed.

1. Introduction

As defined by IUPAC, rare earth elements include a set of seventeen chemical elements in the periodic table, specifically the fifteen lanthanides along with scandium and yttrium. Among the rare earth family, cerium (Ce) is the most abundant element. Cerium is more abundant in the Earth's crust (66.5 ppm) than that of copper (60 ppm) or tin (2.3 ppm).[1–3] The electron configuration of cerium is [Xe] $4f^2 6s^2$ with two common valence state cerium(III) and cerium(IV). With a high abundance, cerium oxide (CeO_2) is a technologically important material due to its wide applications as a promoter in three-way catalysts (TWCs) for the elimination of toxic auto-exhaust gases,[4,5] low-temperature water–gas shift (WGS) reaction,[6,7] oxygen sensors,[8,9] oxygen permeation membrane systems,[10,11] fuel cells,[12–15] glass-polishing materials,[16,17] electrochromic thin-film application,[18–20] ultraviolet absorbent,[21] as well as biotechnology, environmental chemistry, and medicine.[22,23] With a decrease in particle size, there usually are high densities of interfaces in nanocrystalline solids. The energetics for defect formation may be substantially reduced in nanocrystalline oxides leading to markedly increased levels of nonstoichiometry and electronic carrier generation.[24] Therefore, nanostructured CeO_2 has attracted much attention due to improvements in the redox properties, transport properties and surface to volume ratio with respect to the bulk materials. A vast number of papers related to the topic of

[a]*Beijing National Laboratory for Condensed Matter Physics, Institute of Physics, Chinese Academy of Sciences, Beijing 100190, China. E-mail: csun@iphy.ac.cn; Fax: +86-10-82649046; Tel: +86-10-82649901*
[b]*Key Laboratory for Renewable Energy, Chinese Academy of Sciences, Beijing Key Laboratory for New Energy Materials and Devices, Beijing 100190, China*

Broader context

In the context of significant interest and concern on energy and environment, nanostructured cerium oxide (CeO_2)-based materials are highly desired for solving present energy- and environment-related issues due to the improvements in redox properties, transport properties and surface to volume ratio with respect to the bulk materials. Ceria is one of the most studied metal oxides and it has been widely used in clean energy, environmental protection and remediation, typically including as a promoter in three-way catalysts (TWCs) for the elimination of toxic auto-exhaust gases, low-temperature water-gas shift (WGS) reaction, solid oxide fuel cells (SOFCs), solar-driven thermochemical CO_2 reduction, biomass reforming, as well as biotechnology, environmental chemistry, and medicine. Most of these applications are related to the rapid formation and elimination of oxygen vacancy in CeO_2 that endows it with a high oxygen storage capacity. New experimental approaches with an atomic scale resolution and density functional theory (DFT) calculations can provide insight into the rational design of highly reactive catalysts and understanding of the interactions between the noble metal and ceria support. In this paper, we attempt to provide an overview of present research progresses in the field of controllable synthesis of nanostructured ceria with various morphologies, their unique properties, as well as a few typical applications and theory study.

nanostructured ceria and their applications have been published in the past decade. Especially, Bumajdad *et al.*[25] reviewed recent research on the synthesis of cerium oxide in colloidal dispersions media for obtaining high surface area catalyst materials. Yan *et al.*[26] extensively reviewed controlled synthesis and assembly of ceria-based nanomaterials. Yan's group also demonstrated applications of coordination chemistry principle in the synthesis and assembly of rare earth nanocrystals, particularly the coordination effect on the control of structure/microstructure/texture, surface/interface, particle size and morphology.[27] Traversa and Esposito[28] demonstrated ceria microstructures for specific ionic device applications that can be tuned by a combined effect of powder grain size, dopant content, and sintering temperature–time profile. In addition, Vivier and Duprez[29] reviewed the applications of ceria-based solid catalysts in various organic synthesis reactions. Guo and Waser[30] reviewed the electrical properties of the grain boundaries of acceptor-doped zirconia and ceria. However, the former two papers mainly focus on the controlled synthesis and assembly of ceria-based nanomaterials, while the latter two papers are not involved in nanostructured ceria materials. This critical review aims to provide an overview of present research progress in the field of synthesis of nanostructured ceria with various morphologies, their unique properties, as well as a few typical applications and theory study. Regrettably, it is not possible to cover all aspects and references in the literature. It is not our intention to provide an exhaustive review of the entire field.

2. Properties

2.1. Material properties and defect chemistry of ceria

CeO_2 crystallizes in the fluorite crystal structure with space group $Fm\bar{3}m$ over the temperature range from room temperature to the melting point. The fluorite structure consists of a face-centered cubic (f.c.c.) unit cell of cations with anions occupying the octahedral interstitial sites. This can also be seen as a superposition of a f.c.c. lattice of cations (Ce^{4+}) with lattice constant a, and a simple cubic lattice of anions (O^{2-}) with lattice constant $a/2$.[31] In this structure (shown schematically in Fig. 1), each cerium cation is coordinated by eight nearest-neighbor oxygen anions, while each oxygen anion is coordinated by four nearest-neighbor cerium cations.[31] The color of CeO_2 is pale yellow, probably due to Ce(IV)–O(II) charge transfer, while non-stoichiometric $CeO_{2-\delta}$ ($0<\delta<0.5$) is blue and turns almost black.[32] Ceria in the fluorite structure exhibits a few defects depending on partial pressure of oxygen, which is the intrinsic property for its potentials in catalysis, energy conversion, and other applications. Under the reduction extreme, CeO_2 becomes the hexagonal sesquioxide Ce_2O_3 ($P\bar{3}m1$). Some of the physical properties of CeO_2 are listed in Table 1.[32–36]

Like stabilized zirconia, cerium oxide can accommodate a high oxygen deficiency by the substitution of lower valent elements on the cation sublattice. This leads to high oxygen ion conductivities and its interest as a solid electrolyte in solid oxide fuel cells.[12,30] At the same time, CeO_2 is also well known to release significant levels of oxygen at low oxygen partial pressures (P_{O2}) and elevated temperatures (*e.g.* $<\sim 10^{-15}$ atm O_2 at 800 °C) leading to a mixed ionic electronic conductivity (MIEC). This can be described by the following defect reaction, written in Kröger–Vink notation.[37]

$$O_O^{\times} \leftrightarrow V_O^{\cdot\cdot} + 2e' + \frac{1}{2}O_2(g) \quad (1)$$

where $O_O^{\times}$, $V_O^{\cdot\cdot}$, and e' are oxide ions in the lattice, doubly charged oxygen vacancies, and electrons in the conduction band made up of Ce 4f energy states, respectively.[38,39] The electrons formed during reduction are often treated as being localized on cerium, thereby converting Ce^{4+} to Ce^{3+} ions.[38] This is consistent with the demonstration that electrons in ceria can be described as small polarons, *i.e.* the motion of electrons through the lattice is achieved *via* a thermally activated hopping process.[40] Defects such as oxygen vacancies dominate the electronic and chemical properties of ceria. The normal definition of oxygen vacancy concentration is the stoichiometric vacancy concentration, which is determined by the solute concentration through the electroneutrality condition; however, for transport measurements only the mobile vacancy concentration should be taken into account

Chunwen Sun

Chunwen Sun is an associate professor in Institute of Physics, Chinese Academy of Sciences. He received his Ph.D. in Condensed Matter Physics from the Institute of Physics, Chinese Academy of Sciences under the direction of Prof. Liquan Chen in 2006. After graduation, he joined the group of Prof. Ulrich Stimming as a postdoctoral research fellow at Technische Universität München (TUM), Germany; then Institute for Fuel Cell Innovation, National Research Council Canada as a Research Associate; and he worked as a postdoctoral research fellow with Prof. John B. Goodenough at The University of Texas at Austin in 2010–2011. His research interests include the synthesis and characterization of nanostructured materials and their applications in energy conversion and storage (fuel cells and lithium-ion batteries).

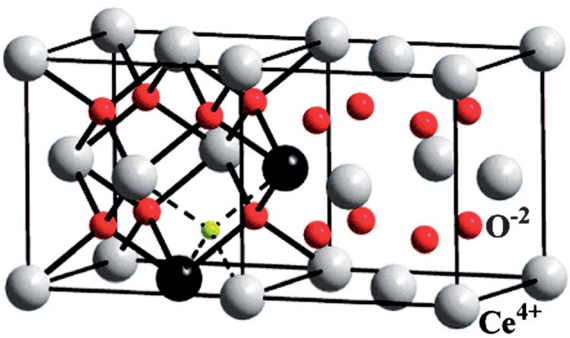

Fig. 1 The crystal structure of doped ceria. In the right cube, the undoped CeO_2 is shown, whereas in the left cube, two of the cerium ions are replaced by trivalent ions from the lanthanide series (dark spheres), between which an oxygen vacancy appears (indicated by a small sphere). (Reprinted from ref. 31 with permission from the Copyright (2006) National Academy of Sciences, USA).

Table 1 Some physical properties of pure stoichiometric CeO_2 (ref. 32–36)

Property		Value/unit
Lattice parameter		$a = 5.411$ Å
Molar mass		172.12 g mol^{-1}
Molar volume		0.158 nm
Density[32]		7.22 g cm^{-3}
Melting point[32]		*ca.* 2750 K
Boiling point		*ca.* 3773 K
Solubility in water		Insoluble
Specific heat[32]		*ca.* 460 J kg^{-1} K^{-1}
Thermal conductivity[32]		*ca.* 12 W m^{-1} K^{-1}
Refractive index[32]		*ca.* 2.1 visible
		ca. 2.2 infrared
Relative dielectric constant (0.5–50 MHz)[32]		11
Youngs' modulus[32]		*ca.* 165 × 10^9 N m^{-2}
Poisson's ratio[32]		*ca.* 0.3
Hardness[32]		5–6
Electronic conductivity (25 °C)[33]		2.48 × 10^{-8} S cm^{-1}
Ionic conductivity	(1000 °C, in air)[34,35]	3.13 × 10^{-3} S cm^{-1}
	(600 °C, in air)[34]	4.08 × 10^{-5} S cm^{-1}
	(600 °C, in H_2)[34]	1.11 × 10^{-3} S cm^{-1}
Formation energy (25 °C, 1 atm)[36]		−1025.379 kJ mol^{-1}
Magnetic susceptibility (χ_{mol})[36]		26 × 10^{-6} cm^3 mol^{-1}

when oxygen vacancy associates form because only these "free" vacancies are mobile and can contribute to oxygen ion transport in the solid solutions.[41]

Oxygen vacancies play significant roles in the reactivity of the cerium oxide surface for the catalytic oxidation of carbon monoxide.[42–44] This enhanced activity is often attributed to the oxygen storage capacity (OSC) of ceria, which is closely linked to how easily the cerium can change oxidation states. This is partially due to the similar energy of the 4f and 5d electronic states and low potential energy barrier to electron density distribution between them.[45] The valence state of the cerium is commonly discussed using the ratio Ce^{3+}/(Ce^{3+} + Ce^{4+}) (hereafter Ce^{3+} fraction).[46,47] The formation of oxygen vacancy defects results from a decrease in the oxygen content in the cerium oxide. Since oxygen has an oxidation state of 2^- in the stoichiometric CeO_2, ceria with a high density of oxygen vacancy defects is expected with an increase in its Ce^{3+} fraction in order to maintain the electroneutrality.[48,49]

Cerium oxides are excellent oxygen buffers because of their redox capability.[50] With alterations in the cerium oxidation state, CeO_2 forms oxygen vacancies or defects in the lattice structure by loss of oxygen and/or its electrons. The valence and defect structure of CeO_2 is dynamic and may change spontaneously or in response to physical parameters such as temperature, oxygen partial pressure, and doping with other ions,[51–53] as well as an electrical field,[54] or surface stresses.[55]

The effects of doping on the electrical properties of acceptor-doped CeO_2 have been well addressed in ref. 30 by Guo and Waser. In materials with high purity, the effect of the space-charge depletion layer is dominant; however, in materials of normal purity, the effect of the grain-boundary impurity phase is dominant.

An electrical field can be used to drive the redox process in CeO_2. The dynamic changes taking place during the electrically driven redox reaction were recently imaged by Wang's Group with an *in situ* high-resolution transmission electron microscopy, as shown in Fig. 2.[54] The reversible phase transformations due to the migration of oxygen vacancies have been reproducibly achieved. These results could lead to the low-temperature operation of catalysts by means of the electrical field for the purification of automobile emissions of pollutants, oxygen generation, and intermediate-temperature solid oxide fuel cells, as well as catalytic reforming. Sekine *et al.*[56] investigated four catalytic reactions assisted with an electric field to promote the catalytic activity of CeO_2-based catalysts. In the presence of an electric field, four reactions of steam reforming of ethanol, decomposition of ethanol, water gas shift, and steam reforming of methane proceeded at a very low temperature of 150 °C. Conversion of the reactant was greatly increased and apparent activation energies for these four reactions were lowered by implementing the electric field to the catalyst bed. This process can produce hydrogen and syngas by using a considerably small energy and has a quick response.

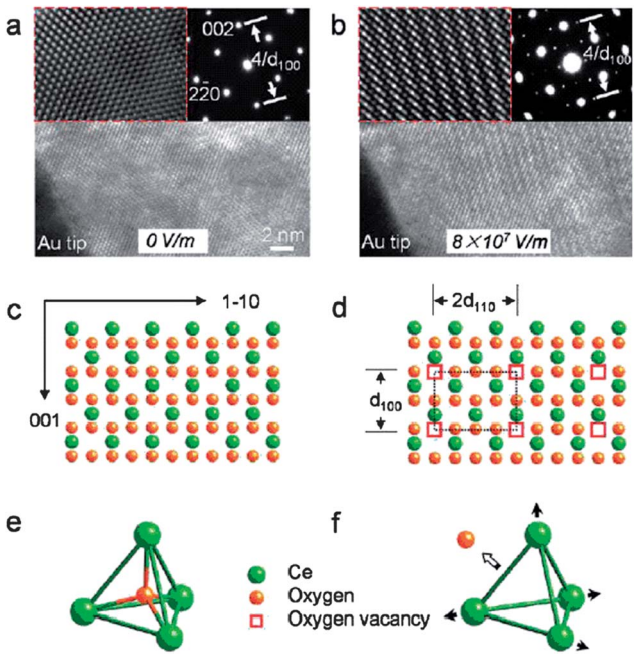

Fig. 2 (a) *In situ* TEM image of a single-crystal CeO_2 film along the ⟨110⟩ zone axis. The enlarged HRTEM image and the corresponding SAED pattern are shown in the upper left and the upper right insets, respectively. d_{100} is the interplanar spacing of the (100) plane of CeO_2. (b) The wave-sweeping patterns appeared when a bias of 6 V ($E \approx 8 \times 10^7$ V m^{-1}) was applied across the CeO_2 film, indicating the decomposition of the cerium oxide. Superlattice reflections (upper left) and extra diffraction spots (upper right) were observed in this case. (c) Solid-sphere model of CeO_2 in a perfect fluoride structure. This drawing represents the projection along the ⟨110⟩ direction. (d) Solid-sphere model showing the formation of oxygen vacancies. The rectangles indicate the vacancy superlattices. (e) Cerium oxide can be viewed as tetrahedral with cations at the corners and oxygen anions at the centers. (f) Cerium oxide with an oxygen vacancy will cause the CeO_2 film cations to repel each other because of coulombic interactions. The arrowhead indicates the displacement direction of the oxygen anion. (Reprinted with permission from ref. 54. Copyright 2010 American Chemical Society).

Space charge models are widely used to describe the electrochemical behavior of surfaces and interfaces in ionic solids[57,58] which are based on the fact that defect formation energies at surfaces differ from those in the bulk. This leads to an electric gradient near the surface, to maintain a thermodynamic equilibrium. The width of this space charge region is related to the Debye screening length,[24,58,59] which is determined by charge carrier concentration. Sheldon and Shenoy[55] recently found that near-surface variations in point defects can induce stresses that are large enough to significantly alter thermodynamic equilibrium (Fig. 3). Volume changes related to point defects in space charge layers can produce strains significantly changing the thermodynamic equilibrium near surfaces in ionic solids.[55] For example, near-surface compressive stresses exceeding −10 GPa have been predicted for ceria by Sheldon *et al.*[55] The magnitude of this effect is consistent with anomalous lattice parameter increases that occur in ceria nanoparticles.[60,61] These stresses should substantially alter defect concentrations and key transport properties in a wide range of materials. De Souza *et al.*[62] employed static atomistic simulations, based on empirical pair-potentials (EPP) to determine the effect of strain on the energetic barriers for oxygen-vacancy migration in CeO_2-based electrolytes. They found that a biaxial, tensile strain of 4% may increase the in-plane conductivity at $T = 500$ K by about four orders of magnitude. Space-charge accumulation is unlikely to enhance significantly the conductivity of a CeO_2–M_2O_3 (M = Gd, Sm) fluorite material.

Besides optimizing the composition, tailoring of the microstructure can also be used to increase the conductivity of oxides. Two strategies are usually adopted: (1) increasing the density of homo-interfaces (grain boundaries) drastically, by moving from microcrystalline to nanocrystalline; (2) creating specific hetero-interfaces, by employing epitaxial thin-film geometries.[62] A conductivity increase of about one order of magnitude in Gd-doped CeO_2 and ZrO_2 layers with increasing the number of interfaces by decreasing the thickness of the layer to 15 nm (Fig. 4) has been observed by Azad *et al.*[63] TEM observation revealed dislocations both at the interface and in the layers, regardless of the number of interfaces. However, the dislocations at the interfaces were separated by a distance much longer than

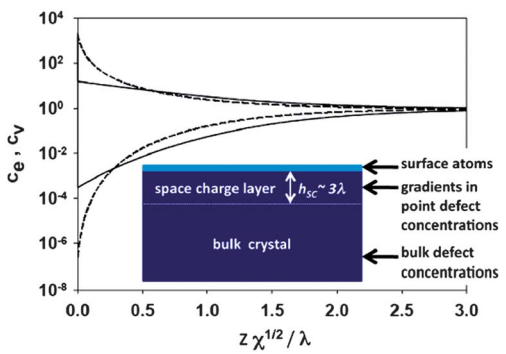

Fig. 3 The solid lines show the defect concentration profiles. Total strain is divided into oxygen vacancy (subscript V) and extra electron (subscript e) contributions. χ is the bulk nonstoichiometry in $CeO_{2-\chi}$. h_{SC} is typically 2 to 3 times the Debye length, $\lambda/\sqrt{\chi}$. The analogous results without considering stress contributions are shown as dashed lines. (Reprinted from ref. 55 with permission from American Physical Society.)

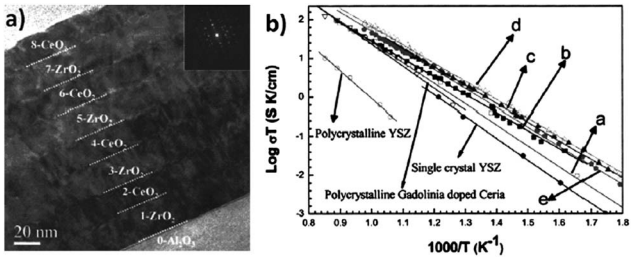

Fig. 4 (a) TEM image showing a cross-sectional view of an eight-layer Gd_2O_3-doped CeO_2 and ZrO_2 film grown on Al_2O_3 (0001), (b) Arrhenius plots of oxygen ionic conductivity of two-(a), four-(b), eight-(c), ten-(d), and sixteen-layer (e) gadolinia-doped ceria–zirconia thin films. (Reprinted from ref. 63 with permission from American Institute of Physics.)

that expected considering the lattice mismatch between the two phases. The authors explained this finding by considering the highly textured structure of the layers (epitaxially (111)-oriented) and that the lattice misfit was also accommodated by the dislocations formed in the layer bulk.[63,64] However, the conductivity decreased for the layer thickness below 15 nm. It is attributed to the lattice strain and extended defects due to the lattice mismatch.[63]

2.2. Nano-size effects

With a decrease in particle size, ceria nanoparticles demonstrate the formation of more oxygen vacancies.[47,65] The large surface area to volume ratio existing in a nanoparticle enables CeO_2 to act catalytically, commonly resulting in unique properties. For example, ceria nanoparticles (NPs) of diameter about 3–4 nm supporting Au lead to an increase of two orders of magnitude in the catalytic activity for CO oxidation with respect to the Au–CeO_2 catalysts prepared by coprecipitation or by Au deposition on a regular bulk cerium oxide support.[66] Ceria nanoparticles with a similar size were also shown to supply reactive oxygen from the NPs to the supported gold species.[67] These results imply that the O vacancy formation energy (E_f) in ceria crystallites of a particular size becomes lower than that in extended structures in order to enable such an extraordinary increase of the NP reactivity at low temperature.[68] The properties of the support can change drastically with the particle size decreasing to the nanosize region, turning an inactive support into a highly active species. These examples clearly demonstrate it is feasible to tune the specific reactivity of ceria nanoparticles by controlling their size.

Moreover, nanocrystalline CeO_2 materials also possess some other new properties compared to the coarsened bulk materials, such as the enhanced electronic conductivity,[69,70] Raman-allowed modes shifting and broadening,[71] the size-induced lattice relaxation,[60,61] the pressure-induced phase transformation,[72] and the blue shift in ultraviolet absorption spectra.[73] The interested reader can refer to these references and references therein.

3. Synthesis

During the last two decades, much effort has been devoted to preparing CeO_2 nanoparticles and films. The methods include hydrolysis,[74] precipitation,[71,75–77] thermal deposition,[78]

combustion or flame-synthesis,[79,80] sol–gel,[20,81] hydrothermal or solvothermal,[82,83] microemulsion method,[84,85] gas condensation,[86] sonochemical synthesis,[87] electrochemical synthesis,[88] and so on. It is generally believed that the evolution of a solid from a solution phase involves two steps in crystallization: nucleation and growth.[89] Important shape guiding parameters for the construction of nanocrystal architectures have been discussed by Cheon *et al.*[90] The nucleating seeds, kinetic control, temperature, and selective activation energy modulations of surfaces through the use of capping molecules have been found to be crucial for the anisotropic growth.[90] By delicately balancing and controlling these parameters, it is possible to control the shapes of nanocrystals. Highly active ceria based catalysts can be rationally designed by controlling the synthesis process to produce desired morphologies and microstructures with controlled oxygen vacancies.

3.1. One-dimensional nanostructured CeO_2

One-dimensional (1D) nanostructured CeO_2 has been intensively investigated due to their novel physical properties and potential applications. 1D nanostructured materials, such as nanowires, nanorods, and nanotubes, offer opportunities for fundamental research concerning the influence of size and dimensionality of a material on its physical and chemical properties.[91] They may also be promising building blocks for nanoscale devices. CeO_2 nanowires/rods first synthesized by using hard templates, such as porous anodic alumina membranes.[92,93] To obtain 1D nanostructures by anisotropic growth, the crystal growth pathway can also be controlled thermodynamically and kinetically with different mediators, *e.g.*, solvents, surfactants, mineralizers, concentration, temperature, *etc.* Our group, for the first time, reported polycrystalline CeO_2 nanowires that were synthesized *via* a solution-phase route with sodium bis(2-ethylhexyl) sulfosuccinate as a structure-directing agent.[94] The HRTEM image indicates clearly that the nanowires are composed of many tiny grains at different orientations (Fig. 5). The porous nanowires may enable the gas to access all the surfaces of CeO_2 nanoparticles contained in the device unit.

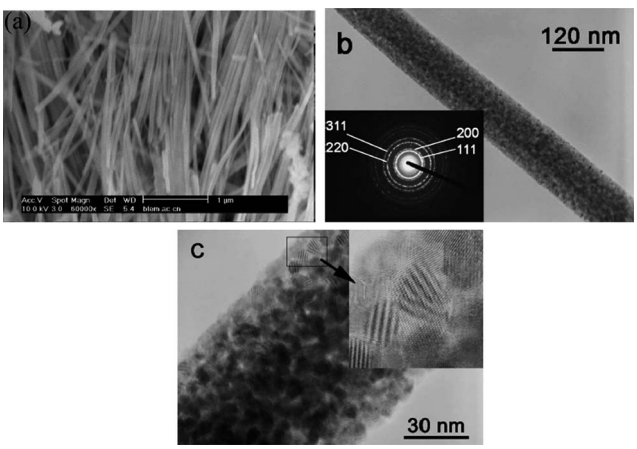

Fig. 5 Typical SEM (a), TEM (b) and HRTEM (c) images of the CeO_2 nanowires, the inset in (c) is the SAED pattern of single CeO_2 nanowires. (Reprinted from ref. 94 with permission from Chemical Society Japan.)

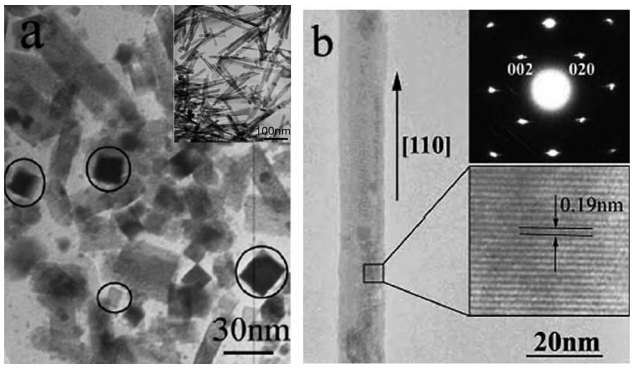

Fig. 6 (a) The cross-sectional TEM image of the CeO_2 nanorods, the inset shows a low magnified TEM image; (b) HRTEM image of a typical CeO_2 nanorod, the upper right inset shows a selected area electron diffraction (SAED) pattern, and the lower inset shows a magnified view of the selected area of the nanorod. (Reprinted from ref. 98 with permission from Elsevier Ltd.)

CeO_2 nanorods were also prepared by solvothermal methods.[95–98] A typical cross-sectional TEM image of the CeO_2 nanorods is shown in Fig. 6a.[98] It clearly presents their rectangular cross section, indicating that each nanorod has four side surfaces. Fig. 6b shows the as-prepared CeO_2 nanorods are single crystalline and the preferential growth direction is [110].

Fig. 7a shows a 2D crystal lattice image of one typical nanorod with a growth axis perpendicular to the electron beam. It

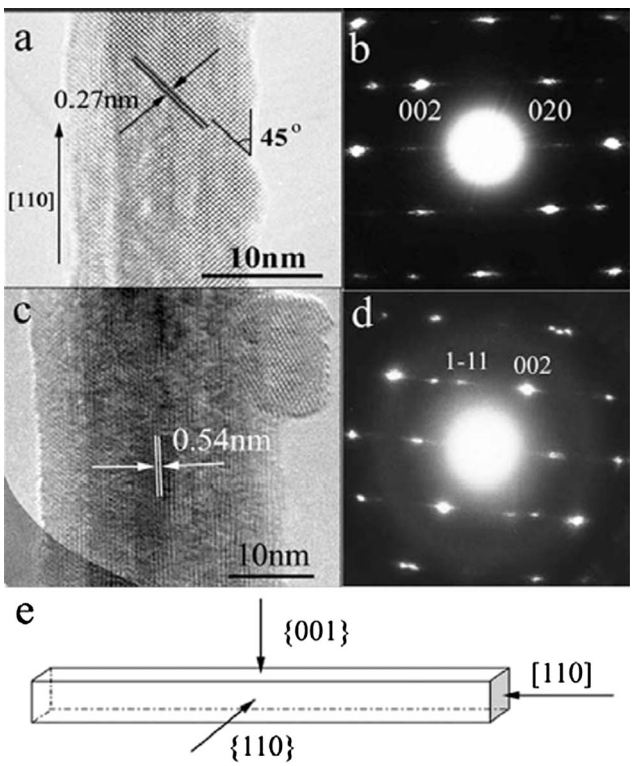

Fig. 7 (a) The magnified HRTEM image of a typical nanorod view along [001] direction, (b) the SAED pattern of (a); (c) the magnified HRTEM image of a typical nanorod view along [110]; (d) the SAED pattern of (c); (e) the structural models of CeO_2 nanorods. (Reprinted from ref. 98 with permission from Elsevier Ltd.)

indicates that CeO_2 nanorods have well-defined reactive planes {001} and {110} planes.[98] This study also indicated that the catalytic activity toward CO oxidation was greatly influenced by the specific crystal planes and oxygen vacancy clusters with larger sizes.[98]

Han *et al.*[99] synthesized ceria nanotubes *via* a two-step procedure: precipitation at 100 °C and aging at 0 °C for a long time (45 days). As shown in Fig. 8, there are two kinds of 1 D nanostructures of CeO_{2-x}, the nanowires with consistent lattice across and the nanotubes with a cylindrical geometry. Tang *et al.*[100] prepared layer-structured rolling $Ce(OH)_3$ nanotubes through an alkali thermal-treatment process under oxygen-free conditions and ceria nanotubes by annealing $Ce(OH)_3$ in a reducing atmosphere. However, these methods were either time-consuming or required special equipment.

Zhou *et al.*[101] reported a facile rational synthesis of CeO_2 nanotubes with large cavities and thin walls by a simple oxidation-coordination-assisted dissolution process of the $Ce(OH)_3$ nanotubes/nanorods, as shown in Fig. 9.

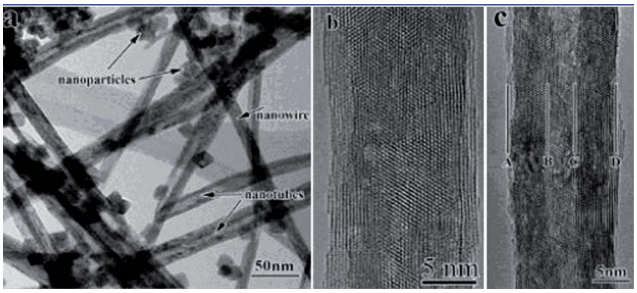

Fig. 8 (a) Typical morphology of the sample. There are three kinds of nanostructures: nanoparticles, nanowires, and nanotubes as marked in the figure. (b) High-resolution image of a nanowire. (c) High-resolution image of a nanotube. The thickness of the wall of the nanotube is about 5.5 nm by measuring the spacing between lines A and B or lines C and D. (Reprinted with permission from ref. 99. Copyright 2005 American Chemical Society.)

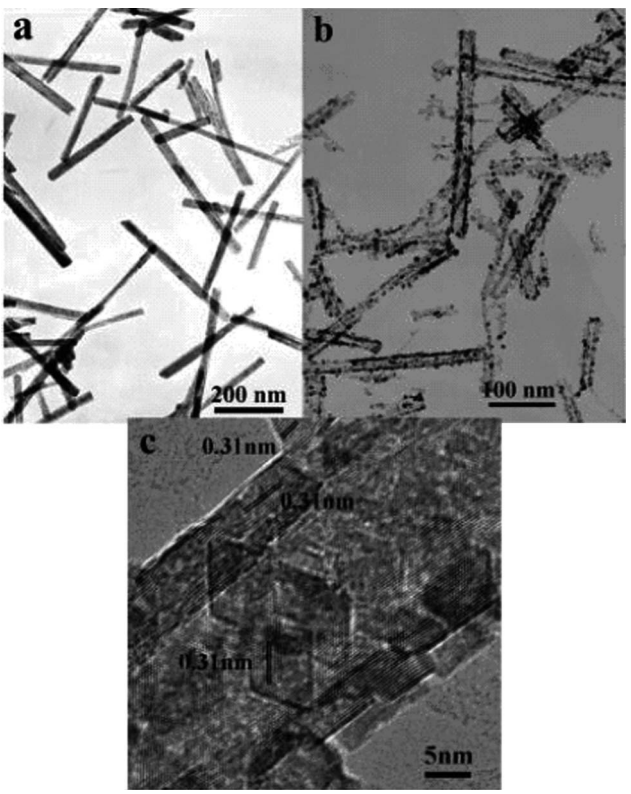

Fig. 9 (a) TEM image of the newly prepared 1D $Ce(OH)_3$. (b) TEM image of the CeO_2 nanotubes synthesized *via* the oxidation-coordination-assisted dissolution process. (c) High-resolution TEM image of the CeO_2 nanotube. (Reprinted with permission from ref. 101. Copyright 2007 American Chemical Society.)

3.2. 2D and 3D nanostructured CeO_2

Shape- and size-controlled synthesis of ceria nanocubes bounded by six {200} planes were prepared by Gao's group through a rational one-pot approach.[102] Fig. 10 shows two- and three-dimensional self-assemblies of NPs on Si substrates induced by slow evaluation of the particle dispersion. Both shape and size of the ceria NPs can be tuned more conveniently by changing the concentration of the reactants, the amount of stabilizing agents and the water/toluene ratio in the reaction system. Due to the presence of oriented aggregation mediated precursor growth, the synthesized ceria nanocubes exhibit fantastic structural properties (rough {200} surfaces).[102]

Highly dispersible and crystalline rare-earth oxide nanopolyhedra, nanoplates, and nanodisks were synthesized in oleic acid/oleylamine solvents by Yan's group *via* a thermolysis of their benzoylacetonate complexes, as shown in Fig. 11.[103] The

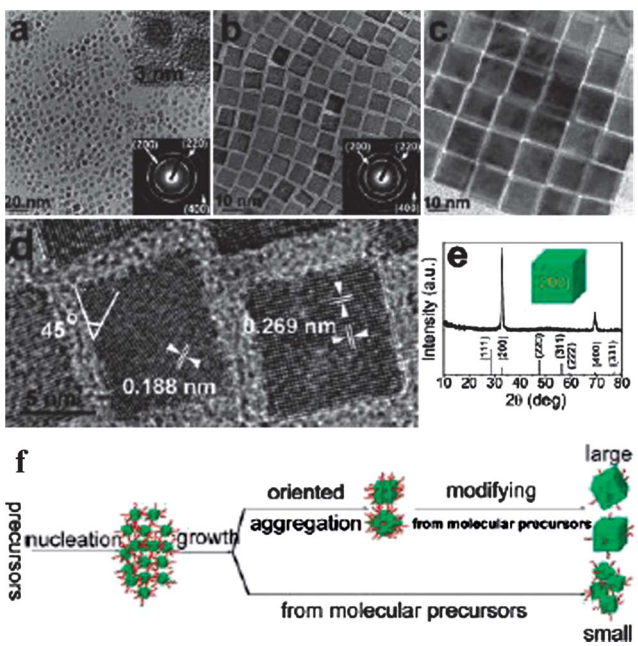

Fig. 10 TEM images of ceria nanocubes with the average sizes of (a) 4.43, (b) 7.76, and (c) 15.65 nm, the insets are SAED patterns of individual NPs; (d) HRTEM image of the ceria nanocubes; (e) a typical XRD pattern of the ceria nanocubes assembled on a Si wafer; (f) schematic illustration of the oriented aggregation mediated precursor growth mechanism of colloidal NPs. (Reprinted with permission from ref. 102. Copyright 2006 American Chemical Society).

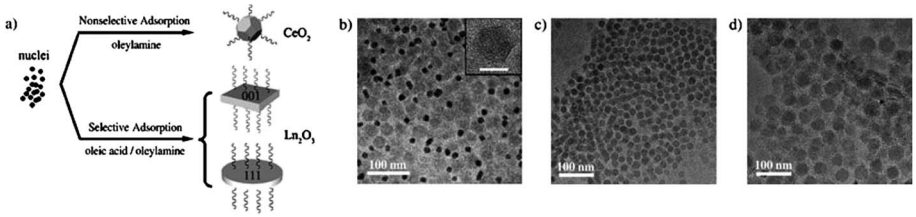

Fig. 11 (a) Formation of rare-earth oxide nanopolyhedra, nanoplates, and nanodisks. (b)–(d) TEM images of the as-obtained Eu_2O_3: (b) OA/OM = 1 : 7, 310 °C, 1 h (inset: HRTEM image of an Eu_2O_3 nanoparticle; scale bar: 10 nm); (c) OA/OM = 3 : 5, 310 °C, 20 min; (d) OA/OM = 3 : 5, 330 °C, 1 h. (Reprinted from ref. 103 with permission from John Wiley and Sons.)

obtained products with different morphologies were dependent on the nature of metal cations and the selective adsorption effects of the solvents employed. These nanocrystals also exhibit a striking ability to self-assemble into large-area nanoarrays.

Hyeon *et al.*[104] synthesized uniform-sized ceria nanocrystals with quasispherical, wire, and tadpole shapes from the non-hydrolytic sol–gel reaction of cerium(III) nitrate and diphenyl ether in the presence of appropriate surfactants, as shown in Fig. 12.

2D nanoplates and nanosheets have been paid a lot of attention in recent years because of their special properties. Recently, Murray *et al.* reported a simple solution-phase synthetic method to prepare ultrathin ceria nanoplates in the presence of mineralizers, as shown in Fig. 13.[105] The morphology of nanoplates can be easily controlled by changing reaction parameters, such as precursor ratio, concentration, and reaction time, *etc.* The obtained CeO_2 nanoplates have higher theoretical surface-area to volume ratio and desirable (100) surfaces, exhibit much higher oxygen storage capacity than that of 3D CeO_2 nanomaterials prepared by other methods. The key to this synthesis of ceria nanoplates is the incorporation of a mineralizer (sodium diphosphate) that accelerates the crystallization process and controls the morphology of ceria nanocrystals. In the absence of mineralizers, the yield of ceria nanocrystals is very low, and the morphologies are not controlled.[105]

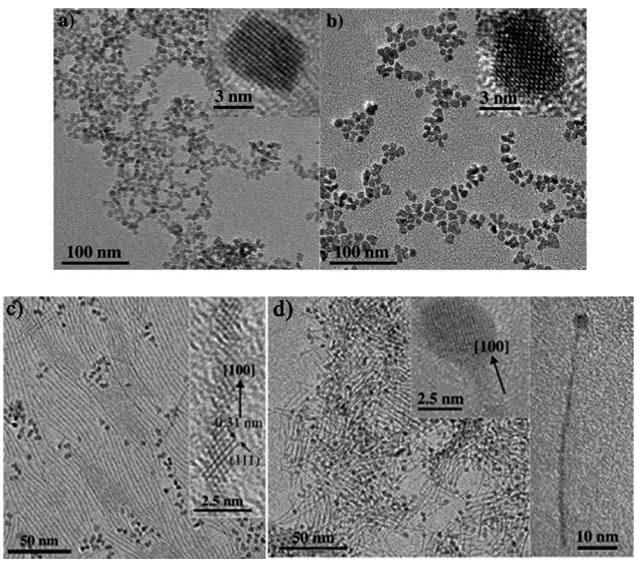

Fig. 12 TEM images of (a) 3.5 nm spherical ceria nanocrystals and (b) 5.2 nm spherical ceria nanocrystals. Insets are their HRTEM images. (c) TEM images of 1.2 × 71 nm wire-shaped ceria nanocrystals. The inset is the HRTEM image of a wire-shaped nanocrystal. (d) TEM images of the tadpole-shaped ceria nanocrystals. The inset is the HRTEM image of a tadpole shaped nanocrystal. (Reprinted from ref. 104 with permission from John Wiley and Sons, Inc.)

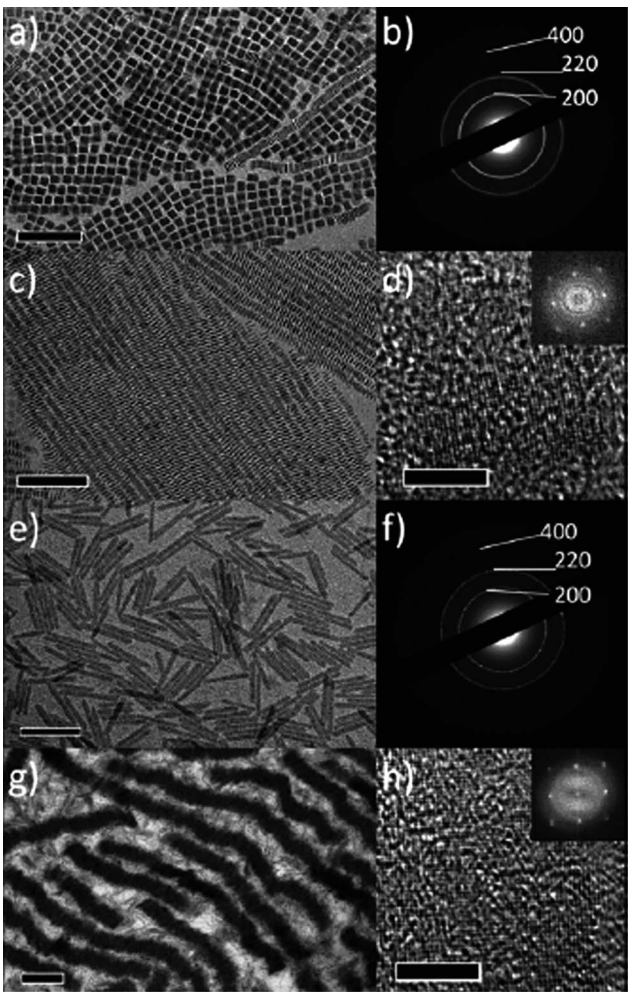

Fig. 13 (a) TEM image and (b) SAED pattern of square ceria nanoplates; (c) TEM image of stacking square ceria nanoplates and (d) HRTEM image of a square ceria nanoplate; (e) TEM image; (f) SAED pattern and (h) HRTEM image of elongated ceria nanoplates. Insets of (d) and (h): fast Fourier Transform (FFT) patterns of HRTEM images. Scale bars: (a and c) 100 nm, (e and g) 200 nm, (d and h) 5 nm (Reprinted from ref. 105 with permission from John Wiley and Sons, Inc.).

Ultrathin, single-crystalline ceria nanosheets with a thickness of approximately 2.2 nm and lateral dimension up to 4 μm were synthesized by Xia's group with a simple aqueous route, as shown in Fig. 14.[106] They found that the ceria nanosheets were formed through 2D self-organization of initially formed small ceria nanocrystals, followed by an *in situ* recrystallization process. The slow addition of a cerium(III) nitrate precursor using a syringe pump is critical to the formation of ceria nanosheets.

Tong *et al.*[107] developed an electrochemical deposition route for the preparation of hierarchically porous ceria and Gd-doped ceria (Fig. 15) at room temperature, providing a facile and low-cost route for the synthesis of porous ceria and Gd-doped ceria foam nanostructures in high yield. The as-prepared hierarchically porous Gd-doped CeO_2 nanostructures have shown a remarkable enhancement of optical and magnetic properties.

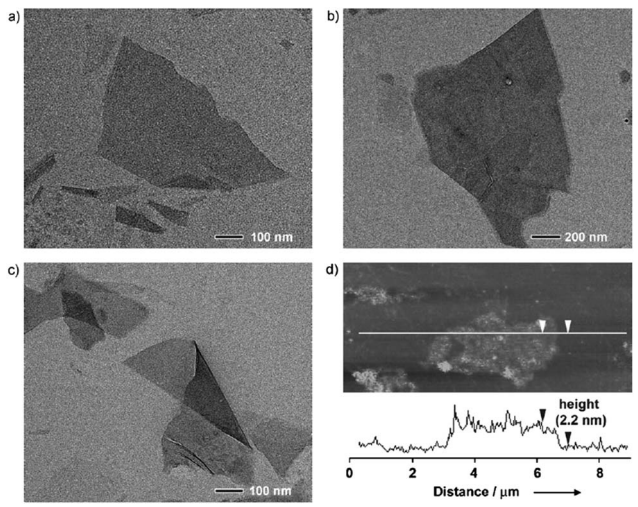

Fig. 14 (a and b) TEM images of ceria nanosheets with different sizes, (c) TEM image of a self-folded nanosheet, (d) tapping-mode AFM image and the height along the line shown in the AFM image. (Reprinted from ref. 106 with permission from John Wiley and Sons, Inc.)

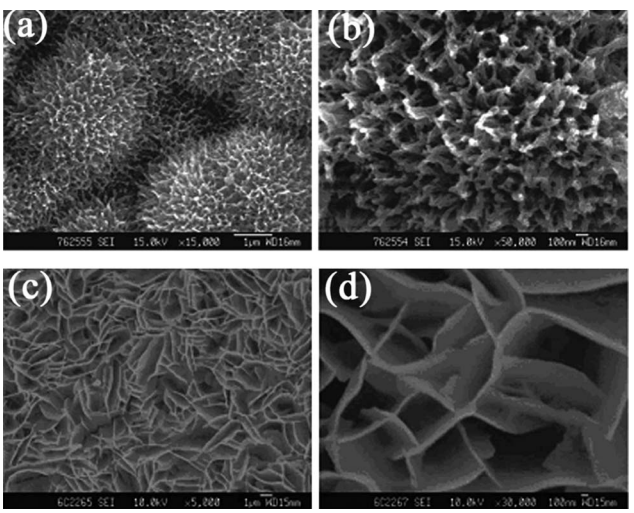

Fig. 15 SEM images of the porous CeO_2 (a and b) and Gd-doped CeO_2 (c and d) prepared by an electrochemical deposition route. (Reprinted with permission from ref. 107. Copyright 2009 American Chemical Society).

Mesoporous ceria has shown great potential as versatile catalysts and catalyst supports due to its high surface area and the increased dispersion of active secondary components.[108–110] However, a major problem is its poor thermal stability, which is often caused by structure collapse during surfactant removal at elevated temperatures.[111] Therefore, mesoporous CeO_2 with an excellent thermal stability is highly desired for designing high-performance catalysts. To address this issue, a novel hydrothermal method has been developed by our group in IOP to prepare monodisperse flowerlike CeO_2 microspheres with micro/nano structure, as shown in Fig. 16.[112] The obtained CeO_2 microspheres have open three-dimensional (3D) porous and hollow structures consisting of nanosheets as the petals with an average thickness of about 20 nm (Fig. 17a–d). They possess high surface area (92.2 $m^2\ g^{-1}$), large pore volume (0.17 $cm^3\ g^{-1}$), and marked hydrothermal stability. By means of the results of morphology and phase evolution of the products obtained under different reaction times as well as GC-MS analysis of the liquid products, a formation mechanism of the flowerlike CeO_2 microspheres was proposed, mainly consisting of four processes of simultaneous polymerization–precipitate reaction, metamorphic reconstruction and mineralization under hydrothermal condition, and subsequent controlled calcinations, schematically shown in Fig. 16e. This method has been generalized to prepare flowerlike La_2O_3 (ref. 113) and a series of elements-doping CeO_2 microspheres.[114] The large surface area endows this material with high reactivity in CO oxidation[114–117] and hydrocarbons reforming.[112,118] The excellent kinetics property was demonstrated in a SOFC by applying a Ru-loaded flowerlike ceria catalyst layer in the anode side.[119] Moreover, Sm-doped ceria microspheres combined with Ag was found highly reactive for

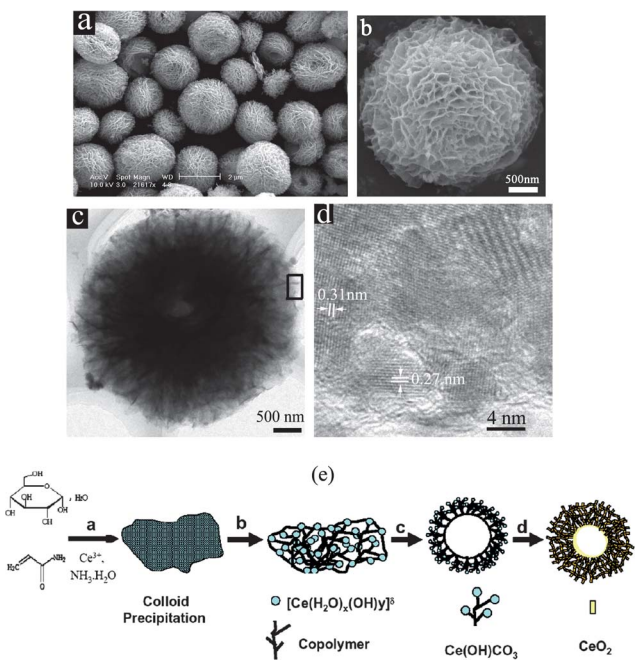

Fig. 16 Representative SEM images (a and b) and TEM images (c and d) of the flowerlike CeO_2 microspheres; (e) schematic illustration of the evolution of flowerlike CeO_2 microspheres. (Reprinted with permission from ref. 112. Copyright 2006 American Chemical Society).

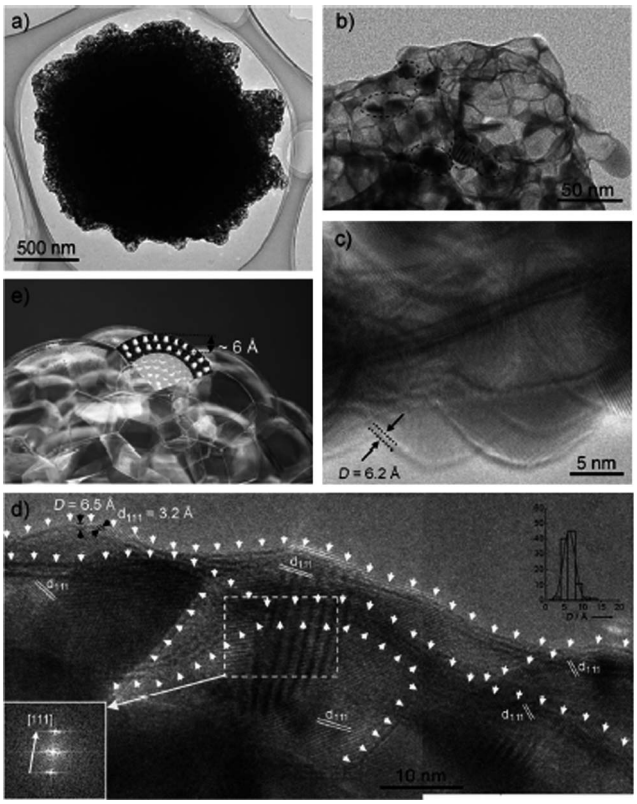

Fig. 17 (a and b) Typical TEM images with different magnification. (c and d) Typical high-resolution TEM images. (e) Digital camera photograph of soap bubbles as a model of the wall of CeO_2 foam inserted. Insets in (d): FFT patterns obtained from the HRTEM image and statistical analysis of thickness distribution of walls of CeO_2 foam (average D = 6.41 Å, relative standard deviation (22.5%) derived from counting 50 walls and two different points of each wall were measured). (Reprinted from ref. 121 with permission from John Wiley and Sons, Inc.)

oxygen reduction reaction as a cathode in intermediate temperature solid oxide fuel cells.[120]

Similar to the morphology of the flowerlike CeO_2 microspheres, Yang *et al.*[121] recently reported a thermal decomposition process to fabricate three-dimensional CeO_2 foams with long-range atomically thin single-crystalline walls (4–8 Å) under an ammonia atmosphere, using scheelite-type $CeGeO_4$ as a starting material, as shown in Fig. 17. The obtained CeO_2 foams have a BET surface area of 60.1 $m^2\ g^{-1}$ and a pore volume of 0.19 $cm^3\ g^{-1}$. The feasibility and reaction pathways of nitridation process were analyzed by first-principles calculations, which indicated that O element on the {101} facets of orthogermanate $CeGeO_4$ can be removed by NH_3 as a result of forming Ce^{3+} and Ge^{2+}. The Ge^{2+} may be gasified as GeO at high temperature, which leads to the decomposition of the $CeGeO_4$ crystals and formation of CeO_2 foams.

The nanocasting pathway with hard templates opens the door to the design of highly porous solids with multifunctional properties and interesting application perspectives.[122] Nanocasting is a process in which a template with relevant structures on the length scale of nanometers is filled with another material to be cast or a precursor for it, and the initial template is subsequently removed.[122] The nanocasting method for CeO_2 which employed uniform mesoporous silica as a hard template, pioneered by the group of Ryoo, allowed synthesis of highly ordered thermally stable mesoporous CeO_2 with nanocrystalline walls (Fig. 18) for the first time.[123] Recently, ordered mesoporous CeO_2 was also prepared by Ji *et al.* with nanocasting from cubic *Ia3d* mesoporous MCM-48 silica (Fig. 19).[124] The obtained mesoporous CeO_2 shows a blue shift in UV-vis absorbance and has many more surface vacancies due to the controlled nanocrystal size. Compared with the corresponding nonporous analogues and standard reference of TiO_2 materials, the

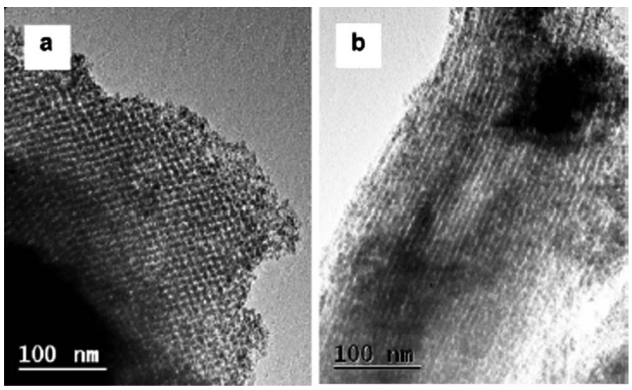

Fig. 18 TEM images of the template-free CeO_2 samples synthesized with cubic *Ia3d* silica template (a), and with 2D hexagonal *p6mm* template (b). The image in (a) shows a high similarity with images taken along the [110] direction of cubic *Ia3d* mesoporous carbons, and the image in (b) corresponds to the [100] direction of the *p6mm* structure. (Reprinted from ref. 123 with permission from Royal Society of Chemistry).

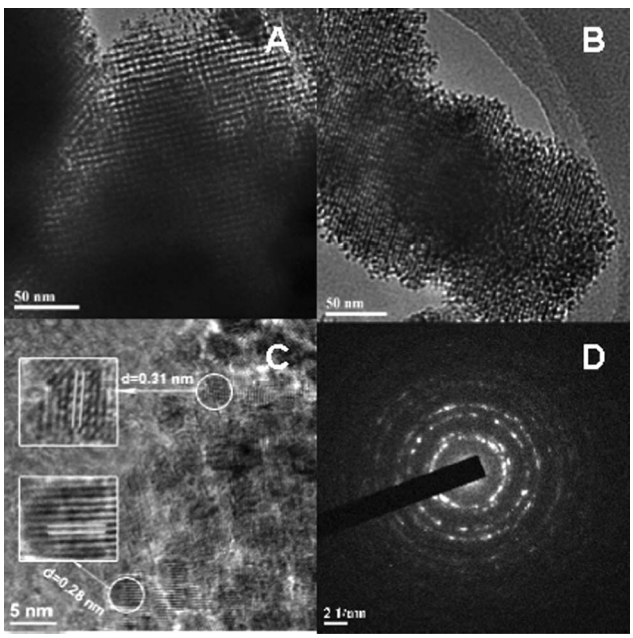

Fig. 19 (A and B) TEM images of the template-free CeO_2 sample calcined for 2 h at 550 °C. (C) The HRTEM image of the CeO_2 sample showing its nanocrystalline nature. (D) The SAED pattern confirming the crystallinity of the porous materials. (Reprinted with permission from ref. 124. Copyright 2008 American Chemical Society).

mesoporous material shows significantly increased catalytic activity toward acid orange 7 (AO7) decomposition, a nonbiodegradable azodye and target contaminant to test photocatalytic activities under visible light irradiation.

Chane-Ching *et al.* developed a general two-step assembly approach for the synthesis of ordered 2D or 3D nanostructured materials (Fig. 20) with a large surface area through the self-assembly of functionalized nanoparticles.[125] In their work, ceria nanoparticles are functionalized by using the (CH_2CH_2O) groups of the surfactant. Based on the cooperative self-assembly of colloidal nanoparticles, hexagonal arrays of CeO_2 are obtained and the symmetry of the arrays was preserved upon heating up to 500 °C.

Yuan *et al.* prepared a highly ordered mesoporous $Ce_{1-x}Zr_xO_2$ solid solution with a 2D hexagonal mesostructure,[126] as shown in Fig. 21. The general synthesis strategy is based on a sol–gel process combined with evaporation-induced self-assembly in ethanol using block copolymer Pluronic P123 as the template and ceric nitrate and zirconium oxide chloride as the precursors without additional acid or base. Under the optimized temperature and humidity conditions, a series of mesoporous $Ce_{1-x}Zr_xO_2$ with different Ce/Zr ratios can be obtained.

Spherical and nearly cubic-like monodispersed ceria colloid nanocrystals (Fig. 22) have been prepared by Li's group with a simple hydrolysis process in glycol.[127] Subsequently, $Ce_{1-x}Zr_xO_2$ and $CeO_2@Ce_{1-x}Zr_xO_2$ nanocages with different outer and interior morphologies have been prepared with the colloid ceria cluster as both chemical precursors and physical templates by Kirkendall effect. This approach has shown great flexibility in controlling the sizes, shapes, and compositions of the solid solution.[127]

The interaction of metals with ligands is a key factor in the design of catalysts. Much effort has been devoted to the rational control of metal–ligand interactions in order to exploit their catalytic properties.[128] Mitsudome *et al.* recently reported a facile synthesis of the core–shell nanocomposite of $AgNPS@CeO_2$ by combining the reverse micelle technique and a redox reaction.[128] The SEM image of the $AgNPs@CeO_2$ showed uniformly spherical nanoparticles with a size of 30 nm in diameter

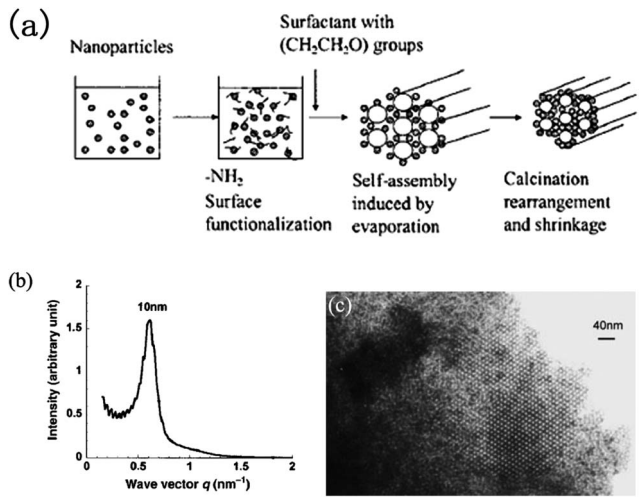

Fig. 20 (a) Schematic illustration of the synthetic route for the self-assembly of surface-modified nanoparticles, (b) small-angle X-ray scattering pattern and (c) TEM image of the assembled CeO_2 nanostructured material after calcination at 500 °C. (Reprinted from ref. 125 with permission from John Wiley and Sons, Inc.)

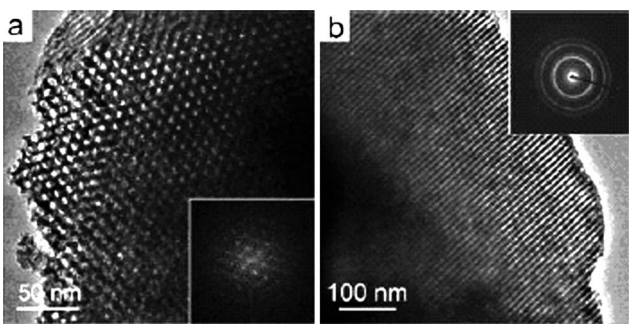

Fig. 21 TEM images of the mesoporous $Ce_{1-x}Zr_xO_2$ ($x = 0.5$) recorded along the [001] (a) and [110] (b) orientations. The inset in (a) is the corresponding FFT pattern, and the one in (b) is the corresponding SAED pattern. (Reprinted with permission from ref. 126. Copyright 2007 American Chemical Society).

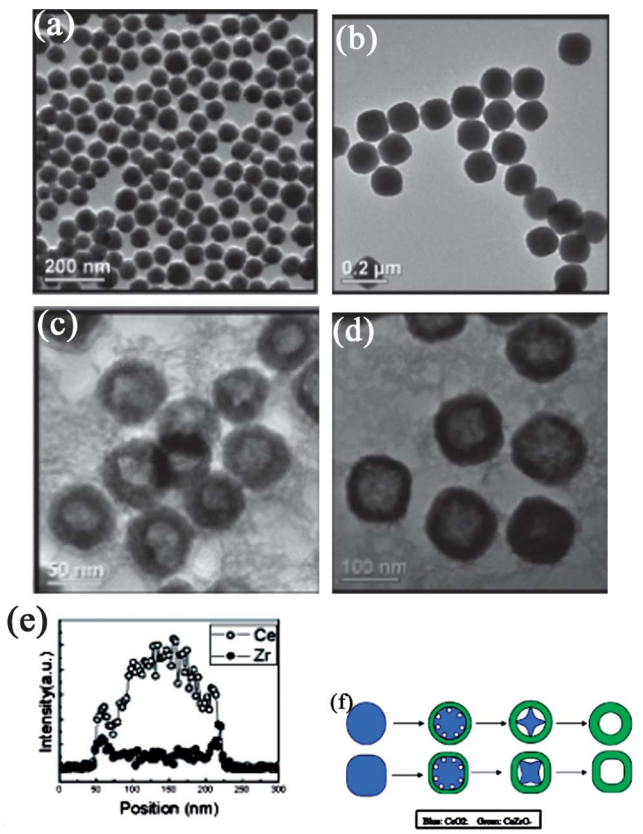

Fig. 22 (a) Typical TEM image of nearly monodispersed spherical ceria nanocrystal clusters obtained at low water concentration. (b) TEM image of nearly cubic-like ceria nanocrystal clusters obtained at high water concentration. (c) TEM image of spherical Ce–Zr–O nanocages. (d) TEM image of nearly cubic-like Ce–Zr–O nanocages. (e) Compositional line profile across a single hollow core–shell structure probed by EDS line scanning. (f) The illustration of formation process of the Ce–Zr–O nanocages based on Kirkendall effect. (Reprinted with permission from ref. 127. Copyright 2008 American Chemical Society).

(Fig. 23a). TEM image showed the two areas of an electron-dense core 10 nm in diameter and an electron-poor shell 8 nm thick (Fig. 23b). EDS analysis clearly indicated that the nanocomposite was composed of a Ag core and CeO_2 shell (Fig. 23c). Close inspection of the HRTEM image showed that the spherical CeO_2 NPs are about 3–5 nm in diameter and assemble to form the shell. The nanospace-containing shell structure enables the access of reactants to the active metal core. AgNPs@CeO_2 was demonstrated to be an effective catalyst for the complete chemoselective reduction of nitro compounds in the presence of C=C bonds using H_2 as a clean reductant. Moreover, AgNPS@-CeO_2 was applicable to the deoxygenation of epoxides to alkenes with higher selectivity (99%). Maximizing the interface interaction between AgNPs and basic sites of CeO_2 by the construction of core–shell AgNPS–CeO_2 successfully induces the heterocatalytic cleavage of H_2 and leads to the development of highly chemoselective catalytic reduction of polar functionalities.[128]

Wei *et al.* recently prepared a series of catalysts of three-dimensionally ordered macroporous (3 DMO) $Ce_{0.8}Zr_{0.2}O_2$-supported gold nanoparticles with controllable sizes using a facile method of gas bubbling-assisted membrane reduction (GBMR).[129] All the catalysts have well-defined 3DOM structures, which consist of interconnected networks of spherical voids (Fig. 24), and the Au nanoparticles are well dispersed and supported on the inner wall of the uniform macropores. 3DMO $Au_{0.04}/Ce_{0.8}Zr_{0.2}O_2$ catalyst with Au particle size of 2–3 nm has the strong capability of adsorption and activation of oxygen. Thus, it exhibits superior catalytic activity for diesel soot oxidation, especially at low temperatures.

Ceria nanoparticles are one of the key abrasive materials for chemical-mechanical polarization of advanced integrated circuits. However, undoped CeO_2 nanocrystals usually show polyhedral shapes, which scratch the silicon wafers and increase defect concentrations.[16] Wang *et al.* synthesized ceria nanospheres doped with 12 atomic% of Ti using flame spray pyrolysis of a solution of cerium and titanium precursors dissolved in a flammable solvent alcohol. Upon doping with Ti, the ceria nanocrystals are spherical and polishing defects are reduced by

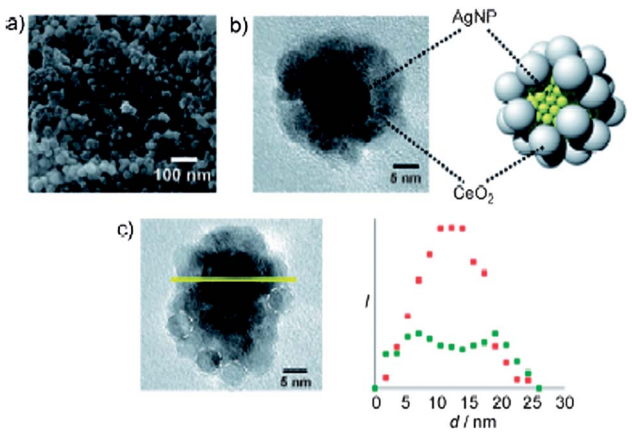

Fig. 23 (a) SEM image of AgNPs@CeO_2. (b) HRTEM image of the single AgNPs@CeO_2 nanocomposite. (c) The line-scan STEM-EDS across the AgNPs@CeO_2 nanocomposite (Ag: red squares, Ce: green squares). The circled areas correspond to the spherical CeO_2 NPS shell. (Reprinted from ref. 128 with permission from John Wiley and Sons.)

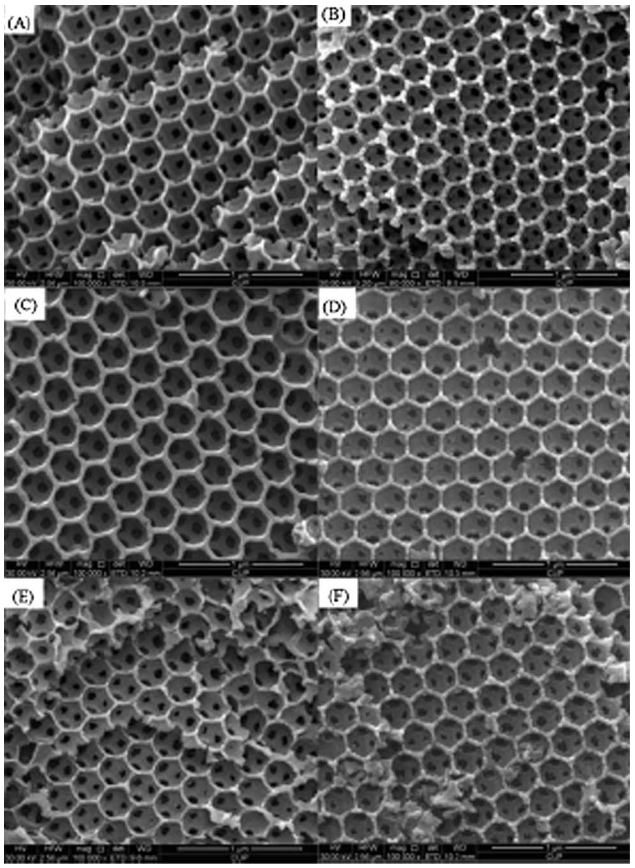

Fig. 24 SEM images of the 3DOM $Au_n/Ce_{1-x}Zr_xO_2$ catalysts prepared by GBMR method: (A) $Ce_{0.8}Zr_{0.2}O_2$, (B) $Au_{0.005}/Ce_{0.8}Zr_{0.2}O_2$, (C) $Au_{0.01}/Ce_{0.8}Zr_{0.2}O_2$, (D) $Au_{0.02}/Ce_{0.8}Zr_{0.2}O_2$, (E) $Au_{0.04}/Ce_{0.8}Zr_{0.2}O_2$, (F) $Au_{0.06}/Ce_{0.8}Zr_{0.2}O_2$. (Reprinted from ref. 129 with permission from Royal Society of Chemistry).

80% and silica removal rates are increased by 50%, facilitating precise and reliable mass-manufacturing of chips for nanoelectronics.[16] These results are very important for industry. Molecular dynamic (MD) simulation rationally elucidates the observed morphological variation *via* crystallization from melt at the atomistic level and corroborates the experimental observations that the doping of Ti ions changes the shape of CeO_2 nanocrystals from polyhedron to sphere (Fig. 25a). From these results, they predicted that spherical oxide nanocrystals can be synthesized generally by suppressing nucleating seed evolution at the surface thus forcing the nucleating seed to spontaneously evolve in the bulk.[16]

Following this work, Sayle *et al.* performed simulation with full atomistic models of pure and titanium-doped ceria nanorods and framework architectures.[130] The formation of amorphous nanoparticles firstly, then self-aggregation into nanorods and nanoporous architectures, and lastly the crystallization from the amorphous oxide precursors are simulated step by step. The simulation results predicted that Ti doping would "smooth" the surface: the CeO_2 hexagonal prisms shaped CeO_2 nanorods with {111} and {100} surfaces become cylindrical, and framework architectures change from facetted pores and channels with well-defined {111} and {100} surfaces to "smooth" pores and channels, as shown in Fig. 26a–d.[130]

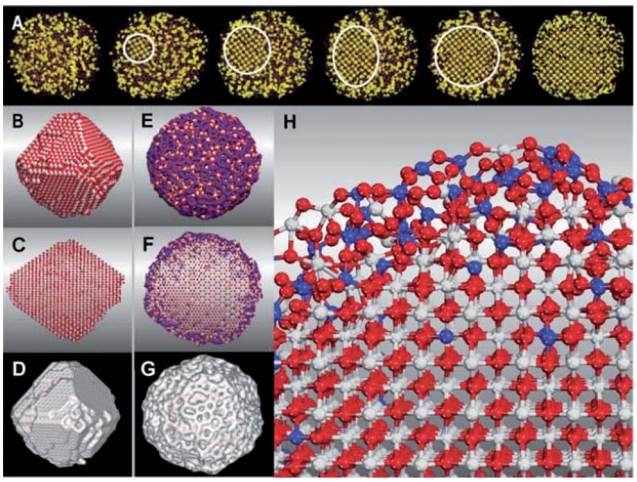

Fig. 25 (A) Images taken during a MD simulation for crystallization of Ti-doped CeO_2 nanoparticles, showing the initial amorphous precursor (left), evolution, and growth of the seed (circled) to the fully crystalline nanoparticle with amorphous shell (right); (B to D) Nondoped nanoparticle, (E to G) Ti-doped CeO_2 nanospheres, (H) enlarged segment of the Ti-doped nanosphere. (B and E) Sphere model representation of the atomic positions, (C and F) side view with smaller spheres to view through the nanoparticle, (D and G) surface rendered model. Cerium is colored in white; Ti(IV) is blue, and oxygen is red. The nanoparticles are about 7 to 8 nm in diameter. All images show actual atomic positions and are not schematics. (Reprinted from ref. 16 with permission from the American Association for the Advancement of Science.)

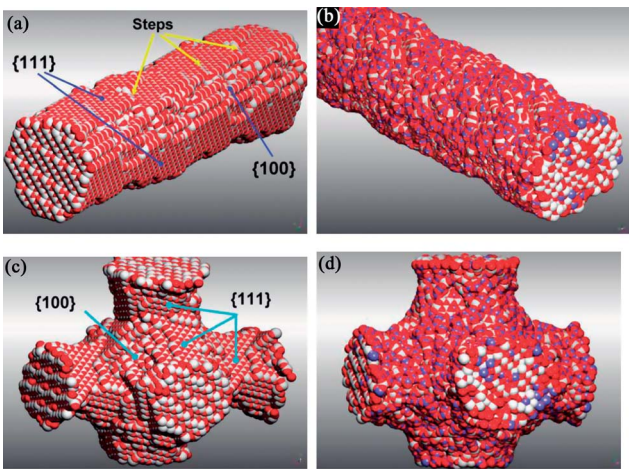

Fig. 26 The atomistic sphere models of (a) the undoped CeO_2 nanorod and (b) the Ti-doped CeO_2 nanorod, and atomistic sphere models of nanoporous framework architectures (c) CeO_2 and (d) Ti-CeO_2. Ce is colored in white; Ti, blue; and O, red. (Reprinted with permission from ref. 130. Copyright 2007 American Chemical Society).

4. Theory calculation

4.1. Fundamental properties of ceria

Recent progress in theoretical studies provides fundamental understanding of the properties of CeO_2. The calculation by Skorodumova *et al.*[131] on the basis of first-principles quantum mechanical simulations first explained the microscopic mechanism behind the extraordinary ability of ceria to store, release, and transport oxygen. They proposed that the reversible CeO_2–Ce_2O_3 reduction transition associated with oxygen-vacancy formation and migration is directly coupled with the quantum process of localization/delocalization of the 4f electron of cerium, as shown in Fig. 27. The vacancies are easily healed again in an O-rich ambience, which makes the oxide perfectly suited to balance the oxygen supply during a catalytic reaction.[131] Two electrons are left behind in the lattice that form two reduced Ce^{3+} species when an oxygen atom is removed. The electrons occupy split-off states of the initially empty Ce 4f band, lying inside the O_{2p}–Ce_{5d} bandgap of ceria and being highly localized in space.[131] The migration of oxygen in ceria and ceria-based materials takes place *via* a vacancy hopping mechanism.[132] Clusters of more than two vacancies, such as linear surface oxygen vacancies, proved to be favorable for migration of oxygen.[133,134] If the diffusion of anions is sufficiently fast, a continuous supply of oxygen from the bulk to the surface will guarantee an enhanced reducibility in ceria.

For better understanding of surface chemistry and catalysis on ceria, Ganduglia-Pirovano *et al.* theoretically studied the structure of near-surface oxygen vacancies and found subsurface vacancies with (2 × 2) periodicity to be energetically more favorable.[135] The electrons arising from the formation of surface and subsurface lattice oxygen vacancies at the CeO_2 (111) surface do not necessarily localize on the nearest neighbor (NN) Ce ions, but that relaxations may lead to a global minimum structure with the electrons localized on the next-nearest neighbors (NNN) instead.[135]

It should be mentioned that the electronic structure of materials that exhibit strong electron correlation, such as cerium oxide and many rare-earth oxides, is typically poorly described by the conventional density functional theory (DFT) approach.[136,137] DFT normally averages the exchange correlation of the electronic interaction and does not correct for the non-physical self-interaction of the electrons. Skorodumova *et al.*[138] and Andersson *et al.*[139] described the structural, thermodynamic, and electronic properties of cerium oxide and found that the on-site Coulomb interaction U has a significant influence on the calculated results. Shi *et al.*[140] theoretically investigated the

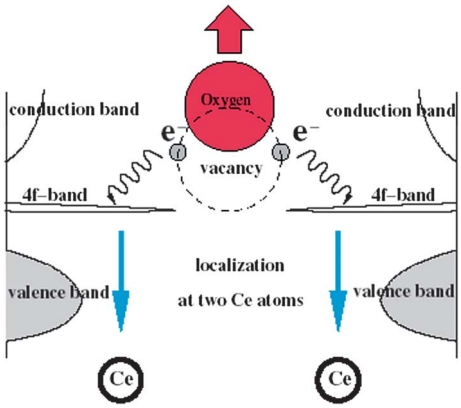

Fig. 27 The process of oxygen-vacancy formation in ceria. An oxygen atom moves away from its lattice position leaving behind two electrons, which localize on two cerium atoms, turning Ce (4+) into Ce (3+). (Reprinted from ref. 131 with permission from American Physical Society.)

effects of M (M = Mn, Pr, Sn, Zr) doping on the redox thermodynamics of CeO_2 using first-principles density-functional theory calculations by taking the on-site Coulomb interaction into account. Two different mechanisms for the O-vacancy formation in doped CeO_2 have been proposed. Compared with the case of pure CeO_2, the decrease of the O-vacancy formation energy for Zr-doped CeO_2 is mostly caused by the structural distortion, whereas the decrease for Mn-, Pr-, or Sn-doping originates from the electronic modification as well as from the structural distortion.[140] It was found that the electronic modification occurs in those dopants whose uttermost atomic orbitals are half or fully occupied by the filling of the excess electrons left by the formation of the O vacancy.[140] Two effects contribute to the concentration dependence of the O-vacancy formation energies for different dopant species.

Solid electrolytes play an important role in several technological applications, such as fuel cells. Optimization of such materials is often done by trial and error.[31] Andersson *et al.*[141] present a clear physical picture of the connection between the choice of a dopant and the improvement of ionic conductivity in ceria using a quantum-mechanical first-principles calculation. Their results reveal a remarkable correspondence between vacancy properties at the atomic level and the macroscopic ionic conductivity. The key parameters comprise migration barriers for bulk diffusion and vacancy–dopant interactions, represented by association (binding) energies of vacancy–dopant clusters.[141] In the optimal electrolyte, the repulsive elastic and attractive electronic interactions should balance. They concluded that the ideal dopant should have an effective atomic number between 61 (Pm) and 62 (Sm).[141]

The catalytic activity of CeO_2 is closely related to the energy of oxygen vacancy formation on ceria surfaces. Using a force-field method, Sayle *et al.* showed that oxygen vacancies were found to be more stable on (111), (110) and (310) surfaces than that in the bulk of crystal[142] and formation of anion vacancy seemed to be more difficult on CeO_2 (111) than on (110) and (100).[143] Yang *et al.*[144] studied the formation of oxygen vacancies on ceria surfaces using a first-principles method and found that the formation of an oxygen vacancy was closely related to the surface structure and occurs more easily for the (110) surface than (111). The preferred vacancy location is in the surface layer for CeO_2 (110) and in the subsurface layer (the second O-atomic layer) for CeO_2 (111). For both surfaces, the O vacancy forms more readily than in the bulk.[144] Yang's results are consistent with the results of Ganduglia-Pirovano *et al.*[135] and Nolan *et al.*[145] Liu *et al.* reported that Au atoms prefer to sit on the O-vacancy site on CeO_2 (111) compared to the stoichiometric surface, which can be explained in terms of an enhanced ionic bonding since each O-vacancy is associated with two extra electrons left by the removal of an O atom.[146]

Furthermore, computational studies of ceria nanoparticles ranging from 50 to more than 200 atoms (*i.e.*, including aggregates large enough to be in the "scalable-to-bulk" regime) have been performed recently.[147–149] These models allow one to realistically describe the reactivity of various sites of both ceria nanoparticles and catalysts formed after deposition of noble metal cluster on them. It has shown that the highest occupied molecular orbital (HOMO)–lowest unoccupied molecular orbital (LUMO) gap in nanometer-sized ceria particles is notably reduced with respect to the regular CeO_2 (111) surface, with the HOMO mainly composed of O 2p orbitals and the LUMO of Ce 4f orbitals.[68] The oxygen-vacancy formation energy in ceria nanostructures decreases with respect to the extended surface.

4.2. The interactions between the metal and ceria support

The nature of the support had a decisive role in the activity of catalysts, for example, alumina- and magnesia-supported gold were found to be significantly more active than silica-supported gold.[150] A synergetic effect usually exists between the metal oxide support and the catalysts.[151] The metal oxide does not only simply act as an inert support, but also intervenes in the catalytic process. Noble metal/ceria-based catalysts are among the systems long known to exhibit strong metal–support interaction (SMSI) effects.[152] Therefore, understanding of metal–ceria support interactions in supported metal catalysts is very important for developing nanostructured CeO_2-based catalysts with desired performances.

For the origin of the interactions between the active (metal) phase and support, various support effects have been proposed and well summarized by Vayssilov *et al.*,[153] including electronic interactions between both components,[154] stabilization or destabilization of certain particle shapes or sizes,[155,156] surface transport of adsorbates through the boundary (spillover, reverse spillover, capture zone effects);[157,158] and so-called 'strong metal–support interactions' involving migration of partially reduced oxides onto the active phase[159,160] or the stabilization/destabilization of oxidized active phases by the support.[161]

CeO_2 has been recognized as the best supporting material for catalysis at Au NPs due to its high oxygen storage and release capacity, facile oxygen vacancy formation, and the presence of a narrow Ce f-band.[162] Experimental studies have shown that the surface of CeO_2 can easily be enriched with oxygen vacancies[163,164] and that Au NPs bind strongly to these vacancies.[165,166] Lawrence *et al.* recently demonstrated that catalytic activity is a function of the concentration of oxygen vacancies for the CO oxidation activity of CeO_2 nanorods, NPs, and the bulk surface.[164] Oxygen vacancy formation on the CeO_2 surface accompanies the reduction of adjacent Ce^{4+} to Ce^{3+} ions, and the concentration of Ce^{3+} ions is proportional to that of oxygen vacancies.[164] The formation of the surface chemisorbed oxygen species can be facilitated by defects in the catalyst structure.[167] Localized electrons on the occupied 4f-orbital of Ce^{3+} ions contribute to the electronic interaction between reduced CeO_2 and supported Au NPs.[162,168] Au tends to be oxidized once it is in contact with CeO_2. $Au^{\delta+}$ ions can adsorb CO sufficiently strongly for subsequent catalysis.[115,146] The highly catalytic activity is not limited to ultrasmall monolayer Au clusters,[169] which was suggested previously by Liu *et al.*[146]

Kim *et al.*[170] recently studied the catalytic activity of CeO_2-supported Au nanoparticles toward CO oxidation using density functional theory. They proposed three CO oxidation mechanisms by Au_{13}@CeO_2: CO oxidation by co-adsorbed O_2, CO oxidation by lattice oxygen in CeO_2, and CO oxidation by O_2 bound to a Au–Ce^{3+} anchoring site.[170] Oxygen vacancies are shown to open a new CO oxidation pathway by O_2 bound to a Au–Ce^{3+} anchoring site. Their results provide a design strategy for CO oxidation on supported Au catalysts. Lowering the vacancy formation energy of the supporting oxide with easily

reducible oxides can increase the concentration of reduced metal ions which act as anchoring sites for O_2 molecules, similar to the results by Nilekar *et al.*[171] In transition metal core–Pt shell NPs, modifying Au NPs with alloying elements would be a promising strategy for lowering CO adsorption energy, as well as decreasing and increasing saturated CO and O_2 concentration, respectively.

Pt–ceria is another important catalyst for CO oxidation,[172] water gas shift reaction[172–174] and other catalytic reactions.[175] The interaction of a representative metal cluster Pt_8 with two group of model ceria nanoparticles exhibiting crystalline-like atomic arrangement was studied computationally by Vayssilov *et al.*[176] It was found that the presence of platinum on the ceria nanoparticles induced electron transfer from the metal to the support leading to the formation of a small fraction of Ce^{3+} cations. The amount of the reduced cerium cations depends on the size of the ceria nanoparticle and the stability of the Ce 4f levels.[176] The electronic levels of platinum fill the gap between the O 2p and Ce 4f levels of ceria, thus mediating the electron exchange between the Pt cluster and ceria nanoparticle, and leading to the reduction of a nonstoichiometric amount of Ce^{4+} to Ce^{3+} cations upon the removal or spillover of O.

Recently, Vayssilov *et al.* also found that oxygen transfer from the CeO_2 support to Pt NPs, termed oxygen spillover, occurs due to the low vacancy formation energy of nanostructured CeO_2.[153] A Pt_8 cluster supported on a stoichiometric $Ce_{40}O_{80}$ nanoparticle was chosen as a model. In the most stable structure found for $Pt_8/Ce_{40}O_{80}$ (Fig. 28a), the metal cluster interacts through five Pt atoms with the ceria particle and reveals a binding energy of −6.49 eV with respect to the bare $Ce_{40}O_{80}$ and Pt_8 species. The presence of Pt_8 on the ceria nanoparticle has only a moderate influence on both the O 2p and Ce 4f levels (Fig. 28b), however, the platinum states essentially fill the whole bandgap and contribute to the HOMO–LUMO region.[153] Both the HOMO and the LUMO belong to the platinum cluster, but the Ce 4f levels are close in energy to the LUMO. Two types of oxidative metal–oxide interaction on well-defined models have been identified, electron transfer from the Pt nanoparticle to the support, and oxygen transfer from ceria to Pt.[153] The electron transfer is favorable on ceria supports and the oxygen transfer is shown to require the presence of nanostructured ceria in close contact with Pt, which is inherently a nano-size effect. Their findings confirm that the size of the CeO_2 support has a critical role in catalytic activity of supported NPs, consistent with the finding by Carrettin *et al.*[66] It enables clarification of the formation mechanism of the catalytically indispensable Pt–O species on ceria and to elucidate the extraordinary structure–activity dependence of ceria-based catalysts in general.[153]

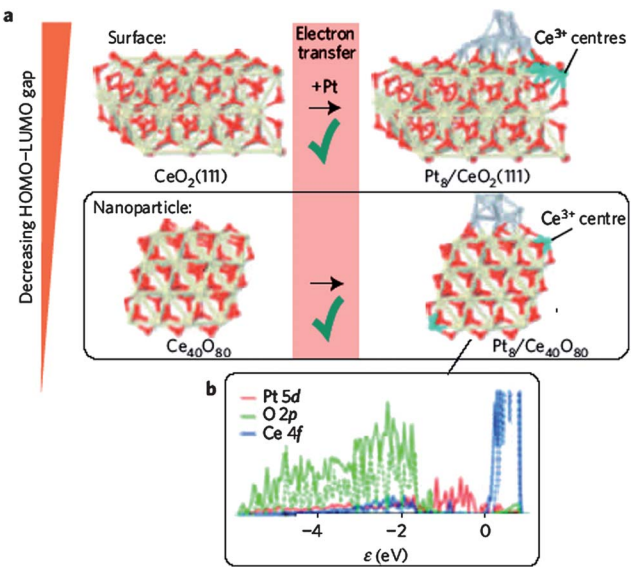

Fig. 28 Metal–oxide interaction in Pt–CeO_2: electron transfer. (a) Electronic interaction between Pt clusters and extended planar or nanostructured CeO_2 supports: for Pt_8 clusters on both a CeO_2 (111) slab and a stoichiometric $Ce_{40}O_{80}$ nanoparticle calculations predict spontaneous electron transfer from platinum to the ceria support. (b) Density-of-states plot for the bare nanoparticle $Ce_{40}O_{80}$ (dashed lines) and the nanoparticle system $Pt_8/Ce_{40}O_{80}$ (solid lines). The energies are with respect to the Fermi level of $Pt_8/Ce_{40}O_{80}$ and two density-of-states plots are aligned using the difference in the average VASP electrostatic potentials in vacuum. (Reprinted from ref. 153 with permission from Nature Publishing Group.)

For Ag–CeO_2 catalysts, Liu and colleagues[177] predicted oxygen adsorption, dissociation, and transport processes on the two most stable Ag (111) and Ag (110) surfaces and on a monolayer silver supported by CeO_2 (111) surfaces with or without oxygen vacancies using first-principles calculations based on spin polarized DFT with PAW method. The computed energies of these reactions show that the O_2 reduction process and the incorporation of the dissociated O ions in the oxide electrolyte prefer taking place in the TPB region with oxygen vacancies.[177] This result is useful for understanding the oxygen reduction reactions occurring in the cathode of SOFCs.

5. Characterization

X-ray photoelectron spectroscopy (XPS) and X-ray absorption near edge spectroscopy (XANES) have been used to investigate the oxidation state of cerium ions in ceria nanoparticles.[178] Recently, Eichhorn *et al.* performed *in situ* spectroscopy to probe oxidation states of all exposed surfaces in operational solid oxide electrochemical cells (SOCs) at 750 °C in mbar reactant gases H_2 and H_2O, combining ambient-pressure XPS and CeO_{2-x}/YSZ/Pt single-chamber cells.[179] The mixed ionic/electronic conducting CeO_{2-x} electrodes undergo Ce^{3+}/Ce^{4+} oxidation–reduction changes with applied bias. The simultaneous measurements of local surface Ce oxidation states and electric potentials reveal the active ceria regions during H_2 electro-oxidation and H_2O electrolysis. They also found that the active regions extend about 150 μm from the current collectors and are not limited by the three-phase-boundary interfaces associated with other SOC materials.[179] The observation of the existence of the Ce^{3+}/Ce^{4+} shifts in the about 150 μm active region leads to the conclusion that the surface reaction kinetics and lateral electron transport on the thin ceria electrodes are co-limiting processes.

The recent advancement in experimental approaches, *e.g.* high-resolution scanning tunneling microscopy (STM), dynamic force microscopy (DFM), and spherical aberration-corrected transmission electron microscopy, has contributed significantly to the characterization of ceria-based heterogeneous catalysts with a true atomic-scale resolution. The enormous success of the STM is owing to its unique and unparalleled high spatial and

temporal resolution enabling imaging of single atoms and molecules on surfaces and their motion in real time.[180] Esch *et al.* investigated the CeO_2 surfaces by combining STM and density functional theory.[163] They showed that surface oxygen vacancies on CeO_2 (111) were immobile at room temperature, but linear clusters of these vacancies form at higher temperatures. These vacancy clusters expose exclusively Ce^{3+} ions to gas-phase reactants. Thus, the exposed Ce^{3+} ions are grouped into large ensembles, whereas the sites immediately adjacent to these vacancy clusters remain as pure Ce^{4+} ions (Fig. 29).[43] One subsurface oxygen vacancy is required to nucleate each vacancy cluster.

As stated above, Esch's results on the reduced CeO_2 (111) surface have revealed that one subsurface oxygen vacancy is required to nucleate linear surface oxygen vacancy clusters.[163] Thus, these subsurface vacancies seem to play a critical role in the catalytic properties of ceria by enabling a further surface oxygen release and stabilizing the formation of linear oxygen vacancy clusters, which are the dominant defect structures on the strongly reduced surface.[163,181,182] Using an atomic resolution dynamic force microscopy, Torbrügge *et al.*[183] have clearly identified surface and subsurface oxygen vacancies on the slightly reduced CeO_2 (111) surface at 80 K, as shown in Fig. 30. Their result substantiates the topography predicated by the first-principles calculations.[137] By combining two simultaneously acquired signals (the topography and the energy dissipated from the cantilever oscillation), they clearly locate subsurface oxygen vacancies buried at the third surface atomic layer.[183] Their results conclude the existence of interactions between subsurface oxygen vacancy structures that make them to order in open linear arrays upon the presence of a high density of these defects.[183]

Recently, STM imaging and spectroscopy in combination with DFT calculations have also been used to reveal electron localization in defective ceria surfaces by Jerratsch *et al.*[184] The spatial correlation between an oxygen vacancy and the associated Ce^{3+} ion pair in a defective CeO_2 (111) film has been identified. The two Ce^{3+} ions can occupy different cationic shells around the vacancy. The resulting variation in the chemical environment leads to a splitting of the filled Ce^{3+} f levels that is detected with STM spectroscopy. Although the precise position of the two Ce^{3+} ions is not revealed, it was found that they always sit in different coordination spheres around the defect, in agreement with earlier

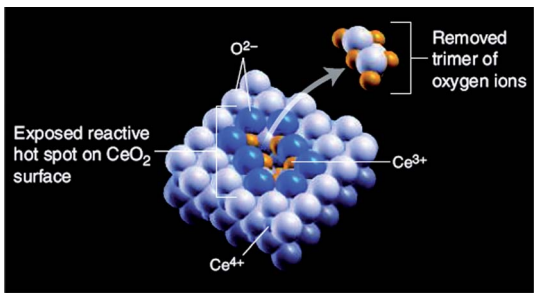

Fig. 29 Reactive defect in a ceria surface. Coordinated Ce^{4+} ions in a diametric surface vacancy cluster are reduced to reactive Ce^{3+} when the trimer of oxygen ions (surface dimmer plus a subsurface oxygen) is removed. (Reprinted from ref. 43 with permission from The American Association for the Advancement of Science.)

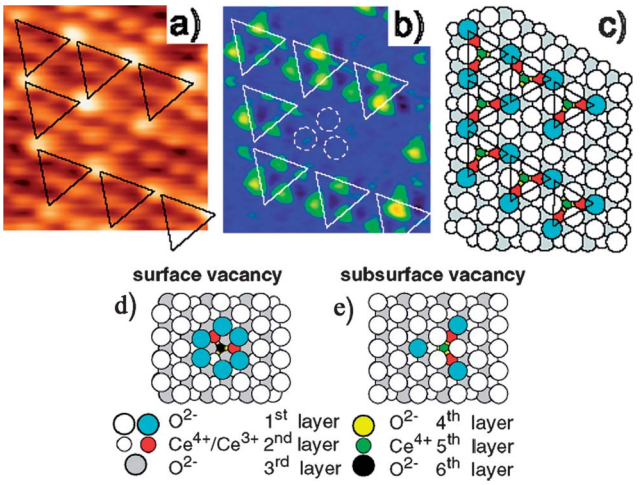

Fig. 30 Topography (a) and dissipation (b) images together with the corresponding schematic model (c) of the typical local ordering of subsurface oxygen vacancies observed. The subsurface oxygen vacancy structures are highlighted by triangles. The dashed circles indicate a defect free surface area. The color coding of the model depicted in (c) is the same as that in structural models for surface vacancy (d) and subsurface vacancy (e). The image set point was $-2.9\text{fN}\sqrt{\text{m}}$. (Reprinted from ref. 183 with permission from American Physical Society.)

theoretical results.[135] The driving force for adopting such open configurations is the better ability of the system to relax lattice strain induced by the more spacious Ce^{3+} ion compared to the Ce^{4+} counterpart.[184]

Electron microscopy and its associated techniques (*e.g.*, electron energy loss spectroscopy (EELS) analysis) have contributed significantly to the characterization of heterogeneous catalysts and can provide micro-scale information on the structure, morphology, composition, and electronic state of the area of interest. With the advent of spherical aberration correction in the electron microscope to achieve an image resolution below 0.1 nm and the rapid development of *in situ* techniques, advanced electron microscopy has been employed to probe fundamental questions of heterogeneous catalysis and catalysts.[185] Understanding the nature of metal–support interactions by means of advanced electron microscopy becomes critical for designing and fabricating nanoarchitectured catalysts with desired performances.[186]

Kirkland *et al.*[187] showed that spherical aberration-corrected transmission electron microscopy (TEM) can be used to determine the surface termination of oxide nanoparticles. They have used a combination of direct aberration corrected TEM and computational exit wavefunction restoration to examine the structure of specific surfaces of catalytic CeO_2 nanoparticles during a reversible beam induced redox reaction at ambient temperature. Fig. 31a shows the phase of the specimen exit surface wavefunction of a representative ceria nanoparticle viewed close to a ⟨110⟩ direction, restored from a focal series of aberration-corrected images. The nanoparticle surface present in the restored exit wave phase parallel to the electron beam was characterized by extracting average line profiles (Fig. 31b) and matching these to equivalent profiles extracted from the simulated data. It is noted that this comparison with the simulated

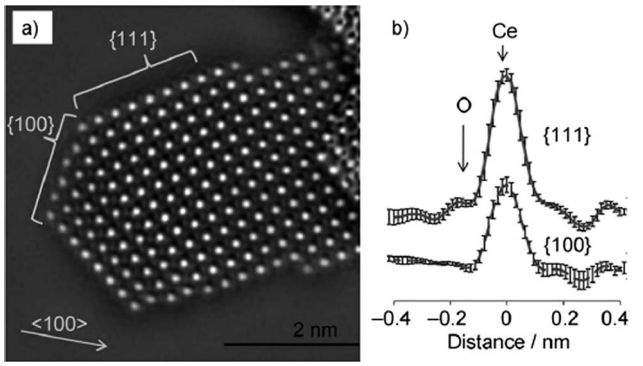

Fig. 31 (a) Exit wave phase of a CeO_2 nanoparticle imaged close to a ⟨110⟩ direction. (b) Average of seven line profiles obtained from {111} and {100} surfaces along a ⟨110⟩ direction, as indicated in (a), with the vacuum region on the left and the particle bulk on the right. Profiles were aligned by centering the peak corresponding to the outermost cerium atomic column at zero and calculating the mean value of the experimentally measured phase shift. Error bars show the standard deviation in this measurement for equivalent surface sites as a function of pixel position. The averaged profile for a {111} surface has a peak at the surface corresponding to oxygen. This peak is absent in the profile extracted for the {100} surface. (Reprinted from ref. 187 with permission from John Wiley and Sons, Inc.)

data is simplified compared to that using single images since reconstruction of the exit wavefunction computationally compensated the residual aberrations of the microscope leaving the projected structure and specimen thickness as the only unknown parameters.[187]

Fig. 32a shows the restored exit wave phase for a particle that was imaged for several hours.[187] The ordering of oxygen vacancies occurs at ambient temperature under prolonged irradiation and in the high-vacuum conditions of the TEM has been observed, as demonstrated by the presence of superlattice reflections along a ⟨220⟩ direction in the Fourier transform modulus shown in Fig. 32b. The {111} surface remains predominately oxygen-terminated even in the highly reduced ordered state (Fig. 32c). Their results support the conclusion that

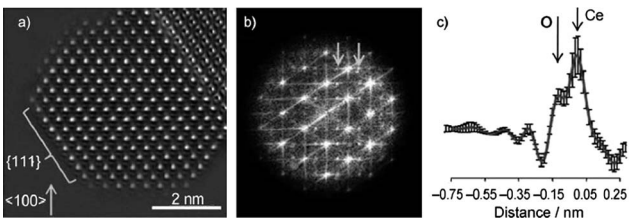

Fig. 32 (a) Phase of the exit wavefunction for a CeO_2 nanoparticle imaged close to a ⟨110⟩ direction after extensive beam-induced reduction to an ordered sub-oxide. (b) Modulus of the Fourier transform calculated from (a) with arrows indicating the presence of superlattice spots along the ⟨220⟩ directions characteristic of oxygen vacancy ordering. (c) Average projected line profile with the vacuum on the left-hand side extracted along a ⟨100⟩ direction through a {111} surface, as indicated at the bottom left of the restored exit wave phase in (a). The arrow in (c) shows a shoulder on the larger cerium peak which is consistent with the {111} surface remaining oxygen-terminated. (Reprinted from ref. 187 with permission from John Wiley and Sons, Inc.)

the extended {111} surface in CeO_2 nanoparticles are stabilized by oxygen termination and that this surface structure is maintained even after the nanoparticle has been substantially reduced under electron irradiation. This result is in agreement with theoretical models[130] and also with atomic force microscopy measurements of bulk {111} ceria surface.[184] In contrast, the {100} surfaces are metal-terminated but are unstable, which is again in agreement with the theoretical calculations.

In situ phase contrast high-resolution transmission electron microscopy with spherical aberration correction has been shown to be the ideal tool to analyze cationic reconstruction.[188] Hydrothermally prepared ceria nanoparticles with particularly enhanced {100} surface exposures are explored. Experimental analysis of cationic reconstruction is supported by molecular dynamics simulations where the Madelung energy, a major constituent of the cohesive energy of ionic crystals, is shown to be directly related to the binding energy, which enables one to generate a visual representation of the distribution of "reactive" surface oxygen. A faceted ceria nanoparticle was selected and imaged so that an extended {100} surface adjoining a smaller {111} surface can be clearly observed (Fig. 33a). To clarify the geometry and crystallography, a molecular dynamics simulated system showed the same joining interfaces (Fig. 33b). Dynamic changes under the e-beam were observed by taking a series of 30 images at an interval of 2 s each (Fig. 33c). It was found that the changes were arising from atomic motion and reconstruction of the terminating monolayer in the extended surfaces of both

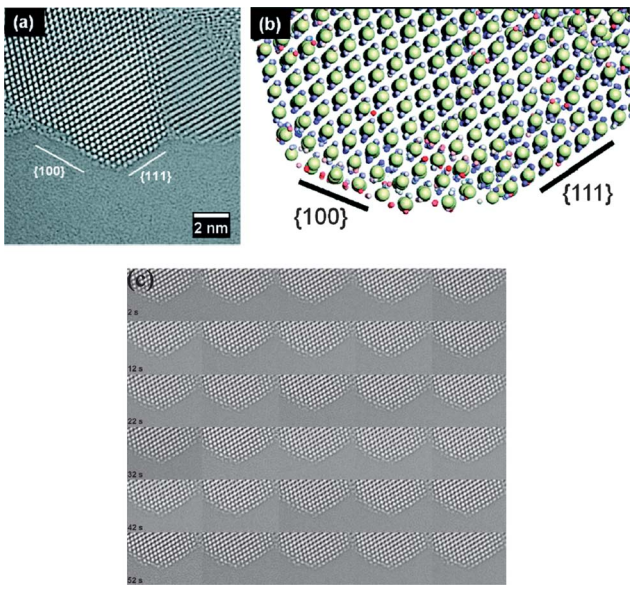

Fig. 33 (a) Faceted ceria nanoparticle imaged along the [110] zone axis using 300 kV JEM-3100 R005 aberration-corrected TEM showing {111} and {100} facets. The image, taken at slight underfocus, has been black-white inverted for better visibility of atomic columns. (b) Atomic model revealing {100} and {111} surfaces to compare with experiment. Cerium positions are represented by large spheres, and oxygen positions represented by small spheres colored according to Madelung energy (red = low, blue = high). (c) Time series of atomic hopping processes on a ceria nanoparticle, recorded at a time interval of 2 s (imaging conditions as with a). (Reprinted with permission from ref. 188. Copyright 2012 American Chemical Society).

{100} and {111} type. Therefore, the electron beam and its induced atom migration were proposed as a readily available probe to emulate and quantify functional surface activity, which is crucial for catalytic performance.[188]

The atomic and electronic structures of a (210)$\sum$5 grain boundary selected as a model grain boundary in CeO_2 thin film was investigated by Hojo *et al.* with STEM, EELS, and theoretical calculations.[189] Cerium and oxygen sublattices have been determined directly and the evidence of oxygen nonstoichiometry at the grain boundary has been obtained (Fig. 34). In the high-angle annular dark-field (HAADF) image (Fig. 34a), the bright spots correspond to the Ce column locations, while the O columns surrounded by four Ce columns are not evident because the atomic number Z for oxygen is too small. An annular dark field image formed only by very high angle, incoherently scattered electrons, as opposed to Bragg scattered electrons, is highly sensitive to variations in the atomic number of atoms in the sample (Z-contrast images). Oxygen columns can be directly identified in the annular bright-field (ABF) image, in which the columns appear with dark contrast, as indicated by the arrows in panels in Fig. 34b and d. The atomic columns of Ce were observed even in the grain boundary core region and the grain boundary was made of repeating structural units marked by quadrilaterals in Fig. 34a and b. The presence of oxygen vacancies at the grain boundaries was also confirmed by EELS measurements (Fig. 35). The weak peak intensity at the grain boundary region indicates the low density of Ce atoms at the grain boundary region.[189] The EELS spectrum from the grain boundary region is slightly broader than that from the grain interior region, indicating the presence of Ce^{3+} as well.[189] The M_5/M_4 intensity ratios were calculated to be 0.9, whereas that at the grain boundary tends to be larger, going toward the Ce^{3+} side (Fig. 35b). Their results revealed that oxygen nonstoichiometry plays a crucial role in the stable grain boundary structure of CeO_2. The importance of considering nonstoichiometry in constructing grain boundary structural models was demonstrated, especially for systems where a high degree of nonstoichiometry is expected, which provides a way for comprehensive understanding of grain boundaries through atomic scale determination of atom and defect locations.[189]

Barnard and Kirkland[191] demonstrated combining advanced high resolution transmission electron microscopy characterization of the shape of ceria nanocrystals with a shape-dependent thermodynamic model is possible to determine the detailed surface chemistry of ceria at the nanoscale.

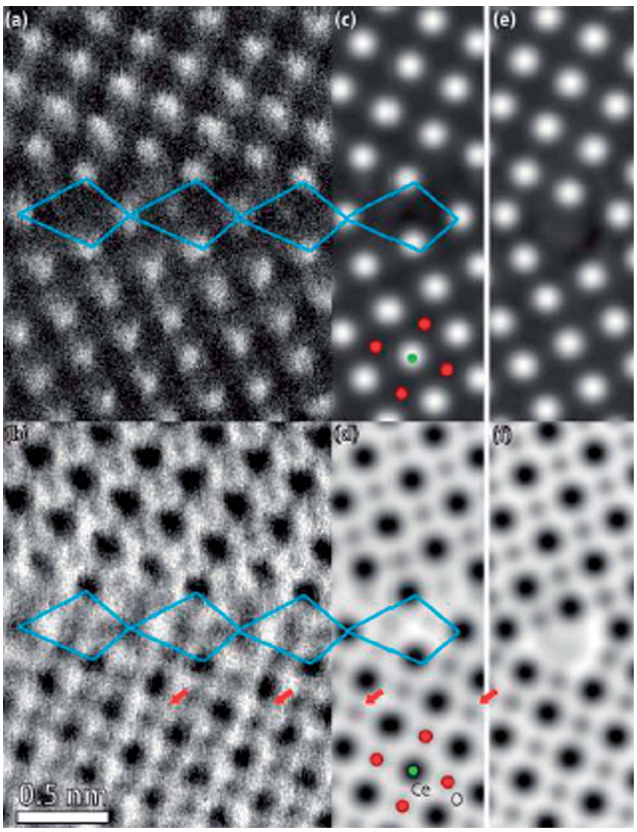

Fig. 34 (a) The HAADF and ABF images of a [001] (210)$\sum$5 grain boundary in a CeO_2 thin film. (c) Simulated HAADF and (d) ABF images of the nonstoichiometric grain boundary model structure. (e) Simulated HAADF and (f) ABF images of the stoichiometric grain boundary model structure. The structural units of each boundary are indicated by polygons. The contrast in (c) and (e) has been aligned a little to fit to the experimental image. A noise-reduction procedure was applied to the ABF image by a background subtraction filter. (Reprinted with permission from ref. 189. Copyright 2010 American Chemical Society).

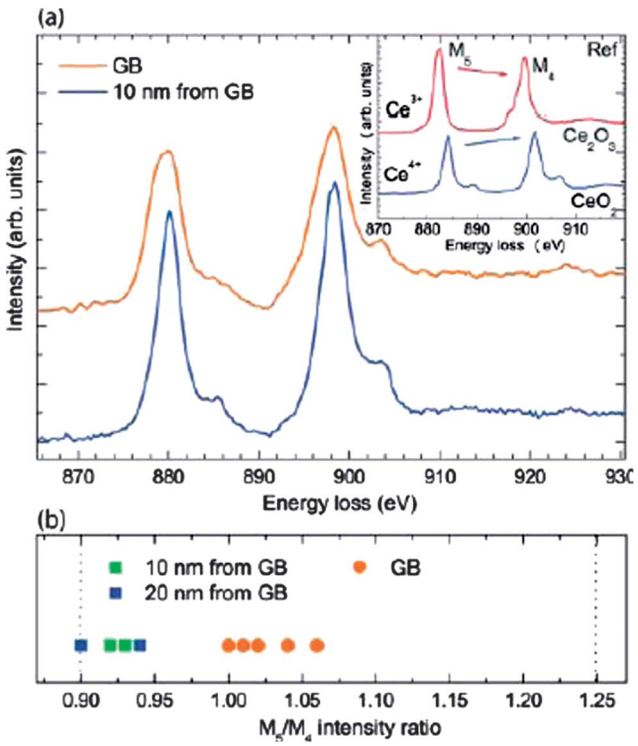

Fig. 35 (a) Typical Ce $M_{4,5}$-edge EELS spectra taken from the grain boundary region and from the grain interior region. The inset shows reference spectra from ref. 190 obtained for CeO_2 and Ce_2O_3, corresponding to valence states of Ce^{4+} and Ce^{3+}, respectively. (b) Variation of the M_5/M_4 intensity ratio calculated by the positive part of second derivative of the experimental spectra at several grain boundary regions and grain interior regions. (Reprinted with permission from ref. 189. Copyright 2010 American Chemical Society).

6. Applications

As discussed above, ceria is a technologically important functional material for many applications. In the following sections, a few typical application examples regarding nanostructured ceria will be selectively reviewed.

6.1. CO oxidation

Nanostructured CeO_2 materials loaded with noble metals are promising catalysts for the elimination of toxic auto-exhaust gases,[4,5] low-temperature water-gas shift (WGS) reaction,[6,7] and the preferential oxidation of traces of CO in a large hydrogen excess (PROX).[192] In the case of Au-supported catalysts, factors such as Au particle size, preparation method, pretreatment conditions, and choice of the support may have an impact on activities of the final catalysts.[66,150] In particular, the support material could have a significant effect on the performance of the catalysts.

Carbonaceous soot can be oxidized below 300 °C by a catalyst containing silver and ceria, however, the oxidation rate is inadequate and deterioration arising from sintering of silver usually occurs. Kayama *et al.*[193] recently fabricated a CeO_2–Ag nanomaterial with a rice-ball configuration that is different from encapsulated materials with a core–shell configuration in which nanosized metal particles are surrounded by polymerized oxide.[194] This unique characteristic makes it suitable for application as a catalyst. Fig. 36b shows that CeO_2–Ag oxidizes soot much more efficiently below 300 °C than CeO_2 and Ag–CeO_2 (a conventional supported catalyst consisting of equimolar silver and ceria), which oxidize soot mainly above 300 °C. These results show that catalysts containing silver and ceria lower the temperature of soot oxidation, although oxidation by the catalyst without the rice-ball nanostructure is inefficient at low temperatures below 300 °C.[193] Thus, the rice-ball nanostructure is an innovative catalyst configuration.

Haruta suggested that the catalytic activity of gold nanoparticles for CO oxidation depends strongly on the gold nanoparticle-support contact area.[195] Our group reported for the first time that flowerlike CeO_2 microspheres were used as catalyst supports for the CO oxidation reaction.[115] From the typical SEM and TEM images (Fig. 37a and b), it can be seen clearly that the gold nanoparticles were highly dispersed and distributed evenly onto the surface of CeO_2 nanosheets. The average size of Au nanoparticles is about 2–30 nm. By loaded with Au on flowerlike CeO_2 microspheres, the redox properties and the catalytic

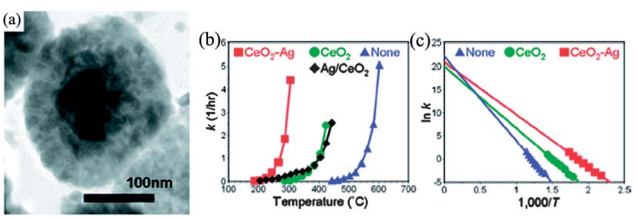

Fig. 36 (a) TEM image of the rice-ball nanostructured CeO_2–Ag; (b and c) Properties compared with conventional catalysts and the absence of a catalyst: (b) Evaluations of carbonaceous soot oxidation; (c) Arrhenius plots. (Reprinted with permission from ref. 193. Copyright 2010 American Chemical Society).

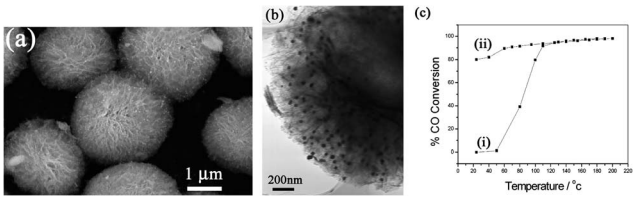

Fig. 37 (a) Typical SEM and (b) TEM images of the Au-loaded CeO_2 microspheres; (c) catalytic activity of CO oxidation over Au supported on CeO_2 catalysts: (i) bulk mesoporous CeO_2 powder loaded with Au (2.82 wt%), (b) flowerlike CeO_2 microsphere loaded with Au (2.77 wt%). (Reprinted from ref. 115 with permission from Elsevier Ltd.)

activities toward CO oxidation have been improved. The loading of Au onto CeO_2 support completely modifies its temperature-programmed reduction (TPR) profile. The Au loaded CeO_2 microsphere exhibits an excellent low-temperature catalytic activity toward CO oxidation. The CO gas over the Au-loaded CeO_2 microsphere starts rapidly its conversion into CO_2 at room temperature, reaching above 80% (Fig. 37c). The enhanced performance was attributed to its open three-dimensional porous structure, large pore volume and higher oxygen vacancy level in CeO_2 microspheres. An excellent catalytic activity toward CO oxidation was also observed in the catalyst of flowerlike CeO_2 microspheres loaded with 15wt.% CuO.[115]

The physical and chemical properties of ceria can be tuned by doping. Low-temperature reducibility is enhanced by doping with reducible elements, such as Pr and Sn.[196–198] Xiao *et al.*[114] prepared Y, La, Zr, Pr, and Sn doped ceria with a flowerlike structure and studied their catalytic activity toward CO oxidation. As shown in Fig. 38, Pr- or Sn-doped flowerlike ceria catalysts exhibit excellent catalytic activities, which was ascribed to the variable valence states of Pr and Sn.[196,198] In contrast, the doping of Y, La or Zr in CeO_2 exhibit adverse effects on the activity of CO oxidation. This may result from the fact that the doping cations with stable valence state partially suppress the conversion of the redox Ce^{4+}/Ce^{3+} couple and decrease the dynamic oxygen storage capacity (OSC) in ceria.

Designing and synthesizing a highly reactive/selective catalyst with well-defined crystal planes has been a challenging goal in heterogeneous catalysis.[199–206] Li and coworkers reported that single-crystalline CeO_2 nanorods are more active for CO

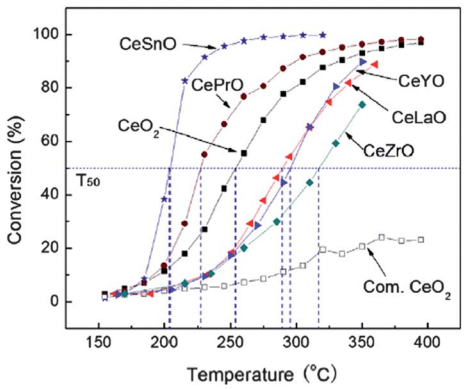

Fig. 38 Conversion profile of carbon monoxide *versus* temperature. (Reprinted from ref. 114 with permission from Elsevier Ltd.)

oxidation than irregular nanoparticles (Fig. 39).[98] The higher CO oxidation activity was ascribed to the more reactive crystal planes {001} and {110} in nanorods. This result indicates that better-performing catalysts with high reactive sites can be rationally designed. The shape-dependent OSC of ceria nanocrystals with various shapes (nanopolyhedra, {111} and {100}); nanorods, {110} and {100}, and nanocubes, {100}) have been reported by Yan *et al.*[97]

Recently, a direct relationship between the concentration of oxygen vacancy clusters with a larger size and the reactivity of nanosized ceria were also revealed by Li's group.[203] They prepared two ceria nanorod samples with different oxygen vacancies using different cerium salts during solvothermal synthesis. HRTEM analysis (Fig. 40) indicate that the A sample predominately exposes the {100} and {111} planes, whereas the {100} and {110} planes are predominately exposed in the B sample. It was also found that there were many "dark pits" on the A sample while fewer were on the B sample. In contrast to the previous theoretic study that {111} is the least active surface followed by {100} and {110} planes,[204] their results showed that A sample was more active than B sample for CO oxidation. By positron annihilation spectrum (PAS), a non-destructive spectroscopy technique to study voids and defects in solids, and temperature-programmed CO reduction (TPR) analysis, they found that there were higher concentrations of oxygen vacancy clusters with larger size in the A sample while some isolated vacancy associates predominated in the B sample. Therefore, the enhanced reactivity of the ceria-A sample was attributed to the larger vacancy clusters coupled with the adjacent Ce^{3+} ions, which provide effective adsorption sites for CO molecular.[203]

Another impressive example of a strong crystal plane-dependent catalytic activity of Au–CeO_2 catalysts for the WGS reaction has also been demonstrated by Flytzani-Stephanopoulos's group.[205] They prepared Au–CeO_2 catalysts by two-step process of hydrothermal synthesis of ceria nanocrystals followed by deposition/precipitation of gold. Different surfaces of CeO_2 nanoshapes were found to bind gold differently.[206] The {110} surfaces of CeO_2 nanorods bind and fully disperse gold (<1 nm), while gold particles (~3 nm) were almost exclusively formed on the {100} surfaces of the CeO_2 nanocubes. The rod-shaped ceria enclosed by {110} and {100} planes is most active for gold stabilization/activation.

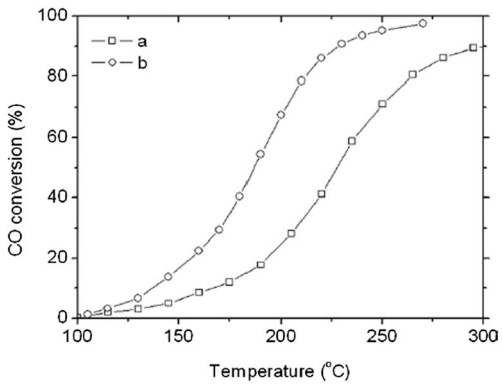

Fig. 39 Percentage conversion *versus* temperature plots for the oxidation CO over (a) CeO_2 nanoparticles and (b) CeO_2 nanorods. (Reprinted from ref. 98 with permission from Elsevier Ltd.)

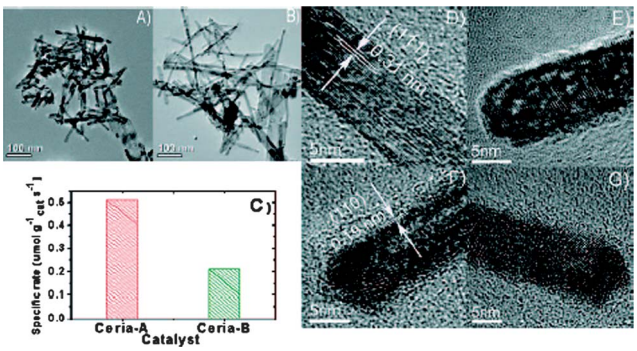

Fig. 40 (A) TEM images of ceria-A sample, (B) TEM images of ceria-B sample, (C) graph showing the specific rate for CO oxidation on ceria. *Reaction conditions*: the molar ratio for CO/air/N_2 was 1 : 16 : 83, with a contact time (W F^{-1}) of 75 g_{cat} h mol_{CO}^{-1}; reaction temperature 160 °C, (D and E) HRTEM images of ceria-A sample, (F and G) HRTEM images of ceria-B sample. (Reprinted with permission from ref. 203. Copyright 2009 American Chemical Society).

6.2. Steam reforming of alcohol for producing hydrogen

The use of biomass-derived alcohol for the production of hydrogen has significant interest for clean energy supply and environmental protection.[207,208] The flowerlike CeO_2 microspheres as mentioned above were used also in a reforming catalyst for steam reforming of ethanol producing H_2. Catalytic activity is evaluated in terms of ethanol conversion and the selectivity of products. The catalyst "selectivity" of products was defined as the mole fraction of each product.[112] Fig. 41a shows the typical experimental results of flowerlike CeO_2–Cu catalyst, in which the selectivity of each product and the conversion of ethanol are shown as a function of reaction temperature in the temperature range of 200–650 °C.[112] A hydrogen-rich gas mixture was produced in a wide temperature range (300–500 °C). No liquid products were detected, such as acetone or

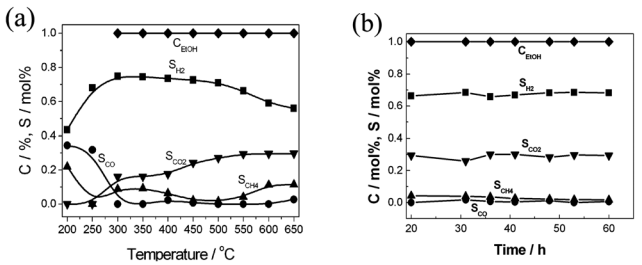

Fig. 41 (a) Effect of reaction temperature (200–650 °C) on conversion of ethanol (C_{EtOH}) and on selectivity of hydrogen (S_{H_2}), carbon monoxide (S_{CO}), carbon dioxide (S_{CO_2}), and methane (S_{CH_4}), obtained over the flowerlike CeO_2–Cu catalyst. *Experimental conditions*: mass of the catalyst 1.37 g, particle size 0.45–0.9 mm, H_2O/EtOH mol ratio 3 : 1, liquid flow rate 0.05 cm^3 min^{-1}, P = 1 atm. (b) Conversion of ethanol and selectivity of products as function of time-on-stream, obtained over the flowerlike CeO_2–Cu catalyst sample reduced by hydrogen for 2 h at 400 °C. *Experimental conditions*: T = 550 °C, others are the same as those given in (a). (Reprinted with permission from ref. 112. Copyright 2006 American Chemical Society).

acetaldehyde. At 300 °C, typical steam reforming of ethanol and water–gas shift reactions occurred obviously, the H_2 selectivity reached the maximum value of 74.9 mol%, while CO was not detected within the precision of gas chromatography. The high-temperature hydrothermal stability of this novel structure catalyst was also examined at 550 °C. Fig. 41b shows clearly that the catalyst kept excellent stability for steam reforming of ethanol at high temperature. These catalytic properties are better than those of Ni/La_2O_3,[209] $Ni–Rh–CeO_2$ and $Rh/CeO_2–ZrO_2$ catalysts.[210,211]

The effects of CeO_2 morphology on the catalytic activity of ethanol reforming was revealed by Hsiao *et al.*[212] HRTEM analysis indicated that the exposed crystal planes are {110} and {100} for nanorods but {100} for nanocubes. The catalysts as-prepared showed good H_2 selectivity compared to that of irregular CeO_2 nanoparticles. Both nanorods and nanocubes with {110} and {100} dominant surfaces showed initially enhanced catalytic activity of ethanol reforming, however, the activities gradually decreased with time because of an altered CeO_2 morphology at 800 °C. The authors suggested that a possible way to maintain the stability of CeO_2 nanocrystals is doping with another stable metal, such as Ti or Zr.[212]

Flytzani-Stephanopoulos *et al.*[213] found that a small amount (<1 at.%) of fully dispersed gold on ceria nanorods exhibits good catalytic activity and selectivity for the low-temperature (<250 °C) methanol steam reforming reaction. Fully dispersed gold (<1 nm) on the {110} surfaces of ceria nanorods catalyze the steam reforming of methanol (SRM) reaction. In contrast, gold nanoparticles (~3 nm) on the {100} surface of ceria nanocubes are inactive for both the SRM and WGS reactions.[213]

6.3. Solid oxide fuel cells

In recent years, considerable attention has been focused on solid oxide fuel cells (SOFCs) due to their potential for providing clean and reliable electric power.[14,15] It has been reported that ceria-based ion conductors have a high resistance to carbon deposition,[13,15,214,215] which permits the direct supply of dry hydrocarbon fuels to the anode. Gorte's group first demonstrated directly electrochemical oxidation of the available hydrocarbons fuels ranging from methane to toluene using a solid oxide fuel cell at 973 and 1073 K with a composite anode of copper and ceria (or samaria-doped ceria).[13] In this anode design, Cu is used primarily as the current collector and CeO_2 imparts catalytic activity for the oxidation reactions. An advantage of Cu/CeO_2/YSZ anodes is its high sulfur tolerance. The cell with Cu/CeO_2/YSZ anodes can operate on fuels with sulfur contents up to ~400 ppm without significant loss in performance.[216] In addition, these anodes also have inherently high redox stability.

Ceria nanoparticles were added to a conventional Ni/YSZ anode by infiltration of an aqueous solution of cerium nitrate followed by heating in air to effectively enhance its capability of sulfur tolerance.[217] Fig. 42 displays the results obtained for cells with and without adding ceria while operating on $H_2S–H_2$ mixtures at 973 K. For the cell without ceria, the addition of 40 ppm H_2S to the H_2 stream caused the cell voltage to drop to zero within several minutes. In contrast, for the cell with an anode loading with CeO_2 nanoparticles, the addition of 40 ppm H_2S caused the cell voltage to drop from 0.78 to 0.6 V in several minutes, but then the performance was kept relatively stable for

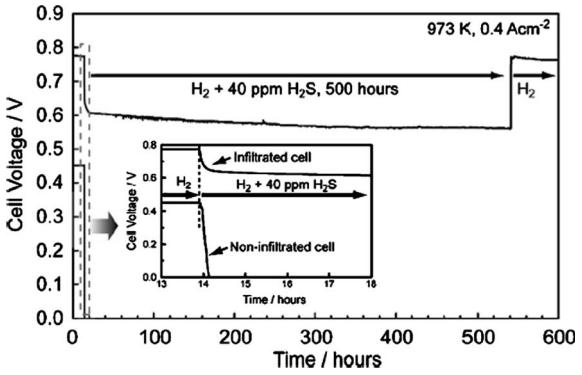

Fig. 42 Cell voltage as a function of time for SOFC operated with a fuel consisting of H_2 and H_2 plus 40 ppm H_2S. Ceria was added to the Ni/YSZ anode in one of the cells by infiltration. (Reproduced from ref. 217 by permission of ECS- The Electrochemical Society.)

over 500 h. The initial performance was also regained when the fuel was switched back to pure H_2. One interpretation for this result is that the initial decay was due to poisoning of Ni and then ceria acted as the electrocatalyst during the period with lower and stable performance.[217]

The presence of CeO_2-based oxides in the anodes of SOFCs with oxygen-ion-conducting electrolytes significantly lowering the activation overpotential for hydrogen oxidation has been demonstrated in numerous literature. However, porous and composite electrode structures with ill-defined geometry and uncontrolled interfacial properties have been widely used in most studies.[218] Haile's group recently demonstrated clearly, through the use of ceria–metal structures with well-defined geometries and interfaces (Fig. 43),[218] that the near-equilibrium H_2 oxidation reaction pathway was dominated by electrocatalysis at the oxide–gas interface with minimal contributions from the oxide–metal–gas triple-phase boundaries, even for structures with reaction-site densities approaching those of commercial SOFCs.[218] On varying the metal-catalysed reaction-site (3PB) density by a factor of 16 while holding the ceria-catalysed reaction-site (2PB) density constant, it was observed that the electrochemical activity remained essentially unchanged and was moreover independent of the choice of metal (Fig. 44). The same behavior has been observed across a wide range of hydrogen and water vapor partial pressures. This finding demonstrates ceria nanostructuring may be an effective route to enhanced activity, rather than the traditional paradigm of metal–catalyst nanostructuring.[218]

In 2005, Barnett's group reported a new SOFC that combines a $Ru–CeO_2$ catalyst layer with a conventional anode, allowing internal reforming of iso-octane without coking, making this solid oxide fuel cell a promising candidate for practical and efficient fuel cell applications.[219] The cell with $Ce_{0.85}Sm_{0.15}O_{1.925}$ (SDC) as electrolyte yielded maximum power densities of ~0.35 W cm^{-2} at 570 °C, a value comparable to those reported for other SDC based electrolyte cells operated on H_2. However, as pointed by the authors, one of the drawbacks to the catalyst layer is that it reduces the rate at which fuel can diffuse to the anode, thereby decrease cell power density. We improved the structure of the fuel cells by using the porous flowerlike CeO_2 microsphere as the support of catalysts.[119] As shown in Fig. 45, the fuel cell with a

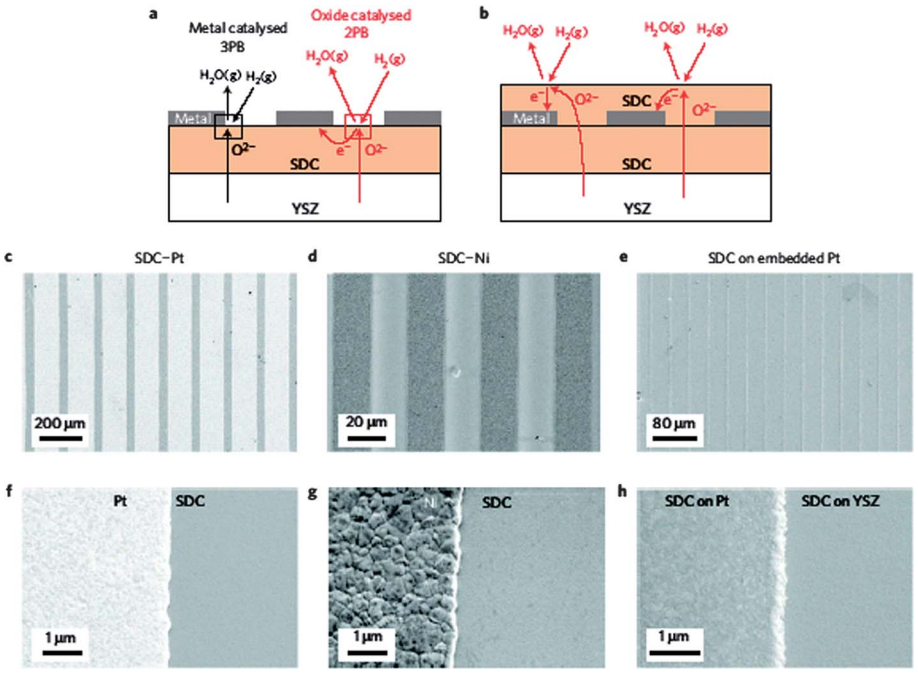

Fig. 43 Patterned metal on thin-film ceria as a model system to study competing electrochemical reactions. (a) Schematic depicting the two macroscopic reaction sites present in a ceria–metal patterned electrode and the corresponding surface reaction and bulk diffusion steps. Bulk pathways involving the metal are not shown. (b) Patterned electrode with an embedded current collector that eliminates contribution from the metallic phase. (c–h) Planar SEM images of corresponding electrode structures recorded after electrochemical characterization under H_2–H_2O–Ar atmospheres at 650 °C. (SDC = $Sm_{0.2}Ce_{0.8}O_{1.9-\delta}$, YSZ = $Y_{0.16}Zr_{0.84}O_{1.92}$). (Reprinted from ref. 218 with permission from Nature Publishing Group.)

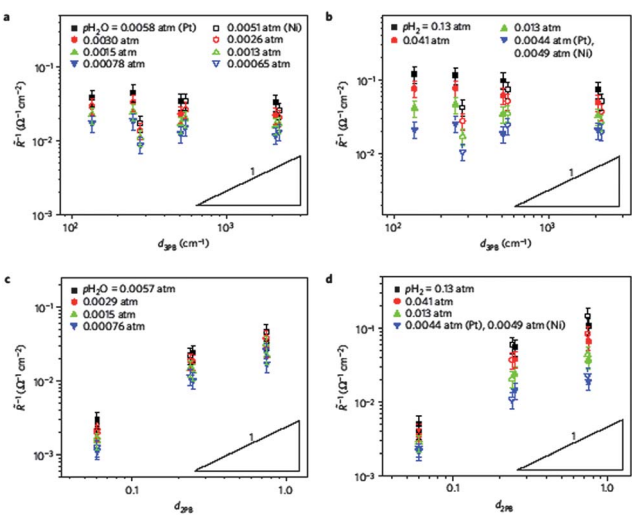

Fig. 44 Electrochemical activity in ceria–metal model electrodes. Filled symbols, Pt; open symbols, Ni. (a–d) Activity as a function of the metal-catalysed, 3PB reaction-site density at 650 °C (with the nominal 2PB density held constant at 0.5) (a and b) and the ceria-catalysed, 2PB reaction-site density (with the nominal 3PB density held constant at 125 cm^{-1}) (c and d) $\tilde{R}$ represent resistance values normalized by the total electrode area. In (a) and (c), the hydrogen partial pressure is held constant at 0.013 atm (Pt) and at 0.016 atm (Ni); in (b), the water vapor pressure is held constant at ~0.0058 atm (Pt) and at ~0.0052 atm (Ni); in (d), the water vapor pressure is held constant at ~0.0057 atm. Error bars indicate the variation in the electrode resistance of nominally identical ceria films deposited simultaneously. (Reprinted from ref. 218 with permission from Nature Publishing Group.)

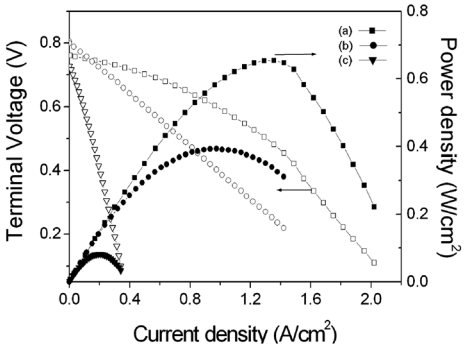

Fig. 45 Voltage and power density *versus* current density for the anode supported SOFCs: (a) with a catalyst layer, flowerlike CeO_2 microspheres loaded with Ru, (b) with a catalyst layer, bulk mesoporous CeO_2 powder loaded with Ru, (c) without a catalyst layer, tested in 5% iso-octane-9% air-3%H_2O–83%CO_2 at 100 ml min^{-1} in the anode and ambient air in the cathode at 600 °C. (Reprinted from ref. 119 with permission from Elsevier Ltd.)

Ru/flowerlike CeO_2 catalyst layer generates a maximum power density up to 0.654 W cm^{-2} at 600 °C. The enhanced performance was ascribed to improved mass transport processes in the porous structure of flowerlike microspheres. When tested with biogas as fuel, the cells also showed good performance.

6.4. Photocatalysis

Heterogeneous photocatalysis is an emerging technique valuable for renewable energy as well as water and air purification and

remediation.[220] Corma *et al.* prepared a hierarchically structured mesoporous material by self-assembly of 5 nm CeO_2 pretreated nanoparticles in the presence of a structure directing agent (poly(alkylene oxide) block polymer).[221] The walls of this hexagonal structured CeO_2 material are formed from the primary nanoparticles. The material possesses large pore volumes, high surface areas, and marked thermal stability. It also exhibits a photovoltaic response (Fig. 46), which is directly derived from the nanometric particle size because normal CeO_2 does not show this response. Organic-dye-free solar cells using nanometric ceria particles (in both mesostructured and amorphous forms) as the active component, show efficiencies dependent on the illuminating power.[221]

At present, developing efficient photocatalytic systems for water splitting is urgently needed since it can eventually lead to the production of solar fuels.[222–225] In spite of the large research effort in the field of photocatalysis for visible-light water splitting, the number of semiconductors that have decent photocatalytic activity under visible-light illumination is still limited, and the vast majority of the studies are carried out with modified TiO_2.[225–227] A novel efficient CeO_2-based photocatalysts with visible-light activity has been developed recently by Primo *et al.* with comparable or higher efficiency than those currently known.[228] Fig. 47 shows the selected plots of the oxygen formed over the time for visible light illumination for Au–CeO_2 catalysts. It indicates that 1.0wt%Au renders a more efficient photocatalyst than 3.0wt%Au. With UV irradiation, the ceria sample (A) prepared by the novel biopolymer template procedure with a smaller particle size is far more efficient than the commercial CeO_2 (B) with a larger particle size. Interestingly, for titanium oxide and other semiconductors, the photocatalytic activity under UV is considerably reduced using visible light, whereas the performance for Au–CeO_2 is better using visible light. It is worth noting that with the use of Au–CeO_2 (A) the final moles of oxygen evolved are higher than those obtained for WO_3 with UV light.

CeO_2 nanomaterials have also been used in photocatalytic hydrogen production. Oriented hexagonal CeO_2 nanorods (NRs) with {110} planes as the main exposed surfaces were directly

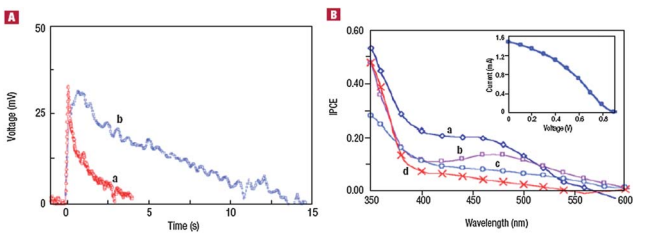

Fig. 46 Comparison of the charge current and spectral response of CeO_2 nanoparticles and TiO_2. (A) temporal profile of the voltage measured for cells comprising a film of semiconductor between a transparent conductive glass and an aluminum counter electrode on 355 nm laser excitation (5 mJ per pulse width). (a) TiO_2; (b) CeO_2. The signals correspond to a single laser shot, and have not been averaged. (B) IPCE *versus* wavelength for a solar cells based on (a) La^{3+}–CeO_2, (b) Zr^{4+}–CeO_2, and (c) CeO_2. For comparison, (d) the photoresponse of an analogous solar cell based on TiO_2, has also been included. Inset, photocurrent-voltage plot of a solar cell based on La^{3+}–CeO_2. (Reprinted from ref. 221 with permission from Nature Publishing Group.)

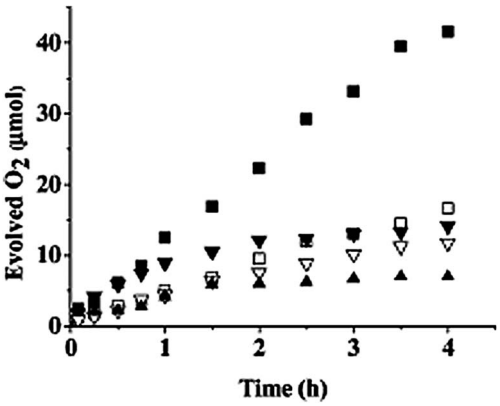

Fig. 47 (a) Oxygen evolved upon visible light ($\lambda > 400$ nm) illumination of an aqueous $AgNO_3$ suspension containing the photocatalysts. ■ Au (1.0 wt%)/CeO_2 (A); □ Au (1.0 wt%)/CeO_2 (B); ▼ Au(3.0 wt%)/CeO_2 (A); ▽ Au (3.0 wt%)CeO_2 (B); ▲ WO_3. CeO_2 (A) was prepared by biopolymer template synthesis while CeO_2 (B) was obtained from Aldrich. (Reprinted with permission from ref. 228. Copyright 2011 American Chemical Society).

grown on Ti substrates *via* a simple template-free electrochemical method.[229] The photocatalytic activity of CeO_2 NRs was studied in water splitting reaction and compared with that of commercial CeO_2, CdS and TiO_2 (P25). Fig. 48 shows the hydrogen evolution rates of samples with Na_2S–Na_2SO_3 as sacrificial agents. It can be seen that the activity of CeO_2 NRs is higher than those of commercial CeO_2 and CdS. The hydrogen evolution rate of CeO_2 NRs reached 741 μmol g^{-1}. With methanol as a sacrificial agent, the hydrogen evolution rate of CeO_2 NRs is much higher than that of the commercial CeO_2 and P25 (Fig. 48b). Furthermore, the photocatalytic activity of CeO_2 NRs in the Na_2S–Na_2SO_3 system is about four times higher than that in the methanol system, indicating the consumption of holes in Na_2S–Na_2SO_3 aqueous solution is more efficient than that in methanol aqueous solution.[229]

For environmental remediation, CeO_2 nanomaterials have also potential application. Recently, Tang *et al.*[230] demonstrated that CeO_2 nanotubes exhibited a markedly enhanced photocatalytic activity and stability compared with the counterpart of CeO_2 nanoparticles and commercial TiO_2 (P25) toward the degradation of aromatic benzene, a well-known toxic pollutant that commonly occurs in urban ambient air and is of significant concern regarding environmental health because of its toxic,

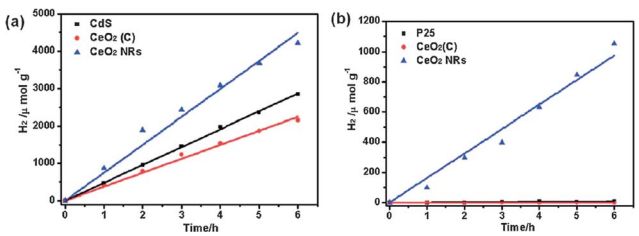

Fig. 48 Hydrogen production rates of samples in (a) Na_2S–Na_2SO_3 (0.43 M:0.5 M) mixture solution, and (b) 20vol% methanol aqueous solution. (Reprinted from ref. 229 with permission from Royal Society of Chemistry.)

mutagenic, or carcinogenic properties. Fig. 49 shows the time-online photocatalytic results for the gas-phase degradation of benzene over the samples of CeO_2–NTs, CeO_2–NPs and P25. During the reaction of 22 h, the sample of CeO_2–NT exhibits the best photocatalytic performance toward the gas-phase degradation of benzene in view of the constant conversion ratio of benzene. After the reaction of 10 h, the produced amount of CO_2 over CeO_2–NTs is nearly stable at 29 ppm. In contrast, the samples of both CeO_2–NPs and commercial P25–TiO_2 nanoparticles display a quite unstable photocatalytic activity toward the gas degradation of benzene. For the CeO_2–NP sample, the conversion ratio of benzene at the initial stage is 2.2%; it is decreased to 1.4% after reaction for 22 h. The improved performance was ascribed to the enhanced light absorption and scattering of the 1D nanotube geometry.[230]

In addition, significant progresses have been achieved recently in enabling the thermochemical cycles based on cerium oxide redox reactions to produce solar fuels.[231] Haile *et al.*[232] demonstrated the production of H_2 from H_2O and of CO from CO_2 using a solar cavity-receiver containing porous monolithic ceria. The same group also reported CeO_2-doped with 15atomic% samarium as an efficient system to produce syngas (from water and CO_2, in the absence of a metal catalyst) or methane (in the presence of Ni as the catalyst).[233] The oxide is pretreated at 1500 °C (24 h) in an oxygen-free atmosphere and then interacted with a flow of water and oxygen in a carrier gas to generate hydrogen, methane, and CO. Steinfeld *et al.*[234] demonstrated syngas production by simultaneous splitting of H_2O and CO_2 *via* a thermochemical redox cycle inside a solar cavity-receiver containing porous ceria felt directly exposed to concentrated thermal radiation. In the first endothermic step at 1800 K, ceria is thermally reduced to an oxygen deficient state. In the second exothermic step at 1100 K, syngas is produced by re-oxidizing ceria with a gas mixture of H_2O and CO_2. Ten consecutive H_2O/CO_2 gas splitting cycles have been performed for 8 h, yielding a constant and stable syngas composition.

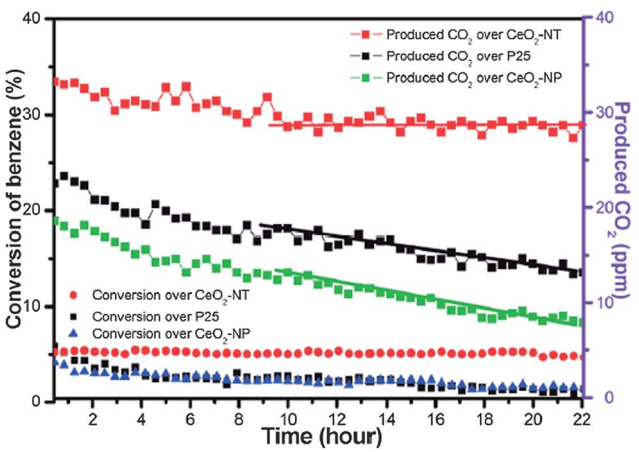

Fig. 49 Time-online data for gas-phase photocatalytic degradation of benzene over the samples of commercial P25, CeO_2 nanoparticles (NPs) and the as-prepared CeO_2 nanotubes (NTs). (Reprinted from ref. 230 with permission from Royal Society of Chemistry.)

6.5. Sensors

Measurement and control oxygen content are critical in many areas such as the environment, industry, transportation, medicine and agriculture. Solid state electrolyte oxygen type sensors are widely used in these areas. Jasinski *et al.*[9] prepared a nanocrystalline undoped ceria oxygen sensor consisting of a thin film of CeO_2 with platinum interdigital electrodes. The dense thin films of CeO_2 were prepared by spin coating a polymer precursor solution onto a sapphire substrate (Fig. 50a). The electrical conductivities of thin film ceria as a function of oxygen partial pressure and temperature are shown in Fig. 50b. They follow $(P_{O2})^{-1/4}$ behavior for the selected temperature range from 550 to 750 °C with only a very small deviation. The relationship

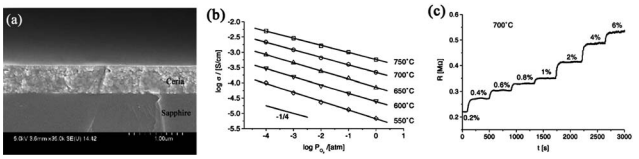

Fig. 50 (a) Cross-section of CeO_2 thin film on sapphire, (b) electrical conductivity of CeO_2 thin film on sapphire, (c) the time response of the ceria sensor DC resistance on the changes of oxygen concentration. (Reprinted from ref. 9 with permission from Elsevier Ltd.)

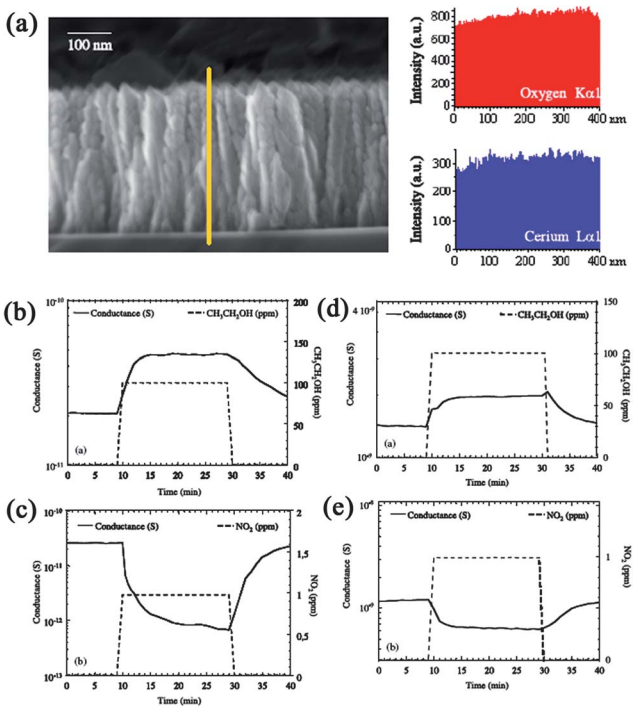

Fig. 51 (a) Representative cross-sectional SEM image of columnar CeO_2 specimen obtained at 350 °C on Si (100) and the corresponding line acan for O $K_{\alpha 1}$ and $CeL_{\alpha 1}$ along the marked line; (b) CH_3CH_2OH and (c) NO_2 sensing curves of the columnar CeO_2 nanostructures deposited on Al_2O_3 at 400 °C; (d) CH_3CH_2OH and (e) NO_2 sensing curves of a continuous CeO_2 layer deposited on Al_2O_3 at 400 °C. In all the cases, the working temperature and relative humidity were 200 °C and 40%, respectively. (Reprinted from ref. 236 with permission from IOP Publishing Ltd.)

$(P_{O2})^{-1/4}$ corresponds to extrinsic charge compensation, indicating the concentration of oxygen vacancies related to the acceptor impurity concentration. These results are in contrast to Beie's results,[8] in which the sensor followed $(P_{O2})^{-1/6}$ behavior and was attributed to intrinsic charge compensation. This difference may be explained by different levels of purity of ceria and different microstructure of the films.[235]

Another impressive example of sensor applications is columnar CeO_2 nanostructures, shown in Fig. 51a, prepared by Barreca *et al.* with a chemical vapor deposition (CVD) on Si(100) and Al_2O_3 substrates.[236] Fig. 51b and c present the isothermal conductance variation for a representative columnar CeO_2 specimen upon exposure to 100 ppm ethanol (a reducing species) and 1 ppm NO_2 (an oxidizing gas), respectively, at a working temperature of 200 °C. This particular ethanol concentration value is lower than the detection limit required for a breath analyzer (200 ppm, corresponding approximately to 0.6 g alcohol per liter in human blood).[237] The sensor response was 1.3 at the relatively low working temperature while the response for a continuous CeO_2 thin film is only 0.38 (Fig. 51d). Upon introducing NO_2 as a square concentration pulse of 1 ppm into the test chamber, the columnar CeO_2 nanostructured displays a conductance decrease (Fig. 51c) due to the electron-withdrawing effects following the direct NO_2 adsorption onto the specimen surface.[238] The sensor response at 200 °C was 50 times higher than that of the continuous film under the same working conditions (Fig. 51e). The higher sensitivity in the detection of gaseous ethanol and NO_2 with respect to continuous CeO_2 thin films demonstrates the promise of development of nanosized CeO_2 sensor devices.[236]

6.6. Oxygen permeation membranes

Nanocrystalline CeO_2 thin films were fabricated on porous cerium oxide substrates with both sol–gel and sputtering deposition techniques and studied for oxygen permeation membranes.[239] The sputtered cerium oxide buffer layer can be seen to grow in a columnar shape from the substrate–film interface (Fig. 52). The high-magnification SEM image, Fig. 52b, clearly shows the columnar nature of the sputtered layer with a mean column diameter of 90 nm and the dense sol–gel layer with a mean grain size of 50 nm and a film thickness of 500 nm.

Fig. 53 shows the effect of oxygen partial pressure driving force on the predicted permeation of nanocrystalline CeO_2 membranes at 800 °C. The flux predictions were calculated given a constant feed side partial pressure of 0.21 atm, while the downstream concentration of oxygen was varied between 10^{-2} and 10^{-6}, resulting in an oxygen flux varying from 0.028 to 0.114 μmol cm^{-2}. In the absence of surface limitations, the oxygen flux can exceed 1 μmol cm^{-2} s^{-1} for films with ionic conductivities in the order of 10^{-3} S cm^{-1}, approaching the flux target of oxygen–air separation membranes by using solely CeO_2 as a single material system. The CeO_2 thin film showed a measurable oxygen flux of 0.014 μmol cm^{-2} s^{-1} at 800 °C, confirming mixed ionic and electronic conductivities and demonstrating the feasibility of utilizing nanocrystalline CeO_2 as an oxygen separation membrane with grain size as a design parameter.[239] The electronic conduction is introduced by the nanocrystalline materials structure rather than second phase additions, for example, noble metal additions commonly added in the dual phase membranes. This result is consistent with recent results reported by Haile's group using ceria nanostructuring as a route to enhance activity, rather than the traditional paradigm of metal–catalyst nanostructuring.[218]

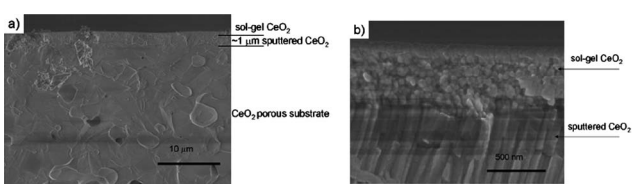

Fig. 52 SEM images: (a) Large view of porous substrate, 1 μm sputtered cerium oxide layer and dense sol–gel cerium oxide layer, (b) close-up of dense sol–gel cerium and sputtered cerium oxide buffer layer. (Reproduced from ref. 239 by permission of ECS - The Electrochemical Society.)

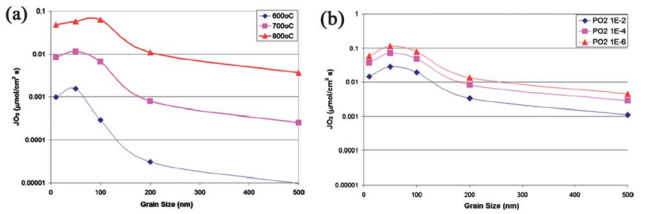

Fig. 53 (a) Oxygen flux [μmol cm^{-2} s^{-1}] as a function of grain size and temperature (b) Oxygen flux [μmol cm^{-2} s^{-1}] at 800 °C as a function of grain size and oxygen partial pressure on the permeate side varying from 10^{-2} to 10^{-6} atm. All were calculated from the Wagner relation equation with size-dependent data from ref. 240. (Reproduced from ref. 239 by permission of ECS - The Electrochemical Society.)

6.7. Biomedical applications

Recent researches have demonstrated that ceria nanoparticles possess antioxidant activity at physiological pH values, and the potential uses of these materials in biomedical applications, such as protection against radiation damage, oxidative stress, and inflammation.[22,23,241–244] The ability of these nanoparticles to act as an antioxidant lies in their ability to reversibly switch from Ce^{3+} to Ce^{4+}.[23] Moreover, the synthesis of biocompatible dextran-coated nanoceria (DNC) and its enhanced stability in aqueous solution has been recently reported.[242] Conjugation with targeting ligands makes ceria nanoparticles an effective nanocatalyst and detection tool in immunoassays.

Das *et al.* evaluated the auto-catalytic anti-oxidant behavior and biocompatibility of cerium oxide nanoparticles for applications in spinal cord repair and other diseases of the central nervous system.[241] Ceria nanoparticles show a mechanism that the engineered particle as a new material for life science applications with remarkable antioxidant activity and pseudo-infinite half-life. The auto-regenerative anti-oxidant property of these nanoparticles is the key to its neuroprotective action. To demonstrate the auto-catalytic property of the engineered ceria nanoparticles, they studied the UV-visible spectroscopy of a nano-ceria sol treated with 10 mM hydrogen peroxide (Fig. 54). In this reaction, hydrogen peroxide provides a source of hydroxyl radicals to mimic oxidative stress found *in vivo*.[241] The

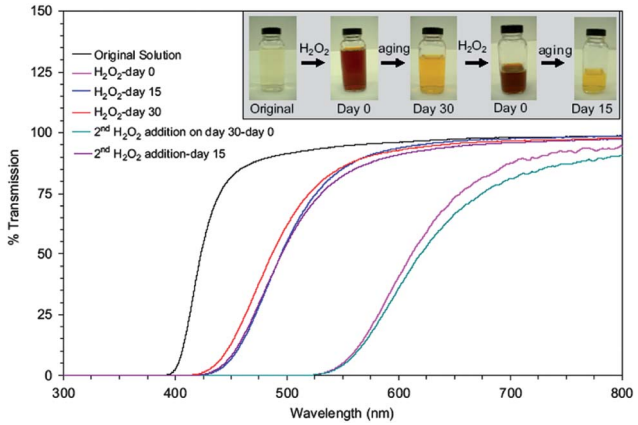

Fig. 54 UV-visible study of cerium oxide nanoparticles treated with hydrogen peroxide at different time intervals. (Reprinted from ref. 241 with permission from Elsevier Ltd.)

UV-visible spectrum of a sample containing the nano-ceria solution was used as the control (black trace-in the graph). They added hydrogen peroxide to the solution and observed a shift in the spectrum to the right or to the lower energy portion of the spectrum (pink trace). This shift is postulated to be due to a change in the oxidation state from Ce^{3+} to Ce^{4+}. The nano-ceria sample treated with hydrogen peroxide was then kept in the dark for 30 days. UV-visible spectra of these samples were then taken at day 15 and day 30 (blue and red traces for the day 15 and day 30 spectra, respectively). A gradual shift in the spectra to the left was observed over time. This gradual higher energy shift suggests the regeneration ($Ce^{4+} \rightarrow Ce^{3+}$) of the ceria nanoparticles.[241]

Asati *et al.*[22] reported that ceria nanoparticles possess unique oxidase-like activity, as they can facilitate the fast oxidation of organic dyes and small molecules in slightly acidic conditions without the need of hydrogen peroxide. They studied the effect of the nanoparticle size on the catalytic activity of nanoceria. As shown in Fig. 55, their results showed that nanoceria's ability to oxidize 3,3′,5,5′-tetramethylbenzidine (TMB) varies with nanoparticle size in the order *is*PNC (5 nm) > *sw*PNC (12 nm) > *is*DNC (14 nm) > *sw*DNC (100 nm). Interestingly, the nanoparticles with a thin poly-(acrylic acid) coating (*is*PNC) have a higher catalytic activity than those with a thicker dextran coating (*sw*DNC). These results demonstrate that this unique aqueous oxidase-like of nanoceria can be used in a wide range of new potential applications in biotechnology, environmental chemistry, and medicine.[22]

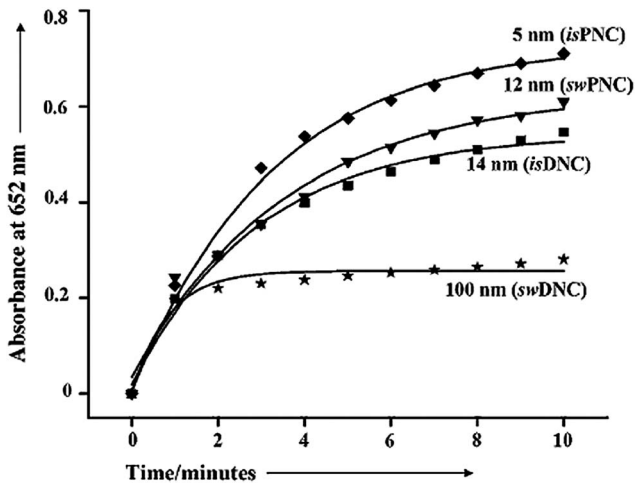

Fig. 55 Nanoceria-promoted oxidation of TMB is size-dependent. At pH 4.0, smaller ceria nanoparticles show higher oxidase-like activity than larger nanoparticles. (Reprinted from ref. 22 with permission from John Wiley and Sons, Inc.)

Radiation therapy has been one of the most widely utilized procedures for the treatment of cancer. During this process, free radicals are formed through ionizing reactions that are then capable of destroying normal tissues. Thus, normal cells can be protected from radiation while the tumor cells are targeted. The related researches have been an important area of interest since the 1950s. Tarnuzzer *et al.*,[23] for the first time, demonstrated nanoceria can confer radioprotection to a normal human breast line but not to a human breast tumor line, MCF-7. The antioxidant function of nanoceria was ascribed to the presence of the mixed valence state of Ce^{3+} and Ce^{4+} on the surface, induced by the oxygen vacancies.[23] Scavenging the free radicals generated by irradiation was achieved by changing its oxidation state from Ce^{3+} to Ce^{4+} in ceria nanoparticles. Another complex surface chemical reaction may be related to renewing the oxidation state from Ce^{4+} to Ce^{3+}. They suggested that there is an auto-regenerative reaction cycle ($Ce^{3+} \rightarrow Ce^{4+} \rightarrow Ce^{3+}$) continuing on the surface of ceria nanoparticles and this may be the mechanism by which it provides the material with a remarkable antioxidant activity.[23] The auto-regenerative antioxidant property of these nanoparticles is a key component of its radio-protective action.

Recent studies have shown that free radical scavenging can be achieved by the introduction of CeO_2 nanoparticles into mammalian cells. The efficacy of CeO_2 nanoparticles to scavenge reactive oxygen species has also been demonstrated *in vivo*. Tsai *et al*[245] prepared crystalline CeO_2 nanoparticles with an average particle size of 3.7 nm by a reverse micelle method. When tested *in vitro*, the CeO_2 nanoparticles were deposited in the cytoplasm of insulin-secreting cells and the intracellular concentration of CeO_2 nanoparticles reached 0.35 pg per cell. Their results demonstrated CeO_2 nanoparticles are effective free radical scavengers within βTC-tet cells. The CeO_2 nanoparticles provide an effective means to improve cellular survival in settings wherein cell loss due to oxidative stress limits native function.[245] Many potential applications in medicine can be expected to benefit from the free radical scavenging abilities of CeO_2 nanoparticles.

Concern of the safety of engineered nanomaterials must be well addressed before their applications. The toxicity of ZnO, CeO_2 and TiO_2 has been compared recently based on dissolution and oxidative stress properties.[246,247] The results showed that CeO_2 nanoparticles can suppress the generation of reactive oxygen species (ROS) production and induced cellular resistance to an exogenous source of oxidative stress and protect cells from oxidant injury. Ceria nanoparticles have very low or no toxicity and are long-lived and can confer their beneficial effect for extended periods of time without redosing.[248,249]

7. Conclusions and outlook

This review highlights the recent progress in the preparation, properties, new characterization approaches, and theoretical study of nanostructured ceria-based materials. Some typical applications regarding ceria-based nanomaterials have also been demonstrated. With great progress being made in the synthesis of nanostructured ceria-based materials, there are fascinating new opportunities and challenges for materials scientists. Although considerable attention has been devoted to synthesis of ceria nanomaterials in the past years, future studies should focus more on a better understanding of how synthetic techniques, composition, size, and morphology affect the properties of materials. In this aspect, theoretical calculation can provide a guideline on the rational design of highly reactive CeO_2-based catalysts. It has been demonstrated that ceria not only works as a support for catalytic reactions, but also functions as an electronic modulator for the electron-transfer process in some catalytic processes. The valence and defect structure of CeO_2 play an important role for various applications. The control of the density and the nature of oxygen vacancies could provide a means for tailoring the reactivity of ceria-based catalysts. Thus, precise selection and control of metal–ceria interfaces in designing catalysts could lead to better activity and selectivity for a specific catalytic reaction. The combination of new characterization approaches, *e.g.* STM, DFM, and modern aberration-corrected TEM, with the first-principles calculations can well present the surface and subsurface properties of ceria and thus clarify the reactions occurring at the interfaces of catalysts. Simulation method is an efficient way to understand the formation mechanism of nanomaterials from the atomic level. An approach based on predictive simulations and the first principles calculations is necessary in accelerating the identification or design of appropriate CeO_2-based nanomaterials as well.[250]

While some encouraging results have been achieved, the development of simple and cost-effective synthetic and fabrication processes for CeO_2-based nanomaterials are still desirable and essential for many applications. Solvothermal, hydrothermal synthesis and electrospinning[251] are promising methods for preparing nanoarchitectures in energy related applications. In addition, the long-term stability of the CeO_2 nanomaterials under high-temperature and reaction conditions is of potential concern. However, good hydrothermal stability has been showed in porous flowerlike CeO_2 microspheres. In the future, ceria-based nanomaterials will play more important role in energy conversion (*e.g.*, fuel cells and the renewable production of fuels from solar energy), energy storage (*e.g.*, lithium-air batteries), environmental protection and remediation (*e.g.*, treatment of toxic contaminants), as well as the new field of biomedical applications (*e.g.*, anti-oxidant agent, free radical scavenging and immunoassays).

Acknowledgements

This work is financially supported by the National Science Foundation of China (NSFC) (Grant no. 51172275), the National Key Basic Research Program of China (Grant no. 2012CB215402), and the Institute of Physics (IOP) start-up funding for the talents.

References

1 T. J. Ahrens, *Global Earth Physics: a Handbook of Physical Constants*, American Geophysical Union, Washington, DC, 1995.
2 T. J. Ahrens, *Global Earth Physics: a Handbook of Physical Constants*, American Geophysical Union, Washington, DC, 1995.
3 D. Lide, *CRC Handbook of Chemistry and Physics*, CRC Publishing Co., Boca Raton, FL, 88th edn, 2007.
4 A. Trovarelli, Catalytic properties of ceria and CeO_2-containing materials, *Catal. Rev. Sci. Eng.*, 1996, **38**, 439–520.
5 J. Kaspar, P. Fornasiero and M. Graziani, Use of CeO_2-based oxides in the three-way catalysis, *Catal. Today*, 1999, **2**, 285–298.
6 Q. Fu, A. Weber and M. Flytzani-Stephanopoulo, Nanostructured Au–CeO_2 catalysts for low-temperature water–gas shift, *Catal. Lett.*, 2001, **77**, 87–95.
7 Q. Fu, H. Saltsburg and M. Flytzani-Stephanopoulo, Active nonmetallic Au and Pt species on ceria-based water–gas shift catalysts, *Science*, 2003, **301**, 935–938.
8 H. J. Beie and A. Gnörich, Oxygen gas sensors based on CeO_2 thick and thin films, *Sens. Actuators, B*, 1991, **4**, 393–399.
9 P. Jasinski, T. Suzuki and H. U. Anderson, Nanocrystalline undoped ceria oxygen sensor, *Sens. Actuators, B*, 2003, **95**, 73–77.
10 M. Stoukides, Solid-electrolyte membrane reactors: current experience and future outlook, *Catal. Rev. Sci. Eng.*, 2000, **42**, 1–70.
11 X. Yin, L. Hong and Z. L. Liu, Oxygen permeation through the LSCO-80/CeO_2 asymmetric tubular membrane reactor, *J. Membr. Sci.*, 2006, **268**, 2–12.
12 B. C. H. Steele, Appraisal of $Ce_{1-y}Gd_yO_{2-y/2}$ electrolytes for IT-SOFC operation at 500 °C, *Solid State Ionics*, 2000, **129**, 95–110.
13 S. D. Park, J. M. Vohs and R. J. Gorte, Direct oxidation of hydrocarbons in a solid oxide fuel cells, *Nature*, 2000, **404**, 265–267.
14 C. W. Sun, R. Hui and J. Roller, Cathode materials for solid oxide fuel cells: a review, *J. Solid State Electrochem.*, 2010, **14**, 1125–1144.
15 C. W. Sun and U. Stimming, Recent anode advances in solid oxide fuel cells, *J. Power Sources*, 2007, **171**, 247–260.
16 X. D. Feng, D. C. Sayle, Z. L. Wang, M. S. Paras, B. Santora, A. C. Sutorik, T. X. T. Sayle, Y. Yang, Y. Ding, X. D. Wang and Y. S. Her, Converting ceria polyhedral nanoparticles into single-crystal nanospheres, *Science*, 2006, **312**, 1504–1508.
17 S. Armini, J. De Messemaeker, C. M. Whelan, M. Moinpour and K. Maex, Composite polymer core-ceria shell abrasive particles during oxide CMP: a defectivity study, *J. Electrochem. Soc.*, 2008, **155**, H653–H660.
18 I. Porqueras, C. Person, C. Corbella, M. Vives, A. Pinyol and E. Bertran, Characteristics of e-beam deposited electrochromic CeO_2 thin films, *Solid State Ionics*, 2003, **165**, 131–137.
19 A. Azens, L. Kullman, D. D. Ragan, C. G. Granqvist, B. Hjörvarsson and G. Vaivars, Optical and electrochemical properties of dc magnetron sputtered Ti–Ce oxide films, *Appl. Phys. Lett.*, 1996, **68**, 3701–3703.
20 N. Ozer, Optical properties and electrochromic characterization of sol–gel deposited ceria films, *Sol. Energy Mater. Sol. Cells*, 2011, **68**, 391–400.
21 T. Morimoto, H. Tomonaga and A. Mitani, Ultraviolet ray absorbing coatings on glass for automobiles, *Thin Solid Films*, 1999, **351**, 61–65.
22 A. Asati, S. Santra, C. Kaittanis, S. Nath and J. M. Perez, Oxidase-like activity of polymer-coated cerium oxide nanoparticles, *Angew. Chem., Int. Ed.*, 2009, **48**, 2308–2312.
23 R. W. Tarnuzzer, J. Colon, S. Patil and S. Seal, Vacancy engineered ceria nanostructures for protection from radiation-induced cellular damage, *Nano Lett.*, 2005, **5**, 2573–2577.
24 H. L. Tuller, Ionic conduction in nanocrystalline materials, *Solid State Ionics*, 2000, **131**, 143–157.
25 A. Bumajdad, J. Eastoe and A. Mathew, Cerium oxide nanoparticles prepared in self-assembled systems, *Adv. Colloid Interface Sci.*, 2009, **147–148**, 56–66.
26 Q. Yuan, H. H. Duan, L. L. Li, L. D. Sun, Y. W. Zhang and C. H. Yan, Controlled synthesis and assembly of ceria-based nanomaterials, *J. Colloid Interface Sci.*, 2009, **335**, 151–167.
27 W. Feng, L. D. Sun, Y. W. Zhang and C. H. Yan, Synthesis and assembly of rare earth nanostructures directed by the principle of coordination chemistry in solution-based process, *Coord. Chem. Rev.*, 2010, **254**, 1038–1053.

28 V. Esposito and E. Traversa, Design of electroceramics for solid oxide fuel cell applications: playing with ceria, *J. Am. Ceram. Soc.*, 2008, **91**, 1037–1051.
29 L. Vivier and D. Duprez, Ceria-based solid catalysts for organic chemistry, *ChemSusChem*, 2010, **3**, 654–678.
30 X. Guo and R. Waser, Electrical properties of the grain boundaries of oxygen ion conductors: acceptor-doped zirconia and ceria, *Prog. Mater. Sci.*, 2006, **51**, 151–210.
31 K. Schwarz, Materials design of solid electrolytes, *Proc. Natl. Acad. Sci. U. S. A.*, 2006, **103**, 3497.
32 M. Mogensen, N. M. Sammes and G. A. Tompsett, Physical, chemical and electrochemical properties of pure and doped ceria, *Solid State Ionics*, 2000, **129**, 63–94.
33 J. Lappalainen, H. L. Tuller and V. Lantto, Electronic conductivity and dielectric properties of nanocrystalline CeO_2 films, *J. Electroceram.*, 2004, **13**, 129–133.
34 S. Basu, P. S. Devi and H. S. Maiti, Synthesis and properties of nanocrystalline ceria powders, *J. Mater. Res.*, 2004, **19**, 3162–3171.
35 P. R. L. Keating, D. O. Scanlon, B. J. Morgan, N. M. Galea and G. W. Watson, Analysis of intrinsic defects in CeO_2 using a Koopmans-like GGA+U approach, *J. Phys. Chem. C*, 2012, **116**, 2443–2452.
36 R. C. Weast, D. R. Lide, M. J. Astle and W. H. Beyer, *CRC Handbook of Chemistry and Physics*, CRC Press Inc., Boca Raton, Florid, 2000.
37 F. A. Kroger and H. J. Vink, Relations between the concentrations of imperfections in crystalline solids, *Solid State Phys.*, 1956, **3**, 307–435.
38 S. R. Bishop, T. S. Stefanik and H. L. Tuller, Electrical conductivity and defect equilibria of $Pr_{0.1}Ce_{0.9}O_{2-\delta}$, *Phys. Chem. Chem. Phys.*, 2011, **13**, 10165–10173.
39 H. L. Tuller and A. S. Nowick, Defect structure and electrical-properties of non-stoichiometric CeO_2 single-crystals, *J. Electrochem. Soc.*, 1979, **126**, 209–217.
40 H. L. Tuller and A. S. Nowick, Small polaron electron-transport in reduced CeO_2 single-crystals, *J. Phys. Chem. Solids*, 1977, **38**, 859–867.
41 J. A. Kilner, Defects and conductivity in ceria-based oxides, *Chem. Lett.*, 2008, **37**, 1012–1015.
42 C. J. Zhang, A. Michaelides, D. A. King and S. J. Jenkins, Oxygen vacancy clusters on ceria: decisive role of cerium f electrons, *Phys. Rev. B: Condens. Matter Mater. Phys.*, 2009, **79**, 075433.
43 C. T. Campbell and C. H. F. Peden, Oxygen vacancies and catalysis on ceria surfaces, *Science*, 2005, **309**, 713–714.
44 A. G. Macedo, S. E. Fernandes, A. Valente, R. A. Sá Ferreira, L. D. Carlos and J. Rocha, Catalytic performance of ceria nanorods in liquid-phase oxidation of hydrocarbons with *tert*-butyl hydroperoxide, *Molecules*, 2010, **15**, 747–765.
45 J. P. Holgado, R. Alvarez and G. Munuera, Study of CeO_2 XPS spectra by factor analysis: reduction of CeO_2, *Appl. Surf. Sci.*, 2000, **161**, 301–315.
46 M. Romeo, K. Bak, J. El Fallah, F. Le Normand and L. Hilaire, XPS study of the reduction of cerium dioxide, *Surf. Interface Anal.*, 1993, **20**, 508–512.
47 S. Deshpande, S. Patil, S. V. N. T. Kuchibhatla and S. Seal, Size dependency variation in lattice parameter and valency states in nanocrystalline cerium oxide, *Appl. Phys. Lett.*, 2005, **87**, 133113.
48 N. J. Lawrence, J. R. Brewer, L. Wang, T. Wu, J. Wells-Kingsbury, M. M. Ihrig, G. Wang, Y. Soo, W. Mei and C. L. Cheung, Defect engineering in cubic cerium oxide nanostructures for catalytic oxidation, *Nano Lett.*, 2011, **11**, 2666–2671.
49 P. L. Land, Defect equilibria for extended point-defects, with application to nonstoichiometric ceria, *J. Phys. Chem. Solids*, 1973, **34**, 1839–1845.
50 J. Chen, S. Patil, S. Seal and J. F. McGinnis, Rare earth nanoparticles prevent retinal degeneration induced by intracellular peroxides, *Nat. Nanotechnol.*, 2006, **1**, 142–150.
51 G. S. Herman, Characterization of surface defects on epitaxial CeO_2 (001) film, *Surf. Sci.*, 1999, **437**, 207–214.
52 J. C. Conesa, Computer modeling of surfaces and defects on cerium dioxide, *Surf. Sci.*, 1995, **339**, 337–352.
53 E. Mamontov, T. Egami, R. Brezay, M. Koranne and S. Tyagi, Lattice defects and oxygen storage capacity of nanocrystalline ceria and ceria-zirconia, *J. Phys. Chem. B*, 2000, **104**, 11110–11116.
54 P. Gao, Z. Kang, W. Fu, W. Wang and X. Bai, Electrically driven redox process in cerium oxides, *J. Am. Chem. Soc.*, 2010, **132**, 4197–4201.
55 B. W. Sheldon and V. B. Shenoy, Space charge induced surface stresses: implications in ceria and other ionic solids, *Phys. Rev. Lett.*, 2011, **106**, 216104.
56 Y. Sekine, M. Haraguchi, M. Tomioka, M. Matsukata and E. Kikuchi, Low-temperature hydrogen production by highly efficient catalytic system assisted by an electric field, *J. Phys. Chem. A*, 2010, **114**, 3824–3822.
57 K. L. Kliewer and J. S. Koehler, Space charge in ionic crystals I. General approach with application to NACL, *Phys. Rev.*, 1965, **140**, A1226.
58 J. Maier, Ionic conduction in space charge regions, *Prog. Solid State Chem.*, 1995, **23**, 171–263.
59 H. L. Tuller, S. J. Litzelman and W. Jung, Micro-ionics: next generation power sources, *Phys. Chem. Chem. Phys.*, 2009, **11**, 3023–3034.
60 X. D. Zhou and W. Huebner, Size-induced lattice relaxation in CeO_2 nanoparticles, *Appl. Phys. Lett.*, 2001, **79**, 3512–3514.
61 X. D. Zhou, W. Huebner and H. U. Anderson, Room-temperature homogeneous nucleation synthesis and thermal stability of nanometer single crystal CeO_2, *Appl. Phys. Lett.*, 2002, **80**, 3814–3816.
62 R. A. De Souza, A. Ramadan and S. Hörner, Modifying the barriers for oxygen-vacancy migration in fluorite-structured CeO_2 electrolytes through strain: a computer simulation study, *Energy Environ. Sci.*, 2012, **5**, 5445–5453.
63 S. Azad, O. A. Marina, C. M. Wang, L. Saraf, V. Shutthanandan, D. E. McCready, A. EI-Azab, J. E. Jaffe, M. H. Engelhard, C. H. F. Peden and S. Thevuthasan, Nanoscale effects on ion conductance of layer-by-layer structures of gadolinia-doped ceriaand zirconia, *Appl. Phys. Lett.*, 2005, **86**, 131906.
64 E. Fabbri, D. Pergolesi and E. Traversa, Ionic conductivity in oxide heterostructures: the role of interfaces, *Sci. Technol. Adv. Mater.*, 2010, **11**, 054503.
65 S. Tsunekawa, R. Sahara, Y. Kawazoe and K. Ishikawa, Latice relaxation of monosize CeO_{2-x} nanocrystalline particles, *Appl. Surf. Sci.*, 1999, **152**, 53–56.
66 S. Carrettin, P. Concepción, A. Corma, J. M. L. Nieto and V. F. Puntes, Nanocrystalline CeO_2 increases the activity of Au for CO oxidation by two orders of magnitude, *Angew. Chem., Int. Ed.*, 2004, **43**, 2538–2540.
67 J. Guzman, S. Carrettin and A. Corma, Spectroscopic evidence for the supply of reactive oxygen during CO oxidation catalyzed by gold supported on nanocrystalline CeO_2, *J. Am. Chem. Soc.*, 2005, **127**, 3286–3287.
68 A. Migani, G. N. Vayssilov, S. T. Bromley, F. Illas and K. M. Neyman, Greatly facilitated oxygen vacancy formation in ceria nanocrystallites, *Chem. Commun.*, 2010, **46**, 5936–5938.
69 Y. M. Chiang, E. B. Lavik, I. Kosacki and H. L. Tuller, Defect and transport properties of nanocrystalline CeO_{2-x}, *Appl. Phys. Lett.*, 1996, **69**, 185–187.
70 Y. M. Chiang, E. B. Lavik, I. Kosacki and H. L. Tuller, Nonstoichiometry and electrical conductivity of nanocrystalline CeO_{2-x}, *J. Electroceram.*, 1997, **1**, 7–14.
71 J. E. Spanier, R. D. Robinson, F. Zhang, S. W. Chan and I. P. Herman, Size-dependent properties of CeO_{2-y} nanoparticles as studied by Raman scattering, *Phys. Rev. B: Condens. Matter*, 2001, **64**, 245407.
72 Z. Wang, S. K. Saxena, V. Pischedda, H. P. Liermann and C. S. Zha, *In situ* X-ray diffraction study of the pressure-induced phase transformation in nanocrystalline CeO_2, *Phys. Rev. B: Condens. Matter*, 2001, **64**, 012102.
73 S. Tsunekawa, T. Fukuda and A. Kasuya, Blue shift in ultraviolet absorption spectra of monodisperse CeO_{2-x} nanoparticles, *J. Appl. Phys.*, 2000, **87**, 1318–1321.
74 M. Hirano and M. Inagaki, Preparation of monodispersed cerium(IV) oxide particles by thermal hydrolysis: influence of the presence of urea and Gd doping on their morphology and growth, *J. Mater. Chem.*, 2000, **10**, 437–477.
75 E. N. S. Muccillo, R. A. Rocha, S. K. Tadokoro, J. F. Q. Rey, R. Muccillo and M. C. Steil, Electrical conductivity of CeO_2 prepared from nanosized powders, *J. Electroceram.*, 2004, **13**, 609–612.

76 F. Zhang, S. W. Chan, J. E. Spanier, E. Apak, Q. Jin, R. D. Robinson and I. P. Herman, Cerium oxide nanoparticles: size-selective formation and structure analysis, *Appl. Phys. Lett.*, 2002, **80**, 127–129.
77 F. Zhang, Q. Jin and S. W. Chan, Ceria nanoparticles: size, size distribution, and shape, *J. Appl. Phys.*, 2004, **95**, 4319–4326.
78 M. Kamruddin, P. K. Ajikumar, R. Nithya, A. K. Tyagi and B. Raj, Synthesis of nanocrystalline ceria by thermal decomposition and soft-chemistry methods, *Scr. Mater.*, 2004, **50**, 417–422.
79 R. D. Purohit, B. P. Sharma, K. T. Pillai and A. K. Tyagi, Ultrafine ceria powders *via* glycine–nitrate combustion, *Mater. Res. Bull.*, 2001, **36**, 2711–2721.
80 L. Madler, W. J. Stark and S. E. Pratsinis, Flame-made ceria nanoparticles, *J. Mater. Res.*, 2002, **17**, 1356–1362.
81 C. Laberty-Robert, J. W. Long, E. M. Lucas, K. A. Pettigrew, R. M. Stround, M. S. Doescher and D. R. Rolison, Sol–gel derived ceria nanoarchitectures: synthesis, characterization, and electrical properties, *Chem. Mater.*, 2006, **18**, 50–58.
82 M. Hirano and E. Kato, Hydrothermal synthesis of nanocrystalline cerium(IV) oxide powders, *J. Am. Ceram. Soc.*, 1999, **82**, 786–788.
83 C. W. Sun and L. Q. Chen, Controlled synthesis of shuttle-shaped ceria and its catalytic properties for CO oxidation, *Eur. J. Inorg. Chem.*, 2009, 3883–3887.
84 T. Masui, K. Fujiwara, K. Machida, G. Adachi, T. Sakata and H. Mori, Characterization of cerium(IV) oxide ultrafine particles prepared using reversed micelles, *Chem. Mater.*, 1997, **9**, 2197–2204.
85 Y. J. He, B. L. Yang and G. X. Cheng, Controlled synthesis of CeO_2 nanoparticles from the coupling route of homogenous precipitation with microemulsion, *Mater. Lett.*, 2003, **57**, 1880–18884.
86 N. Guillou, L. C. Nistor, H. Fuess and H. Hahn, Microstructural studies of nanocrystalline CeO_2 produced by gas condensation, *Nanostruct. Mater.*, 1997, **8**, 545–557.
87 L. Yin, Y. Wang, G. Pang, Y. Koltypin and A. Gedanken, Sonochemical synthesis of cerium oxide nanoparticles- effect of additives and quantum size effect, *J. Colloid Interface Sci.*, 2002, **246**, 78–84.
88 Y. Zhou, R. J. Phillips and J. A. Switzer, Electrochemical synthesis and sintering of nanocrystalline cerium(IV) oxide powders, *J. Am. Ceram. Soc.*, 1995, **78**, 981–985.
89 C. Burda, X. Chen, R. Narayanan and M. A. EI-Sayed, Chemistry and properties of nanocrystals of different shapes, *Chem. Rev.*, 2005, **105**, 1025–1102.
90 S. M. Lee, S. N. Cho and J. Cheon, Anisotropic shape control of colloidal inorganic nanocrystals, *Adv. Mater.*, 2003, **15**, 441–444.
91 Y. N. Xia, P. D. Yang, Y. G. Sun, Y. Y. Wu, B. Mayers, B. Gates, Y. D. Yin, F. Kim and Y. Q. Yan, One-dimensional nanostructures: synthesis, characterization, and applications, *Adv. Mater.*, 2003, **15**, 353–389.
92 G. S. Wu, T. Xie, X. Y. yuan, B. C. Cheng and L. D. Zhang, An improved sol–gel template synthetic route to large-scale CeO_2 nanowires, *Mater. Res. Bull.*, 2004, **39**, 1023–1028.
93 R. J. La, Z. A. Hu, H. L. Li, X. L. Shang and Y. Y. Yang, Template synthesis of CeO_2 ordered nanowire arrays, *Mater. Sci. Eng., A*, 2004, **368**, 145–148.
94 C. W. Sun, H. Li, Z. X. Wang, L. Q. Chen and X. J. Huang, Synthesis and characterization of polycrystalline CeO_2 nanowires, *Chem. Lett.*, 2004, 662–663.
95 C. W. Sun, H. Li, H. R. Zhang, Z. X. Wang and L. Q. Chen, Controlled synthesis of CeO_2 nanorods by a solvothermal method, *Nanotechnology*, 2005, **16**, 1454–1463.
96 A. Vantomme, Z. Y. Yuan, G. H. Du and B. L. Su, Surfactant-assisted large-scale preparation of crystalline CeO_2 nanorods, *Langmuir*, 2004, **21**, 1132–1135.
97 H. X. Mai, L. D. Sun, Y. W. Zhang, R. Si, W. Feng, H. P. Zhang, H. C. Liu and C. H. Yan, Shape-selective synthesis and oxygen storage behavior of ceria nanopolyhedra, nanorods, and nanocubes, *J. Phys. Chem. B*, 2005, **109**, 24380–24385.
98 K. B. Zhou, X. Wang, X. M. Sun, Q. Peng and Y. D. Li, Enhanced catalytic activity of ceria nanorods from well-defined reactive crystal planes, *J. Catal.*, 2005, **229**, 206–212.
99 W. Q. Han, L. J. Wu and Y. M. Zhu, Formation and oxidation state of CeO_{2-x} nanotubes, *J. Am. Chem. Soc.*, 2005, **127**, 12814–12815.
100 C. C. Tang, Y. Bando, B. D. Liu and D. Golberg, Cerium oxide nanotubes prepared from cerium hydroxide nanotubes, *Adv. Mater.*, 2005, **17**, 3005–3009.
101 K. Zhou, Z. Yang and S. Yang, Highly reducible CeO_2 nanotubes, *Chem. Mater.*, 2007, **19**, 1215–1217.
102 S. Yang and L. Gao, Controlled synthesis and self-assembly of CeO_2 nanocubes, *J. Am. Chem. Soc.*, 2006, **128**, 9330–9331.
103 R. Si, Y. Zhang, L. You and C. Yan, Rare-earth oxide nanopolyhedra, nanoplates, and nanodisks, *Angew. Chem., Int. Ed.*, 2005, **44**, 3256–3260.
104 T. Yu, J. Joo, Y. I. Park and T. Hyeon, Large-scale nonhydrolytic sol–gel synthesis of uniform-sized ceria nanocrystals with spherical, wire, and tadpole shapes, *Angew. Chem., Int. Ed.*, 2005, **44**, 7411–7414.
105 D. Wang, Y. Kang, V. Doan-Nguyen, J. Chen, R. Küngs, N. L. Wieder, K. Bakhmutsky, R. J. Gorte and C. B. Murray, Synthesis and oxygen storage capacity of two-dimensional ceria nanocrystals, *Angew. Chem., Int. Ed.*, 2011, **50**, 4378–4381.
106 T. Yu, B. Lim and Y. Xia, Aqueous-phase synthesis of single-crystal ceria nanosheets, *Angew. Chem., Int. Ed.*, 2010, **49**, 4484–4487.
107 G. Li, D. Qu, L. Arurault and Y. Tong, Hierarchically porous Gd^{3+}-doped CeO_2 nanostructures for the remarkable enhancement of optical and magnetic properties, *J. Phys. Chem. C*, 2009, **113**, 1235–1241.
108 J. A. Wang, J. M. Dominguez, A. Montoya, S. Castillo, J. Navarrete, M. Moran-Pineda, J. Reyes-Gasqa and X. Bokhimi, New insights into the defective structure and catalytic activity of Pd–ceria, *Chem. Mater.*, 2002, **14**, 4676–4683.
109 D. M. Lyons, J. P. McGrath and M. A. Morris, Surface studies of ceria and mesoporous ceria powders by solid-state H-1 MAS NMR, *J. Phys. Chem. B*, 2003, **107**, 4607–4617.
110 D. Terribile, A. Trovarelli, J. Llorca, C. de Leitenburg and G. Dolcetti, The synthesis and characterization of mesoporous high-surface area ceria prepared using a hybrid organic–inorganic route, *J. Catal.*, 1998, **178**, 299–308.
111 M. A. Carreon and V. V. Guliants, Ordered meso- and macroporous binary and mixed metal oxides, *Eur. J. Inorg. Chem.*, 2005, 27–43.
112 C. W. Sun, J. Sun, G. L. Xiao, H. R. Zhang, X. P. Qiu, H. Li and L. Q. Chen, Mesoscale organization of nearly monodisperse flowerlike ceria microspheres, *J. Phys. Chem. B*, 2006, **110**, 13445–13452.
113 C. W. Sun, G. L. Xiao, H. Li and L. Q. Chen, Mesoscale organization of flowerlike $La_2O_2CO_3$ and La_2O_3 microspheres, *J. Am. Ceram. Soc.*, 2007, **90**, 2576–2581.
114 G. L. Xiao, S. Li, H. Li and L. Q. Chen, Synthesis of doped ceria with mesoporous flowerlike morphology and its catalytic performance for CO oxidation, *Microporous Mesoporous Mater.*, 2009, **120**, 426–431.
115 C. W. Sun, H. Li and L. Q. Chen, Study of flowerlike CeO_2 microspheres used as catalyst supports for CO oxidation reaction, *J. Phys. Chem. Solids*, 2007, **68**, 1785–1790.
116 C. N. Xian, H. Li, L. Q. Chen and J. S. Lee, Morphological and catalytic stability of mesoporous peony-like ceria, *Microporous Mesoporous Mater.*, 2011, **142**, 202–207.
117 G. Xiao, C. N. Xian, H. Li and L. Q. Chen, Enhanced activity and stability of Cu–Mn and Cu–Ag catalysts supported on nanostructured mesoporous CeO_2 for CO oxidation, *J. Nanosci. Nanotechnol.*, 2011, **11**, 1923–1928.
118 J. Sun, Y. Wang, J. Li, G. Xiao, L. Zhang, H. Li, Y. Cheng, C. Sun, Z. Cheng, Z. Dong and L. Chen, H_2 production from stable ethanol steam reforming over catalyst of NiO based on flowerlike CeO_2 microspheres, *Int. J. Hydrogen Energy*, 2010, **35**, 3087–3091.
119 C. W. Sun, Z. Xie, C. R. Xia, H. Li and L. Q. Chen, Investigations of mesoporous CeO_2–Ru as a reforming catalyst layer for solid oxide fuel cells, *Electrochem. Commun.*, 2006, **8**, 833–838.
120 G. L. Xiao, Z. Jiang, H. Li, C. R. Xia and L. Q. Chen, Studies on composite cathode with nanostructured $Ce_{0.9}Sm_{0.1}O_{1.95}$ for intermediate temperature solid oxide fuel cells, *Fuel Cells*, 2009, **5**, 650–656.
121 J. Xing, H. F. Wang, C. Yang, S. Wang, H. J. Zhao, G. Z. Lu, P. Hu and H. G. Yang, Ceria foam with atomically thin single-crystal walls, *Angew. Chem., Int. Ed.*, 2012, **51**, 3611–3615.
122 A. H. Lu and F. Schuth, Nanocasting: a versatile strategy for creating nanostructured porous materials, *Adv. Mater.*, 2006, **18**, 1793–1805.
123 S. C. Laha and R. Ryoo, Synthesis of thermally stable mesoporous cerium oxide with nanocrystalline frameworks using mesoporous silica templates, *Chem. Commun.*, 2003, 2138–2139.

124 P. Ji, J. Zhang, F. Chen and M. Anpo, Ordered mesoporous CeO_2 synthesized by nanocasting from cubic Ia3d mesoporous MCM-48 silica: formation, characterization and photocatalytic activity, *J. Phys. Chem. C*, 2008, **112**, 17809–17813.

125 J. Chane-Ching, F. Cobo, D. Aubert, H. G. Harvey, M. Airiau and A. Corma, A general method for the synthesis of nanostructured large-surface-area materials through the self-assembly of functionalized nanoparticles, *Chem.–Eur. J.*, 2005, **11**, 979–987.

126 Q. Yuan, Q. Liu, W. G. Song, W. Feng, W. L. Pu, L. D. Sun, Y. W. Zhang and C. H. Yan, Ordered mesoporous $Ce_{1-x}Zr_xO_2$ solid solutions with crystalline walls, *J. Am. Chem. Soc.*, 2007, **129**, 6698–6699.

127 X. Liang, X. Wang, Y. Zhuang, B. Xu, S. M. Kuang and Y. D. Li, Formation of CeO_2–ZrO_2 solid solution nanocages with controllable structures *via* Kirkendall effect, *J. Am. Chem. Soc.*, 2008, **130**, 2736–2737.

128 T. Mitsudome, Y. Mikami, M. Matoba, T. Mizugaki, K. Jitsukawa and K. Kaneda, Design of a silver–cerium dioxide core–shell nanocomposite catalyst for chemoselective reduction reactions, *Angew. Chem., Int. Ed.*, 2012, **51**, 136–139.

129 Y. Wei, J. Liu, Z. Zhao, A. J. Duan, G. Y. Jiang, C. M. Xu, J. S. Gao, H. He and X. P. Wang, Three-dimensionally ordered macroporous $Ce_{0.8}Zr_{0.2}O_2$-supported gold nanoparticles: synthesis with controllable size and super-catalytic performance for soot oxidation, *Energy Environ. Sci.*, 2011, **4**, 2959–2970.

130 D. C. Sayle, X. D. Feng, Y. Ding, Z. L. Wang and T. X. T. Sayle, "Simulating Synthesis": ceria nanosphere self-assembly into nanorods and framework architectures, *J. Am. Chem. Soc.*, 2007, **129**, 7924–7935.

131 N. V. Skorodumova, S. I. Simak, B. I. Lundqvist, I. A. brikosov and B. Johansson, Quantum origin of the oxygen storage capability of ceria, *Phys. Rev. Lett.*, 2002, **89**, 166601.

132 C. R. A. Catlow, Atomistic mechanisms of ionic transport in fast-ion conductors, *J. Chem. Soc., Faraday Trans.*, 1990, **86**, 1167–1176.

133 F. Esch, S. Fabris, L. Zhou, T. Montini, C. Africh, P. Fornasiero, G. Comelli and R. Rosei, Electron localization determines defect formation on ceria substrates, *Science*, 2005, **309**, 752–755.

134 X. W. Liu, K. B. Zhou, L. Wang, B. Y. Wang and Y. D. Li, Oxygen vacancy clusters promoting reducibility and activity of ceria nanorods, *J. Am. Chem. Soc.*, 2009, **131**, 3140–3141.

135 M. V. Ganduglia-Pirovano, J. L. F. Da Silva and J. Sauer, Density-functional calculations of the structure of near-surface oxygen vacancies and electron localization on CeO_2 (111), *Phys. Rev. Lett.*, 2009, **102**, 026101.

136 M. V. Ganduglia-Pirovano, A. Hofmann and J. Sauer, Oxygen vacancies in transition metal and rare earth oxides: current state of understanding and remaining challenges, *Surf. Sci. Rep.*, 2007, **62**, 219–270.

137 S. Fabris, G. Vicario, G. Balducci, S. De Gironcoli and S. Baroni, Electronic and atomistic structures of clean and reduced ceria surfaces, *J. Phys. Chem. B*, 2005, **109**, 22860–22867.

138 N. V. Skorodumova, R. Ahuja, S. I. Simak, I. A. Abrikosov, B. Johansson and B. I. Lundqvist, Electronic, bonding, and optical properties of CeO_2 and Ce_2O_3 from first principles, *Phys. Rev. B: Condens. Matter*, 2001, **64**, 115108.

139 D. A. Andersson, S. I. Simak, B. Johansson, I. A. Abrikosov and N. V. Skorodumova, Modeling of CeO_2, Ce_2O_3, and CeO_{2-x} in the LDA plus U formalism, *Phys. Rev. B: Condens. Matter Mater. Phys.*, 2007, **75**, 035109.

140 Y. Tang, H. Zhang, L. Cui, C. Ouyang, S. Shi, W. Tang, H. Li, J. Lee and L. Chen, First-principles investigation on redox properties of M-doped CeO_2 (M = Mn, Pr, Sn, Zr), *Phys. Rev. B: Condens. Matter Mater. Phys.*, 2010, **82**, 125104.

141 D. A. Andersson, S. I. Simak, N. V. Skorodumova, I. A. Abrikosov and B. Johansson, Optimization of ionic conductivity in doped ceria, *Proc. Natl. Acad. Sci. U. S. A.*, 2006, **103**, 3518–3521.

142 T. X. T. Sayle, S. C. Parker and C. R. A. Catlow, The role of oxygen vacancies on ceria surfaces in the oxidation of carbon monoxide, *Surf. Sci.*, 1994, **316**, 329–336.

143 C. Conesa, Computer modeling of surfaces and defects on cerium dioxide, *Surf. Sci.*, 1995, **339**, 337–352.

144 Z. Yang, T. K. Woo, M. Baudin and K. Hermansson, Atomic and electronic structure of unreduced and reduced CeO_2 surfaces: a first-principles study, *J. Chem. Phys.*, 2004, **120**, 7741–7749.

145 M. Nolan, S. C. Parker and G. W. Watson, CeO_2 catalysed conversion of CO, NO_2 and NO from first principles energetic, *Phys. Chem. Chem. Phys.*, 2006, **8**, 216–218.

146 Z. P. Liu, S. J. Jenkins and D. A. King, Origin and activity of oxidized gold in water-gas-shift catalysis, *Phys. Rev. Lett.*, 2005, **94**, 196102.

147 C. Loschen, S. T. Bromley, K. M. Neyman and F. Illas, Understanding ceria nanoparticles from first-principles calculations, *J. Phys. Chem. C*, 2007, **111**, 10142–10145.

148 C. Loschen, A. Migani, S. T. Bromley, F. Illas and K. M. Neyman, Density functional studies of model cerium oxide nanoparticles, *Phys. Chem. Chem. Phys.*, 2008, **10**, 5730–5738.

149 A. Migani, C. Loschen, F. Illas and K. M. Neyman, Towards size-converged properties of model ceria nanoparticles: monitoring by adsorbed CO using DFT plus *U* approach, *Chem. Phys. Lett.*, 2008, **465**, 106–109.

150 G. C. Bond and D. T. Thompson, Catalysis by gold, *Catal. Rev. Sci. Eng.*, 1999, **41**, 319–388.

151 V. Boissel, S. Tahir and C. A. Koh, Catalytic decomposition of N_2O over monolithic supported nobel metal-transition metal oxides, *Appl. Catal., B*, 2006, **64**, 234–242.

152 S. Bernal, J. Kaspar and A. Trovarelli, Recent progress in catalysis by ceria and related compounds-Preface, *Catal. Today*, 1999, **50**, 173–173.

153 G. N. Vayssilov, Y. Lykhach, A. Migani, T. Staudt, G. P. Petrova, N. Tsud, T. Skála, A. Bruix, F. Illas, K. C. Prince, V. Matolín, K. M. Neyman and J. Libuda, Support nanostructure boosts oxygen transfer to catalytically active platinum nanoparticles, *Nat. Mater.*, 2011, **10**, 310–315.

154 C. Harding, V. Habibpour, S. Kunz, A. N. Farnbacher, U. Heiz, B. Yoon and U. Landman, Control and manipulation of gold nanocatalysis: effects of metal oxide support thickness and composition, *J. Am. Chem. Soc.*, 2009, **131**, 538–548.

155 C. T. Campbell, S. C. Parker and D. E. Starr, The effect of size-dependent nanoparticle energetics on catalyst sintering, *Science*, 2002, **298**, 811–814.

156 G. Renaud, R. Lazzari, C. Revenant, A. Barbier, M. Noblet, O. Ulrich, F. Leroy, J. Jupille, Y. Borensztein, C. R. Henry, J. Deville, F. Scheurer, J. Mane-Mane and O. Fruchart, Real-time monitoring of growing nanoparticles, *Science*, 2003, **300**, 1416–1419.

157 W. C. Conner and J. L. Falconer, Spillover in heterogeneous catalysis, *Chem. Rev.*, 1995, **95**, 759–788.

158 J. Libuda and H. J. Freund, Molecular beam experiments on model catalysts, *Surf. Sci. Rep.*, 2005, **57**, 157–298.

159 A. Caballero, J. P. Holgado, V. M. Gonzalez-delaCruz, S. E. Habas, T. Herranz and M. Salmeron, *In situ* spectroscopic detection of SMSI effect in a Ni–CeO_2 system: hydrogen-induced burial and dig out of metallic nickel, *Chem. Commun.*, 2010, **46**, 1097–1099.

160 U. Diebold, The surface science of titanium dioxide, *Surf. Sci. Rep.*, 2003, **48**, 53–229.

161 T. Schalow, M. Laurin, B. Brandt, S. Schauermann, S. Guimond, H. Kuhlenbeck, D. E. Starr, S. K. Shaikhutdinov, J. Libuda and H. Freund, Oxygen storage at the metal–oxide interface of catalyst nanoparticles, *Angew. Chem., Int. Ed.*, 2005, **44**, 7601–7605.

162 C. J. Zhang, A. Michaelides and S. J. Jenkins, Theory of gold on ceria, *Phys. Chem. Chem. Phys.*, 2011, **13**, 22–33.

163 F. Esch, S. Fabris, L. Zhou, T. Montini, C. Africh, P. Fornasiero, G. Comelli and R. Rosei, Electron localization determines defect formation on ceria substrates, *Science*, 2005, **309**, 752–755.

164 N. J. Lawrence, J. R. Brewer, L. Wang, T. S. Wu, J. Wells-Kingsbury, M. M. Ihrig, G. H. Wang, Y. L. Soo, W. N. Mei and C. L. Cheung, Defect engineering in cubic cerium oxide nanostructures for catalytic oxidation, *Nano Lett.*, 2011, **11**, 2666–2671.

165 M. Baron, O. Bondarchuk, D. Stacchiola, S. Shaikhutdinov and H. J. Freund, Interaction of gold with cerium oxide supports: CeO_2 (111) thin films *vs.* CeO_x nanoparticles, *J. Phys. Chem. C*, 2009, **113**, 6042–6046.

166 Y. Chen, P. Hu, M. Lee and H. Wang, Au on (111) and (110) surfaces of CeO_2: a density-functional theory study, *Surf. Sci.*, 2008, **602**, 1736–1741.

167 G. I. N. Waterhouse, G. A. Bowmaker and J. B. Metson, Influence of catalyst morphology on the performance of electrolytic silver catalysts for the partial oxidation of methanol to formaldehyde, *Appl. Catal., A*, 2004, **266**, 257–273.

168 F. Raimondi, G. G. Scherer, R. Kotz and A. Wokaun, Nanoparticles in energy technology: examples from electrochemistry and catalysis, *Angew. Chem., Int. Ed.*, 2005, **44**, 2190–2209.
169 C. J. Zhang, A. Michaelides, D. A. King and S. J. Jenkins, Positive charge states and possible polymorphism of gold nanoclusters on reduced ceria, *J. Am. Chem. Soc.*, 2010, **132**, 2175–2182.
170 H. Y. Kim, H. M. Lee and G. Henkelman, CO oxidation mechanism on CeO_2 supported Au nanoparticles, *J. Am. Chem. Soc.*, 2012, **134**, 1560–1570.
171 A. U. Nilekaer, S. Alayoglu, B. Eichhorn and M. Mavrikakis, Preferential CO oxidation in hydrogen: reactivity of core–shell nanoparticles, *J. Am. Chem. Soc.*, 2010, **132**, 7418–7428.
172 H. P. Zhou, H. S. Wu, J. Shen, A. X. Yin, L. D. Sun and C. H. Yan, Thermally stable Pt–CeO_2 hetero-nanocomposites with high catalytic activity, *J. Am. Chem. Soc.*, 2010, **132**, 4998–4999.
173 C. M. Y. Yeung and S. C. Tsang, Some optimization in preparing core–shell Pt–ceria catalysts for water gas shift reaction, *J. Mol. Catal. A: Chem.*, 2010, **322**, 17–25.
174 D. Pierre, W. L. Deng and M. Flytzani-Stephanopoulos, The importance of strongly bound Pt–CeO_x species for the water-gas shift reaction: catalyst activity and stability evaluation, *Top. Catal.*, 2007, **46**, 363–373.
175 Z. Y. Sun, H. Y. Zhang, G. M. An, G. Y. Yang and Z. M. Liu, Supercritical CO_2-facilitating large-scale synthesis of CeO_2 nanowires and their application for solvent-free selective hydrogenation of nitroarenes, *J. Mater. Chem.*, 2010, **20**, 1947–1952.
176 G. N. Vayssilov, A. Migani and K. Neyman, Density functional modeling of the interactions of platinum clusters with CeO_2 nanoparticles of different size, *J. Phys. Chem. C*, 2011, **115**, 16081–16086.
177 J. Wang, M. L. Liu and M. C. Lin, Oxygen reduction reactions in the SOFC cathode of Ag–CeO_2, *Solid State Ionics*, 2006, **177**, 939–947.
178 F. Zhang, P. Wang, J. Koberstein, S. Khalid and S. W. Chan, Cerium oxidation state in ceria nanoparticles studied with X-ray photoelectron spectroscopy and absorption near edge spectroscopy, *Surf. Sci.*, 2004, **563**, 74–82.
179 C. Zhang, M. E. Grass, A. H. McDaniel, S. C. DeCaluwe, F. El Gabaly, Z. Liu, K. F. McCarty, R. L. Farrow, M. A. Linne, Z. Hussain, G. S. Jackson, H. Bluhm and B. W. Eichhorn, Measuring fundamental properties in operating solid oxide electrochemical cells by using *in situ* X-ray photoelectron spectroscopy, *Nat. Mater.*, 2010, **9**, 944–949.
180 R. T. Vang, J. V. Lauritsen, E. Lægsgaard and F. Besenbacher, Scanning tunneling microscopy as a tool to study catalytically relevant model systems, *Chem. Soc. Rev.*, 2008, **37**, 2193–2203.
181 K. Fukui, Y. Namai and Y. Iwasawa, Imaging of surface oxygen atoms and their defect structures on CeO_2 (111) by noncontact atomic force microscopy, *Appl. Surf. Sci.*, 2002, **188**, 252–256.
182 Y. Namai, K. I. Fukui and Y. Iwasawa, Atom-resolved noncontact atomic force microscopic and scanning tunneling microscopic observations of the structure and dynamic behavior of CeO_2 (111) surfaces, *Catal. Today*, 2003, **85**, 79–91.
183 S. Torbrügge, M. Reichling, A. Ishiyama, S. Morita and O. Custance, Evidence of subsurface oxygen vacancy ordering on reduced CeO_2 (111), *Phys. Rev. Lett.*, 2007, **99**, 056101.
184 J. Jerratsch, X. Shao, N. Nilius, H. Freund, C. Popa, M. Veronica Ganduglia-Pirovano, A. M. Burow and J. Sauer, Electron localization in defective ceria films: a study with scanning-tunneling microscopy and density-functional theory, *Phys. Rev. Lett.*, 2011, **106**, 246801.
185 M. Varela, J. Gazquez and S. J. Pennycook, STEM–EELS imaging of complex oxides and interfaces, *MRS Bull.*, 2012, **37**, 29–35.
186 J. Y. Liu, Advanced electron microscopy of metal-supported interactions in supported metal catalysts, *ChemCatChem*, 2011, **3**, 934–948.
187 S. J. Haigh, N. P. Young, H. Sawada, K. Takayanagi and A. I. Kirkland, Imaging the active surfaces of cerium dioxide nanoparticles, *ChemPhysChem*, 2011, **12**, 2397–2399.
188 U. M. Bhatta, I. M. Ross, T. X. T. Sayle, D. C. Sayle, S. C. Parker, D. Reid, S. Seal, A. Kumar and G. Möbus, Cationic surface reconstructions on cerium oxide nanocrystals: an aberration-corrected HRTEM study, *ACS Nano*, 2012, **6**, 421–430.
189 H. Hojo, T. Mizoguchi, H. Ohta, S. D. Findlay, N. Shibata, T. Yamamoto and Y. Ikuhara, Atomic structure of a CeO_2 grain boundary: the role of oxygen vacancies, *Nano Lett.*, 2010, **10**, 4668–4672.
190 L. Minervini, M. O. Zacate and R. W. Grimes, Defect cluster formation in M_2O_3-doped CeO_2, *Solid State Ionics*, 1999, **116**, 339–349.
191 A. S. Barnard and A. I. Kirkland, Combining theory and experiment in determining the surface chemistry of nanocrystals, *Chem. Mater.*, 2008, **20**, 5460–5463.
192 M. Manzoli, G. Avgouropoulos, T. Tabakova, J. Papavasiliou, T. Ioannides and F. Boccuzzi, Preferential CO oxidation in H_2-rich gas mixtures over Au/doped ceria catalysts, *Catal. Today*, 2008, **138**, 239–243.
193 T. Kayama, K. Yamazaki and H. Shinjoh, Nanostructured ceria–silver synthesized in one-pot redox reaction catalyzes carbon oxidation, *J. Am. Chem. Soc.*, 2010, **132**, 13154–13155.
194 C. M. Y. Yeung, K. M. K. Yu, A. J. Fu, D. Thompsett, M. I. Petch and S. C. Tsang, Engineering Pt in ceria for a maximum metal-support interaction in catalysis, *J. Am. Chem. Soc.*, 2005, **127**, 18010–18011.
195 M. Haruta, Nanoparticulate gold catalysts for low-temperature CO oxidation, *J. New Mater. Electrochem. Syst.*, 2004, **7**, 163–172.
196 Z. X. Song, W. Liu, H. Nishiguchi, A. Takami, K. Nagaoka and Y. Takita, The Pr promotion effect on oxygen storage capacity of Ce–Pr oxides studied using a TAP reactor, *Appl. Catal., A*, 2007, **329**, 86–92.
197 T. Y. Zhang, S. P. Wang, Y. Yu, Y. Su, X. Z. Guo, S. R. Wang, S. M. Zhang and S. H. Wu, Synthesis, characterization of CuO/$Ce_{0.8}Sn_{0.2}O_2$ catalysts for low-temperature CO oxidation, *Catal. Commun.*, 2008, **9**, 1259–1264.
198 R. Sasikala, N. M. Gupta and S. K. Kulshreshtha, Temperature-programmed reduction and CO oxidation studies over Ce–Sn mixed oxides, *Catal. Lett.*, 2001, **71**, 69–73.
199 A. T. Bell, The impact of nanoscience on heterogeneous catalysis, *Science*, 2003, **299**, 1688–1691.
200 G. A. Somorjai and Y. G. Borodko, Research in nanosciences-great opportunity for catalysis science, *Catal. Lett.*, 2001, **76**, 1–5.
201 R. Schlögl and S. B. A. Hamid, Nanocatalysis: mature science revisited or something really new?, *Angew. Chem., Int. Ed.*, 2004, **43**, 1628–1637.
202 B. M. Choudary, R. S. Mulukutla and K. J. Klabunde, Benzylation of aromatic compounds with different crystallite of MgO, *J. Am. Chem. Soc.*, 2003, **125**, 2020–2021.
203 X. W. Liu, K. B. Zhou, L. Wang, B. Y. Wang and Y. D. Li, Oxygen vacancy clusters promoting reducibility and activity of ceria nanorods, *J. Am. Chem. Soc.*, 2009, **131**, 3140–3141.
204 T. X. T. Sayle, S. C. Parker and C. R. A. Catlow, The role of oxygen vacancies on ceria surfaces in the oxidation of carbon monoxide, *Surf. Sci.*, 1994, **316**, 329–336.
205 R. Si and M. Flytzani-Stephanopoulos, Shape and crystal-plane effects of nanoscale ceria on the activity of Au–CeO_2 catalysts for the water-gas shift reaction, *Angew. Chem., Int. Ed.*, 2008, **47**, 2884–2887.
206 M. B. Boucher, S. Goergen, N. Yi and M. Flytzani-Stephanopoulos, 'Shape effects' in metal oxide supported nanoscale gold catalysts, *Phys. Chem. Chem. Phys.*, 2011, **13**, 2517–2527.
207 D. K. Liguras, D. I. Kondarides and X. E. Verykios, Production of hydrogen for fuel cells by steam reforming of ethanol over supported nobel metal catalysts, *Appl. Catal., B*, 2003, **43**, 345–354.
208 G. A. Deluga, J. R. Salge, L. D. Schmidt and X. E. Verykios, Renewable hydrogen from ethanol by autothermal reforming, *Science*, 2004, **303**, 993–997.
209 J. Sun, X. P. Qiu, F. Wu and W. T. Zhu, H_2 from steam reforming of ethanol at low temperature over Ni/Y_2O_3, Ni/La_2O_3 and Ni/Al_2O_3 catalysts for fuel-cell application, *Int. J. Hydrogen Energy*, 2005, **30**, 437–445.
210 J. Kugai, V. Subramani, C. S. Song, M. H. Engelhard and Y. H. Chin, Effects of nanocrystalline CeO_2 supports on the properties and performance of Ni–Rh bimetallic catalyst for oxidative steam reforming of ethanol, *J. Catal.*, 2006, **238**, 430–440.
211 C. Diagne, H. Idriss and A. Kiennemann, Hydrogen production by ethanol reforming over Rh/CeO_2–ZrO_2 catalysts, *Catal. Commun.*, 2002, **3**, 565–571.
212 W. I. Hsiao, Y. S. Lin, Y. C. Chen and C. S. Lee, The effect of the morphology of nanocrystalline CeO_2 on ethanol reforming, *Chem. Phys. Lett.*, 2007, **441**, 294–299.

213 N. Yi, R. Si, H. Saltsburg and M. Flytzani-Stephanopoulos, Active gold species on cerium oxide nanoshapes for methanol steam reforming and water gas shift reactions, *Energy Environ. Sci.*, 2010, **3**, 831–837.
214 O. A. Marina and M. Mogensen, High-temperature conversion of methane on a composite gadolinia-doped ceria–gold electrode, *Appl. Catal., A*, 1999, **189**, 117–126.
215 R. J. Gorte and J. M. Vohs, Nanostructured anodes for solid oxide fuel cells, *Curr. Opin. Colloid Interface Sci.*, 2009, **14**, 236–244.
216 H. P. He, R. J. Gorte and J. M. Vohs, Highly sulfur tolerant Cu–ceria anodes for SOFCs, *Electrochem. Solid-State Lett.*, 2005, **8**, A279–A280.
217 H. Kurokawa, T. Z. Sholklapper, C. P. Jacobson, S. J. Visco and L. C. De Jonghe, Ceria nanocoating for sulfur tolerant Ni-based anodes of solid oxide fuel cells, *Electrochem. Solid-State Lett.*, 2007, **10**, B135–B138.
218 W. C. Chueh, Y. Hao, W. Jung and S. M. Haile, High electrochemical activity of the oxide phase in model ceria–Pt and ceria–Ni composite anodes, *Nat. Mater.*, 2012, **11**, 156–161.
219 Z. Zhan and S. A. Barnett, An octane-fueled solid oxide fuel cell, *Science*, 2005, **308**, 844–847.
220 M. I. Litter, Heterogeneous photocatalysis transition metal ions in photocatalytic systems, *Appl. Catal., B*, 1999, **23**, 89–114.
221 A. Corma, P. Atienzar, H. García and J. Chane-Ching, Hierarchically mesostructured doped CeO_2 with potential for solar-cell use, *Nat. Mater.*, 2004, **3**, 394–397.
222 D. Gust, T. A. Moore and A. L. Moore, Solar fuels *via* artificial photosynthesis, *Acc. Chem. Res.*, 2009, **42**, 1890–1898.
223 A. Kudo and Y. Miseki, Heterogeneous photocatalyst materials for water splitting, *Chem. Soc. Rev.*, 2009, **38**, 253–278.
224 P. V. Kamat, Meeting the clean energy demand: nanostructure architectures for solar energy conversion, *J. Phys. Chem. C*, 2007, **111**, 2834–2860.
225 R. M. N. Yerga, M. C. A. Galvan, F. del Valle, J. A. V. de la Mano and J. L. G. Fierro, Water splitting on semiconductor catalysts under visible-light irradiation, *ChemSusChem*, 2009, **2**, 471–485.
226 J. F. Zhu and M. Zach, Nanostructured materials for photocatalytic hydrogen production, *Curr. Opin. Colloid Interface Sci.*, 2009, **14**, 260–269.
227 M. D. Hernandez-Alonso, F. Fresno, S. Suarez and J. M. Coronado, Development of alternative photocatalysts to TiO_2: challenges and opportunities, *Energy Environ. Sci.*, 2009, **2**, 1231–1257.
228 A. Primo, T. Marino, A. Corma, R. Molinari and H. García, Efficient visible-light photocatalytic water splitting by minute amounts of gold supported on nanoparticulate CeO_2 obtained by a biopolymer templating method, *J. Am. Chem. Soc.*, 2011, **133**, 6930–6933.
229 X. Lu, T. Zhai, H. Cui, J. Shi, S. Xie, Y. Huang, C. Liang and Y. Tong, Redox cycles promoting photocatalytic hydrogen evolution of CeO_2 nanorods, *J. Mater. Chem.*, 2011, **21**, 5569–5572.
230 Z. Tang, Y. Zhang and Y. Xu, A facile and high-yield approach to synthesize one-dimensional CeO_2 nanotubes with well-shaped hollow interior as a photocatalyst for degradation of toxic pollutants, *RSC Adv.*, 2011, **1**, 1772–1777.
231 G. Centi and S. Perathoner, Towards solar fuels from water and CO_2, *ChemSusChem*, 2010, **3**, 195–208.
232 W. C. Chueh, C. Falter, M. Abbott, D. Scipio, P. Furler, S. M. Haile and A. Steinfeld, High-flux solar-driven thermochemical dissociation of CO_2 and H_2O using nonstoichiometric ceria, *Science*, 2010, **330**, 1797–1801.
233 W. C. Chueh and S. M. Haile, Ceria as a Thermochemical reaction medium for selectively generating syngas or methane from H_2O and CO_2, *ChemSusChem*, 2009, **2**, 735–739.
234 P. Furle, J. R. Scheffe and A. Steinfeld, Syngas production by simultaneous splitting of H_2O and CO_2 *via* ceria redox reactions in a high-temperature solar reactor, *Energy Environ. Sci.*, 2012, **5**, 6098–6103.
235 T. Suzuki, I. Kosacki, H. U. Anderson and P. Colomban, Electrical conductivity and lattice defects in nanocrystalline cerium oxide thin films, *J. Am. Ceram. Soc.*, 2001, **84**, 2007–2014.
236 D. Barreca, A. Gasparotto, C. Maccato, C. Maragno, E. Tondello, E. Comini and G. Sberveglieri, Columnar CeO_2 nanostructures for sensor application, *Nanotechnology*, 2007, **18**, 125502.
237 T. Brousse and D. M. Schleich, Sprayed and thermally evaporated SnO_2 thin film for ethanol sensors, *Sens. Actuators, B*, 1996, **31**, 77–79.
238 M. J. Madou and S. R. Morrison, *Chemical Sensing with Solid State Devices*, Academic Press Inc., New York, 1988, pp. 67–104.
239 K. S. Brinkman, H. Takamura, H. L. Tuller and T. Iijima, The oxygen permeation properties of nanocrystalline CeO_2 thin films, *J. Electrochem. Soc.*, 2010, **157**, B1852–B1857.
240 A. Tschope and R. Birringer, Grain size dependence of electrical conductivity in polycrystalline cerium oxide, *J. Electroceram.*, 2001, **7**, 169–177.
241 M. Das, S. Patil, N. Bhargava, J. F. Kang, L. M. Riedel, S. Seal and J. J. Hickman, Auto-catalytic ceria nanoparticles offer neuroprotection to adult rat spinal cord neurons, *Biomaterials*, 2007, **28**, 1918–1925.
242 J. M. Perez, A. Asati, S. Nath and C. Kaittanis, Synthesis of biocompatible dextran-coated nanoceria with pH-dependent antioxidant properties, *Small*, 2008, **4**, 552–556.
243 D. Schubert, R. Dargusch, J. Raitano and S. W. Chan, Cerium and yttrium oxide nanoparticles are neuroprotective, *Biochem. Biophys. Res. Commun.*, 2006, **342**, 86–91.
244 S. S. Lee, H. G. Zhu, E. Q. Contreras, A. Prakash, H. L. Puppala and V. L. Colvin, High temperature decomposition of cerium precursors to form ceria nanocrystal libraries for biological applications, *Chem. Mater.*, 2012, **24**, 424–432.
245 Y. Y. Tsai, J. Oca-Cossio, K. Agering, N. E. Simpson, M. A. Atkinson, C. H. Wasserfall, I. Constantinidis and W. Sigmund, Novel synthesis of cerium oxide nanoparticles for free radical scavenging, *Nanomedicine*, 2007, **2**, 325–332.
246 A. Nel, T. Xia, L. Mädler and N. Li, Toxic potential of materials at the nanolevel, *Science*, 2006, **311**, 622–627.
247 T. Xia, M. Kovochich, M. Liong, L. Mädler, B. Gilbert, H. Shi, J. I. Yeh, J. I. Zink and A. E. Nel, Comparison of the mechanism of toxicity of zinc oxide and cerium oxide nanoparticles based on dissolution and oxidative stress properties, *ACS Nano*, 2008, **2**, 2121–2134.
248 Health Effects Institute, *Evaluation of Human Health Risk from Cerium Added to Diesel Fuel, Communication 9*, Health Effects Institute, Boston, MA, 2001.
249 Development of Reference Doses and Reference Concentrations for Lanthanides, Toxicology Excellence for Risk Assessment, The Bureau of Land Management, National Applies Resource Sciences Center, Amended Stage 2, November 1999.
250 A. Chroneos, B. Yildiz, A. Tarancón, D. Parfitt and J. A. Kilner, Oxygen diffusion in solid oxide fuel cell cathode and electrolyte materials: mechanistic insights from atomistic simulations, *Energy Environ. Sci.*, 2011, **4**, 2774–2789.
251 S. Cavaliere, S. Subianto, I. Savych, D. J. Jones and J. Rozière, Electrospinning: designed architectures for energy conversion and storage devices, *Energy Environ. Sci.*, 2011, **4**, 4761–4785.